

Part II

DEVELOPMENT OF A NEW WALL HEAT FLUX PARTITIONING MODEL

5

INTRODUCTION TO HEAT FLUX PARTITIONING

Contents

5.1	Introduction	51
5.1.1	Empirical Approaches	51
5.1.2	First Heat Flux Partitioning Approaches	52
5.2	Kurul & Podowski (1990)	53
5.3	Basu, Warrier & Dhir (2005)	54
5.3.1	Case 1 : Bubble Sliding, $D_d < s$	55
5.3.2	Case 2 : Bubble Coalescence without Sliding, $D_d \geq s$	56
5.4	Gilman (2017)	57
5.5	Kommajosyula (2020)	59
5.6	Conclusion	60

5.1 INTRODUCTION

5.1.1 Empirical Approaches

In the field of heat transfer and boiling, establishing a physical relationship between the applied heat flux at the wall ϕ_w and the wall temperature T_w has always been a primal goal for system design and safety analysis. Traditional approaches for single-phase flows rely on the estimation of the heat transfer coefficient h_{SP} defined as:

$$\phi_w = h_{SP} (T_L - T_w) \quad (5.1)$$

where T_w and T_L are the wall and bulk liquid temperature.

Estimating h_{SP} is usually done using dedicated correlations depending on flow parameters such as the hydraulic Reynolds number Re_{D_h} , the fluid Prandtl number Pr_L , etc. Correlations of Dittus-Boelter (Eq 3.20) or Gnielinski (Eq. 3.21) that were presented earlier are typical example of widely used expressions to estimate h_{SP} .

For boiling multiphase flows, different types of empirical approaches have been developed through the history. For instance, some authors proposed direct correlations relating wall heat flux and temperature such as:

- Jens & Lottes [61]:

$$\phi_w = \left(\frac{\Delta T_w}{25} e^{P/62} \right)^4 \quad (5.2)$$

- Thom *et al.* [124]:

$$\phi_w = \left(\frac{\Delta T_w}{22.65} e^{P/87} \right)^2 \quad (5.3)$$

with P in bar and ϕ_w in MW/m².

On the other hand, some models are based on the estimation of heat transfer coefficients similar to single-phase approaches. They mostly rely on the separation between a single phase h_{SP} and nucleate boiling h_{NB} heat transfer coefficients. Well-known correlations of this type are proposed by Chen [16], Gungor & Winterton [54] or Liu & Winterton [83]. For instance, Chen correlation writes:

$$\phi_w = \phi_{SP} + \phi_{NB} = h_{SP} (T_w - T_L) F + h_{NB} (T_w - T_{sat}) S \quad (5.4)$$

with F an amplification factor for the single phases heat transfer due to bubble agitation and S a suppression term hindering the nucleate boiling under the effect of bulk liquid flow.

The single phase part h_{SP} is calculated using Dittus-Boelter [29] formulation (Eq. 3.20) while the nucleate boiling part is:

$$h_{NB} = 0.00122 \frac{\lambda_L^{0.79} c_{p,L}^{0.45} \rho_L^{0.49}}{\sigma^{0.5} \mu_L^{0.29} h_{LV}^{0.24} \rho_V^{0.24}} \Delta T_w^{0.25} (P_{sat}(T_w) - P_{sat}(T_{sat}))^{0.75} \quad (5.5)$$

along with the factors F and S :

$$\frac{1}{X_{tt}} = \left(\frac{x}{1-x} \right)^{0.9} \left(\frac{\rho_L}{\rho_V} \right)^{0.5} \left(\frac{\mu_V}{\mu_L} \right)^{0.1} \quad (5.6)$$

$$F = \begin{cases} 1 & \text{if } X_{tt} \geq 1 \\ 2.35 \left(\frac{1}{X_{tt}} + 0.213 \right)^{0.736} & \text{if } X_{tt} \leq 1 \end{cases} \quad (5.7)$$

$$S = \frac{1}{1 + 2.53 \times 10^6 \text{Re}_{D_h}^{1.17}} \quad (5.8)$$

where X_{tt} is the Lockhart-Martinelli parameter [84] and x the vapor quality.

Each of those correlations has been developed for given experimental conditions such as high pressure flows up to 150 bar for Thom and Jens & Lottes correlations while Chen correlation is dedicated for low to moderate pressure (~ 35 bar).

5.1.2 First Heat Flux Partitioning Approaches

The spirit of splitting the different heat transfer mechanisms (single-phase, nucleate boiling) using different heat transfer coefficients is actually a premise to what is nowadays called the "Heat Flux Partitioning" approach. Bowring [10] is among the first author who actually expressed the total heat flux at the wall as separate contributions between different heat transfer mechanisms by writing:

$$\phi_w = \phi_e + \phi_a + \phi_{SP} \quad (5.9)$$

where ϕ_e is the latent-heat transfer associated to evaporation, ϕ_a the convection due to bubble agitation and ϕ_{SP} the single-phase heat transfer to the liquid.

Making steps towards a more mechanistic description of boiling, he wrote:

$$\phi_e = N_{sit} f V_b \rho_V h_{LV} \quad (5.10)$$

where N_{sit} is the nucleation site density on the surface, f the bubble nucleation frequency, V_b the bubble volume. Those parameters need dedicated description and modeling based on experimental measurements. Nonetheless, an empirical parameter is introduced by Bowring to estimate the bubble-agitation term ϕ_a as:

$$\phi_w = \phi_{SP} + (1 + \varepsilon) \phi_e \quad (5.11)$$

$$\varepsilon = \frac{\phi_a}{\phi_e} \approx \frac{\rho_L c_{p,L}}{\rho_V h_{LV}} (T_w - T_L) \quad (5.12)$$

where ε has to be experimentally estimated. We can notably observe that its expression is that of a Jakob number based on the temperature difference between the wall and the liquid temperature.

This idea of splitting the wall heat flux and try to precisely model each heat transfer mechanisms using detailed parameters (nucleation site density, frequency, nucleated bubble diameter, etc.) has been since a very active matter of research in the field of boiling heat transfer [26, 62]. With increasing experimental insights allowing to access local parameters relevant for the physics at stake close to the wall [72, 86, 109, 121, 136], the development of such models has become increasingly important both for analytic and simulation grounds. Indeed, the clear separation of the different heat fluxes is a very useful mathematical formulation for multiphase CFD computations where each term can be used as a phase-related source term at the wall [46, 52].

In the following sections, we chronologically present four different Heat Flux Partitioning models developed between 1990 and 2020. For each model, we detail the mathematical formulation of the different fluxes along with associated physical assumptions and highlight the parameters that require a dedicated closure law.

5.2 KURUL & PODOWSKI (1990)

In their original work published in 1990, Kurul & Podowski [73] proposed a complete closure for the wall heat flux partitioning. Their model is among the most referred to by many authors and has been particularly used in CMFD codes due to its simple formulation and closure laws.

Note : The wall boiling model of NCFD mostly rely on the Kurul & Podowski formulation as presented in Chapter 2.

Kurul & Podowski considered the applied heat flux to be divided between three mechanisms (Figure 5.1):

- A liquid single-phase convective heat flux $\phi_{c,L}$;
- A boiling heat flux ϕ_e ;
- A quenching heat flux ϕ_q induced by bubble movement when leaving the surface.

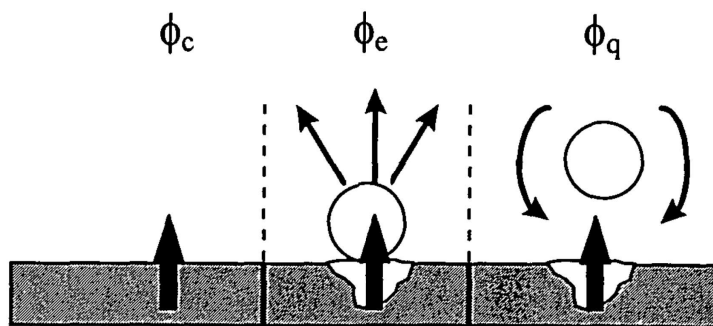


Figure 5.1: Sketch of the HFP considered by Kurul & Podowski (by Manon [87]).

The total wall heat flux being :

$$\phi_w = \phi_{c,L} + \phi_e + \phi_q \quad (5.13)$$

The convective heat flux is expressed as :

$$\phi_{c,L} = A_{c,L} \rho_L c_{p,L} U_{L,\delta} \text{St}_{L,\delta} (T_w - T_{L,\delta}) \quad (5.14)$$

with $A_{c,L}$ the portion of the wall unaffected by boiling, U_L the liquid velocity, St the Stanton number and δ a location in the buffer layer.

Assuming bubbles are spherical and leave the surface at diameter D_{lo} , they write:

$$\phi_e = \frac{1}{6} \pi D_{lo}^3 \rho_V h_{LV} f N_{sit} \quad (5.15)$$

$$(5.16)$$

with N_{sit} the nucleation site density and f the nucleation frequency.

The quenching heat flux occurring over the wait time t_w between two nucleated bubbles is computed following:

$$\phi_q = t_w f A_q \frac{2\lambda_L (T_w - T_{L,\delta})}{\sqrt{\pi \eta_L t_w}} \quad (5.17)$$

This expression corresponds to the time-average (over a time t_w) conductive heat flux from a surface at T_w towards a semi-infinite liquid medium initially at $T_{L,\delta}$ as expressed by Del Valle and Kenning [26].

They also estimate the portion of the surface affected by the bubbles as:

$$A_q = \min(1 ; F_A \pi R_{lo}^2 N_{sit}) = 1 - A_{c,L} \quad (5.18)$$

where $F_A = 4$ accounts for the bubble area of influence when leaving the surface.

One of the main hypothesis of the model is also to suppose that the bubble departure frequency f is directly related to the wait time t_w by neglecting the bubble growth time as:

$$f = \frac{1}{t_w} \quad (5.19)$$

Required closure relationships : N_{sit} , f (or t_w), D_{lo}

5.3 BASU, WARRIER & DHIR (2005)

In 2005, Basu *et al.* [3, 4] proposed a new HFP model together with a series of experiments to further study the different closure relationships required in their approach. This model was meant to account for finer descriptions of the multiple phenomena at stake in subcooled flow boiling. In particular, they account for bubble sliding and merging and thus distinguish bubble departure diameter D_d (leaving the nucleation site) and lift-off diameter D_{lo} (leaving the wall).

Their approach consist of separating the boiling flow in three regions (Figure 5.2a):

- Pre-ONB zone, where only liquid forced convection occurs, yielding:

$$\phi_w = h_{c,L} (T_w - T_L) \quad (5.20)$$

- Zone between the ONB and the OSV, prior to observing a net amount of vapor with bubble lifting off the surface. The heat flux is still totally transferred to the liquid, but the equivalent convective heat transfer coefficient $\bar{h}_{c,L}$ is supposed to be enhanced by 30% due to the presence of bubbles on the wall:

$$\phi_w = \bar{h}_{c,L} (T_w - T_L) \approx 1.3 h_{c,L} (T_w - T_L) \quad (5.21)$$

Basu *et al.* compute the ONB wall temperature as:

$$T_{w,ONB} = T_{sat} + \frac{4\sigma T_{sat}}{D_c \rho_V h_{LV}} \quad (5.22)$$

$$D_c = \sqrt{\frac{8\sigma T_{sat} \lambda_L}{\rho_V h_{LV} \phi_w}} (1 - \exp(-\theta^3 - 0.5\theta)) \quad (5.23)$$

where D_c represents the diameter of active cavities and θ the static contact angle.

- Post-OSV zone, where bubbles now leave the surface towards the bulk flow and the other parts of the HFP appear *i.e.* the boiling and quenching fluxes. The beginning of OSV is defined by Basu *et al.* using a critical liquid temperature $T_{L,OSV}$ as:

$$T_{L,OSV} = T_{sat} - 0.7 \exp \left(-0.065 \frac{D_d h_{c,L}}{\lambda_L} \right) \frac{\phi_w}{h_{c,L}} \quad (5.24)$$

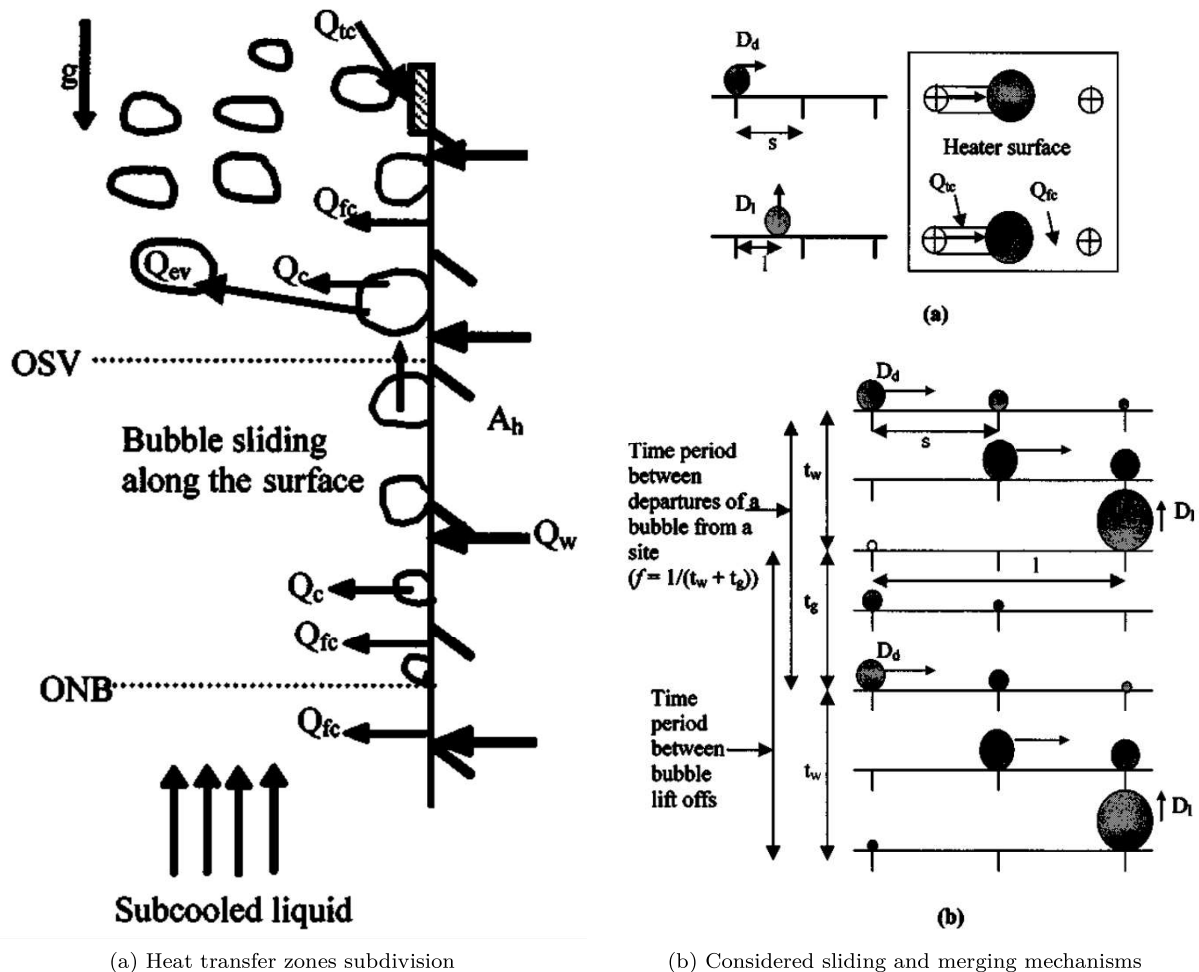


Figure 5.2: Sketch of the heat transfer zones and bubble behavior considered by Basu *et al.*. (Adapted from [3])

The hypothesis of Basu *et al.* is that the heat flux is first transferred to the superheated liquid close to the wall (by convection and transient quenching), part of which contributing to the evaporation through the liquid-vapor interface. The remaining heat is transferred to the bulk liquid (ϕ_L) either from the superheated liquid layer or bubble condensation. The whole heat transfer mechanism thus writes:

$$\phi_w = \phi_{c,L} + \phi_q = \phi_e + \phi_L \quad (5.25)$$

In order to estimate the quenching heat flux associated to bubble sliding and lift-off, Basu *et al.* consider two cases:

- 1) Bubble sliding from departure ($D = D_d$) to lift-off ($D = D_{lo}$) ;
- 2) Bubble coalescence with neighboring sites before departure.

Those two cases are distinguished using the average distance between nucleation sites s , which they suppose equal to $1/\sqrt{N_{sit}}$.

5.3.1 Case 1 : Bubble Sliding, $D_d < s$

In this case, the bubble will grow up to its departure diameter D_d and slide over a length $l_{sl,0}$ before lifting-off. If $l_{sl,0} < s$, the bubble will slide up to its lift-off diameter D_{lo} and leave the wall without colliding with other bubbles. On the contrary, if $l_{sl,0} \geq s$ the sliding bubble will merge with bubbles growing on their nucleation site, inducing a sudden growth of the bubble diameter that can exceed D_{lo} and thus trigger lift-off after sliding over a reduced length $l_{sl} < l_{sl,0}$. Those assumptions are summarized on Figure 5.2b.

If bubble coalescence occurs, the number of bubbles lifting-off the surface is lower than the actual number of nucleating sites. Basu *et al.* thus define a reduction factor:

$$R_f = \begin{cases} \frac{s}{l_{sl}} = \frac{1}{l_{sl}\sqrt{N_{sit}}} & \text{if } l_{sl,0} \geq s \\ 1 & \text{if } l_{sl,0} < s \end{cases} \quad (5.26)$$

Regarding bubble sizes, they suppose that bubbles coalesced by a sliding bubble while growing have a diameter D_d *i.e.* they were close to departure. This results in a bubble of diameter $D = (D_{sl}^3 + D_d^3)^{1/3}$ which will trigger lift-off if $D > D_{lo}$. Consequently, a sliding bubble is allowed to merge with numerous bubbles before lifting off. Noting N_{merg} the number of coalesced bubble and D_N the resulting bubble diameter, the sliding distance is:

$$l_{sl} = N_{merg}s + l_{D_N \rightarrow D_{lo}} \quad (5.27)$$

where $l_{D_N \rightarrow D_{lo}}$ is the remaining distance to slide if $D_N < D_{lo}$, being 0 if $D_N \leq D_{lo}$.

The surface swiped by the sliding bubble is then expressed as $A_{sl} = C\bar{D}l_{sl}$ with \bar{D} the average bubble diameter during sliding and C the ratio between the bubble diameter and its foot, expressed based on measurements from Maity [86] as :

$$C = 1 - \exp(2 - \theta^{0.6}) \quad (5.28)$$

After observing in their experiments that $D_d \approx 0.5D_{lo}$, Basu *et al.* choose:

$$\bar{D} = \frac{D_{lo} + D_d}{2} \approx 0.75D_{lo} \quad (5.29)$$

Defining:

$$t^* = \left(\frac{\lambda_L}{h_{c,L}}\right)^2 \frac{1}{\pi\eta_L} \quad (5.30)$$

the time at which transient conduction heat transfer becomes equal to forced liquid convection, the resulting quenching heat transfer ϕ_q is computed as:

$$\phi_q = \frac{1}{t_w + t_g} \int_0^T \frac{\lambda_L}{\sqrt{\pi\eta_L t}} (T_w - T_L) A_{sl} R_f N_{sit} dt \quad (5.31)$$

where $T = t^*$ if $t^* < t_w + t_g$ (forced convection dominates at some point during a nucleation cycle which total time is the wait time t_w plus the bubble growth time t_g) or $T = t_w + t_g$ if $t^* \geq t_w + t_g$ (transient conduction dominates over the whole nucleation cycle).

The liquid convective heat transfer is therefore:

$$\phi_{c,L} = \overline{h_{c,L}} (T_w - T_L) A_{c,L} + \overline{h_{c,L}} (T_w - T_L) A_{sl} R_f N_{sit} \left(1 - \min\left(1 ; \frac{t^*}{t_w + t_g}\right)\right) \quad (5.32)$$

with $A_{c,L} = 1 - A_{sl} R_f N_{sit}$ the wall area unaffected by bubbles.

The boiling heat flux is:

$$\phi_e = \rho_V h_{LV} \frac{\pi}{6} D_{lo}^3 R_f N_{sit} \frac{1}{t_w + t_g} \quad (5.33)$$

5.3.2 Case 2 : Bubble Coalescence without Sliding, $D_d \geq s$

Under higher wall superheats, the subsequent rise in the nucleation site density N_{sit} can lead to boiling regimes where bubbles coalesce with each other at early stages of their lifetime *i.e.* while still attached to their nucleation site. This situation is accounted for by Basu *et al.* in the case when $D_d \geq s$ by considering immediate lift-off of coalesced bubble at radius $D > D_{lo}$. In this case, the total density of bubbles leaving the surface is lower than N_{sit} and is thus reduced using:

$$R_f = \frac{s^3}{D_{lo}^3} \quad (5.34)$$

Under this massively coalescing regime, the entire surface will experience quenching due to bubble lift-off all over the heater. Depending on the values of t^* , we have:

$$\phi_q = \begin{cases} \frac{1}{t_w + t_g} \int_0^{t^*} \frac{\lambda_L}{\sqrt{\pi \eta_L t}} (T_w - T_L) dt & \text{if } t^* < t_w \\ \frac{1}{t_w + t_g} \left[\int_0^{t_w} \frac{\lambda_L}{\sqrt{\pi \eta_L t}} (T_w - T_L) dt + \int_0^T \frac{\lambda_L}{\sqrt{\pi \eta_L t}} (T_w - T_L) [1 - S_b N_{sit}] dt \right] & \text{if } t^* \geq t_w \end{cases} \quad (5.35)$$

$$\phi_{c,L} = \begin{cases} \overline{h_{c,L}} (T_w - T_L) \frac{t_w - t^*}{t_w + t_g} + \overline{h_{c,L}} (T_w - T_L) [1 - A_b N_{sit}] \frac{t_g}{t_w + t_g} & \text{if } t^* < t_w \\ \overline{h_{c,L}} (T_w - T_L) [1 - A_b N_{sit}] \frac{t_w + t_g - t^*}{t_w + t_g} & \text{if } t^* \geq t_w \end{cases} \quad (5.36)$$

with $A_b = \frac{\pi (Cs)^2}{4}$.

The boiling heat flux still expressed as Eq. 5.33.

Remark : We can note that contrary to Kurul & Podowski model, the bubble nucleation frequency is computed without neglecting the bubble growth time t_g and is thus expressed as:

$$f = \frac{1}{t_g + t_w} \quad (5.37)$$

Required closure relationships : N_{sit} , t_w , t_g , D_d , D_{lo} , $l_{sl,0}$, $h_{c,L}$.

5.4 GILMAN (2017)

A more recent HFP model dedicated to CFD simulations has been proposed in Gilman PhD work [46] and summarized in Gilman & Baglietto [47]. Among the different evolutions proposed in their work, we can mention:

- A probabilistic law to account for static interaction between nucleation sites ;
- A force-balance approach to compute the bubble departure and lift-off diameters ;
- A generic law for the enhanced forced convection coefficient accounting for bubble presence ;
- The presence of a modified quenching term accounting for local wall superheat beneath a bubble dry spot.

The total heat flux is partitioned between the liquid forced convection $\phi_{c,L}$, the solid quenching $\phi_{q,s}$, the quenching due to bubble sliding $\phi_{q,sl}$ and the evaporation flux ϕ_e . Yielding:

$$\phi_w = \phi_{c,L} + \phi_{q,s} + \phi_{q,sl} + \phi_e \quad (5.38)$$

The convective term is computed in a way similar to Basu *et al.* [3] in Eq. 5.32:

$$\phi_{c,L} = h_{c,L} (1 - A_{sl} N_{sit,a}) (T_w - T_L) + \overline{h_{c,L}} A_{sl} N_{sit,a} \left(1 - \frac{t^*}{t_w + t_g} \right) (T_w - T_L) \quad (5.39)$$

where $N_{sit,a}^*$ is the active nucleation site density that will generate sliding bubbles, that can differ from the empirical value of available sites N_{sit} usually computed by a correlation. The time t^* is the same time as in Eq. 5.30, A_{sl} the bubble sliding area, t_w and t_g respectively the wait and bubble growth times.

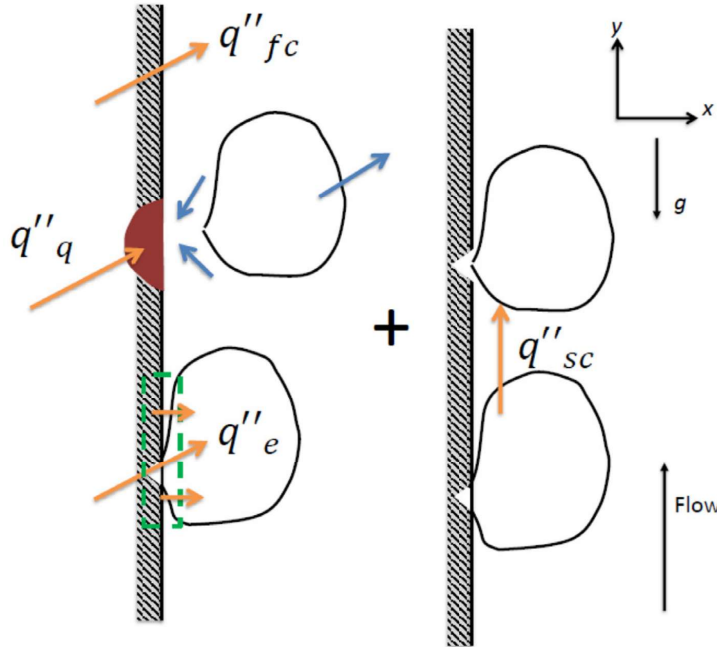


Figure 5.3: Heat Flux Partitioning considered by Gilman [46] (Adapted from [47]).

The actually active nucleation site density $N_{sit,a}$ (that will generate bubbles) is considered by Gilman to be smaller than N_{sit} by considering a static interaction between the available sites *i.e.* the fact that a bubble laying on a site may be blocking nucleation from an other site laying beneath its foot. Following a so-called Complete Spatial Randomness (CSR) approach, they express the probability \mathcal{P} to find a site under a growing bubble of radius R_d as:

$$\mathcal{P} = 1 - e^{-N_b \pi R_d^2} \quad (5.40)$$

where $N_b = \frac{t_g}{t_w + t_g} N_{sit} = t_g f N_{sit}$ is the density of bubbles covering the heated surface.

The number of active sites is then computed as:

$$N_{sit,a} = (1 - \mathcal{P}) N_{sit} = \exp\left(-\frac{t_g}{t_w + t_g} N_{sit} \pi R_d^2\right) N_{sit} \quad (5.41)$$

This value is then reduced by Gilman to obtain the density of sites generating sliding bubbles $N_{sit,a}^*$ using a reduction factor accounting for sliding bubble coalescence (similar to Basu *et al.* in Eq. 5.26):

$$N_{sit,a}^* = R_f N_{sit,a} = \frac{s}{l_{sl,0} + s} N_{sit,a} \quad (5.42)$$

where $l_{sl,0}$ is the sliding length of a single bubble and $s = 1/\sqrt{N_{sit,a}}$.

The sliding quenching term is also computed in a similar to Basu *et al.* as:

$$\phi_{q,sl} = \frac{2\lambda_L (T_w - T_L)}{\sqrt{\pi\eta_L t^*}} A_{sl} N_{sit,a}^* \quad (5.43)$$

$$A_{sl} = \overline{D} l_{sl} = \frac{D_d + D_{lo}}{2} (N_{merg}s + l_{D_N \rightarrow D_{lo}}) \quad (5.44)$$

Regarding the boiling heat flux, Gilman splits it in two contributions respectively associated with the inception of nucleation ($\phi_{e,init}$) and liquid microlayer evaporation ($\phi_{e,ML}$):

$$\phi_e = \phi_{e,init} + \phi_{e,ML} \quad (5.45)$$

$$= \frac{4}{3} \pi R_d^3 \rho_V h_{LV} \frac{1}{t_w + t_g} N_{sit,a} + V_{ML} \rho_L h_{LV} \frac{1}{t_w + t_g} N_{sit,a} \quad (5.46)$$

$$V_{ML} = \frac{2}{3} \pi \left(\frac{R_d}{2}\right)^3 \delta_{max} \quad (5.47)$$

where $\delta_{max} = 2 \mu\text{m}$ is the largest bubble microlayer thickness based on experiments from Gerardi [44].

Finally, the solid quenching term is written as:

$$\phi_{q,s} = \rho_w c_{p,w} V_q \Delta T_q \frac{1}{t_g + t_w} N_{sit,a} \quad (5.48)$$

$$V_q = \frac{2}{3} \pi r_w^2 \quad (5.49)$$

with subscript w denoting the wall properties, r_w the dry patch radius and $\Delta T_q = 2 K$ the extra wall superheat as suggested by Gerardi *et al.* [45].

Required closure relationships : N_{sit} , t_w , t_g , D_d , D_{lo} , $l_{sl,0}$, $h_{c,L}$, $\bar{h}_{c,L}$.

5.5 KOMMAJOSYULA (2020)

The last HFP model we will look through in this Chapter was proposed by Kommajosyula [71] in the continuation of Gilman [46] work. In particular, he proposed:

- A finer modeling of the bubble microlayer evaporation ;
- Simpler empirical correlations for closure parameters such as bubble departure diameter and wait time ;
- A modification of the probabilistic approach for the static interaction between sites.

The total heat flux is partitioned by Kommajosyula between four fluxes : the forced liquid convection $\phi_{c,L}$, the sliding conduction $\phi_{q,sl}$, the evaporation ϕ_e and a direct convective flux to the vapor ϕ_{vap} . Using the wall dry area S_{dry} , he writes:

$$\phi_w = (1 - S_{dry}) (\phi_{c,L} + \phi_{q,sl} + \phi_e) + S_{dry} \phi_{vap} \quad (5.50)$$

The liquid convective term is expressed as:

$$\phi_{c,L} = (1 - S_{sl}) h_{c,L} (T_w - T_L) \quad (5.51)$$

where S_{sl} is the surface covered by sliding bubbles.

Assuming that the transient conduction during quenching operates during the time t^* (Eq. 5.30), Kommajosyula rewrites the total quenching flux using the forced-convection heat transfer coefficient as:

$$\phi_{q,sl} = 2h_{c,L} A_{sl} N_{sit,a} \frac{t^*}{t_g + t_w} (T_w - T_L) \quad (5.52)$$

$$A_{sl} = \frac{1}{\sqrt{N_{sit,a}}} \frac{D_d + D_{lo}}{2} \quad (5.53)$$

with $N_{sit,a}$ the active nucleation site density, D_d and D_{lo} respectively the bubble departure and lift-off diameters.

The total sliding surface is then expressed as:

$$S_{sl} = \min (1 ; A_{sl} N_{sit,a} t^* f) \quad (5.54)$$

The evaporation heat flux is based on Gilman approach by splitting it between inception and microlayer evaporation:

$$\phi_e = \phi_{e,init} + \phi_{e,ML} \quad (5.55)$$

$$= \frac{4}{3} \pi \left(\frac{D_{init}}{2} \right)^3 \rho_V h_{LV} f N_{sit,a} + V_{ML} \rho_V h_{LV} f N_b \quad (5.56)$$

The microlayer terms are modeled based on the contact angle θ and the capillary number $\text{Ca} = \frac{\mu_L U_b}{\sigma}$, where U_b is the bubble interface velocity, as:

$$D_{init} = D_d \max(1 ; 0.1237 \text{Ca}^{-0.373} \sin(\theta)) \quad (5.57)$$

$$V_{ML} = \delta_{ML} D_{ML}^2 \frac{\pi}{12} \left(2 - \left(\frac{D_{dry}}{D_{ML}} \right)^2 - \frac{D_{dry}}{D_{ML}} \right) \quad (5.58)$$

with $D_{ML} = D_{init}/2$ and $\frac{D_{dry}}{D_{ML}} = \max(1 ; 0.1237 \text{Ca}^{-0.373} \sin(\theta))$.

The microlayer thickness δ_{ML} is expressed as:

$$\delta_{ML} = 4 \times 10^{-6} \sqrt{\frac{\text{Ca}}{\text{Ca}_0}} \quad (5.59)$$

with $\text{Ca}_0 = 2.16 \times 10^{-4} \Delta T_w^{1.216}$.

The active nucleation site density $N_{sit,a}$ is computed based on the Complete Spatial Randomness approach proposed by Gilman. However, it is expressed using Lambert's W-function \mathcal{W} as:

$$N_{sit,a} = \frac{\mathcal{W}\left(f t_g \pi \frac{D_d^2}{4} N_{sit}\right)}{f t_g \pi \frac{D_d^2}{4}} \quad (5.60)$$

with \mathcal{W} being approximated to avoid an implicit solving of this equation.

Required closure relationships : N_{sit} , t_w , t_g , D_d , D_{lo} , $h_{c,L}$.

5.6 CONCLUSION

As we have seen, the HFP approach is widely studied since decades and is still an active field of work to hopefully reach an exhaustive and precise modeling of all the heat transfer phenomena that are at stake in wall boiling. While most models are similar to each other regarding terms such as single-phase convection or transient conduction heat transfer, they may differ in their methods to account for bubble sliding, microlayer evaporation or modeling of the bubble nucleation cycle.

Moreover, each of those approaches requires a certain number of closure laws to compute important physical parameters among which we can in particular cite:

- The nucleation site density N_{sit} ;
- The bubble nucleation period / frequency : $f = \frac{1}{t_g + t_w}$;
- The bubble departure and lift-off diameters D_d and D_{lo} .

In this global framework, we will propose the development of a new HFP model by first trying to have a close look at boiling bubble dynamics to propose an acceptable modeling of a bubble lifetime growing and sliding on the wall (Chapter 6). Then, we will tackle the problem of the closure laws aiming to compute important yet highly uncertain parameters (N_{sit} , t_w , etc.) before proposing a final formulation for the HFP that will be compared to experimental measurements (Chapter 7). In order to complete the description of the aforementioned models, we will highlight throughout the development when a given closure law is used in one of the presented models.

6

BOILING BUBBLE DYNAMICS

Contents

6.1	Introduction	62
6.1.1	Experimental Insights	62
6.1.2	Existing Approaches	64
6.2	Bubble Force Balance in Vertical Flow Boiling	68
6.2.1	Introduction	68
6.2.2	General Considerations	69
6.2.3	Buoyancy and Contact Pressure Force	70
6.2.4	Capillary Force	70
6.2.5	Drag and Lift Forces	71
6.2.6	Inertia Force	76
6.2.7	Force Balance Summary	78
6.2.8	Liquid Velocity	79
6.3	Bubble Growth	81
6.3.1	Introduction	81
6.3.2	Heat Diffusion in Uniformly Superheated Liquid	81
6.3.3	Microlayer Evaporation	82
6.3.4	Bubble Growth in Subcooled Flow Boiling	83
6.3.5	Analytic Approach of Bubble Growth in a Linear Thermal Boundary Layer .	84
6.3.6	Comparison with DNS Results	87
6.3.7	Comparison with Experimental Measurements	88
6.3.8	Conclusions on Bubble Growth Modeling	91
6.4	Departure by Sliding	91
6.4.1	Non-Dimensional Analysis	91
6.4.2	Application to Experimental Data	93
6.4.3	Departure Diameter Prediction	95
6.4.4	Discussion and accounting for parameters uncertainties	97
6.5	Sliding phase	99
6.5.1	Modeling	99
6.5.2	Low Pressure Sliding	100
6.5.3	High Pressure Sliding	100
6.5.4	Comparison of Forces in Sliding Stage	101
6.6	Bubble Lift-Off	102
6.6.1	Introduction	102
6.6.2	Experimental Measurements of Lift-Off Diameter	106
6.6.3	Influence of the Flow Boiling Conditions	106
6.6.4	Predicting the Lift-Off with a Force Balance	107
6.6.5	A Simple Non-Dimensional Correlation	110
6.6.6	Conclusion on the Lift-Off	110
6.7	Conclusion	111

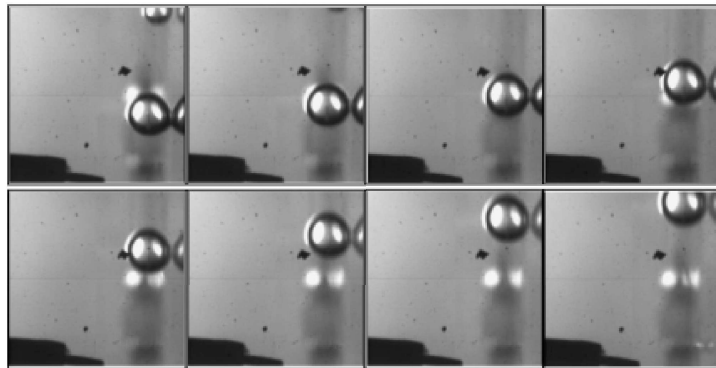
6.1 INTRODUCTION

Dynamics of boiling bubbles is playing an important role in the Heat Flux Partitioning models. For instance, the evaporation heat flux ϕ_e is directly proportional to the bubble lift-off radius R_{lo} 5.16 while the quenching heat flux ϕ_q depends on the wall area visited by a bubble $A_{q,1b}$ (Eq. 5.43) which depends on the bubble sliding length l_{sl} , departure radius R_d and lift-off radius R_{lo} .

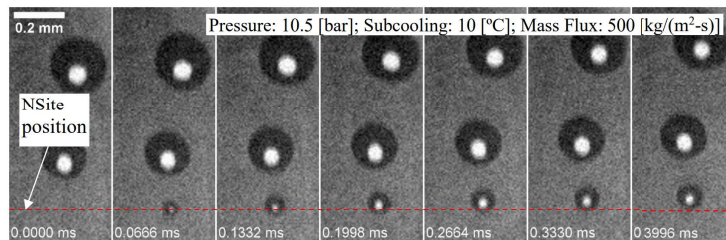
6.1.1 Experimental Insights

Consequently, many experimental investigations have been conducted to further understand the behavior of nucleated bubbles on a wall of a liquid flow. In the case of vertical flow boiling, a typical bubble life cycle can be described as follows:

- Beginning of nucleation, growth while attached to the nucleation site ;
- Detachment occurring when the bubble has a radius R_d , from which the bubble will start to slide and accelerate along the wall while continuing to grow ;
- Lift-off from the wall when the bubble reaches a radius R_{lo} after sliding over a length l_{sl} .



(a) Bubble sliding visualized and adapted from Maity [86] at atmospheric pressure.



(b) Bubble sliding visualized and adapted from Kossolapov [72] at higher pressure.

Figure 6.1: Visualization of bubble sliding at various pressures.

This behavior has been supported by many experimental observations who clearly observed three stages (departure, sliding, lift-off) both at low pressure (Maity [86], Situ [117], Thorncroft [125], Prodanovic [103], Chen [15], Ren [107], etc.) and high pressure (March [88], Kossolapov [72]). Altogether, those works cover various flow conditions and operating fluids which demonstrate the dominance of this bubble behavior in vertical flow boiling. Examples from the literature of visualizations of bubble sliding at atmospheric and high pressure are reproduced on Figure 6.1.

The bubble sliding process has also been thermally studied through experiments to quantify its impact on the wall heat transfer. Estrada-Perez *et al.* [33] observed the significant thermal impact of sliding bubbles footprints. Kossolapov [72] also investigated the sliding of boiling bubbles and measured the magnitude of the transient heat transfer induced by the disruption of the liquid thermal boundary layer in the bubble's wake. Typical experimental observations from those works are reproduced on Figure 6.2

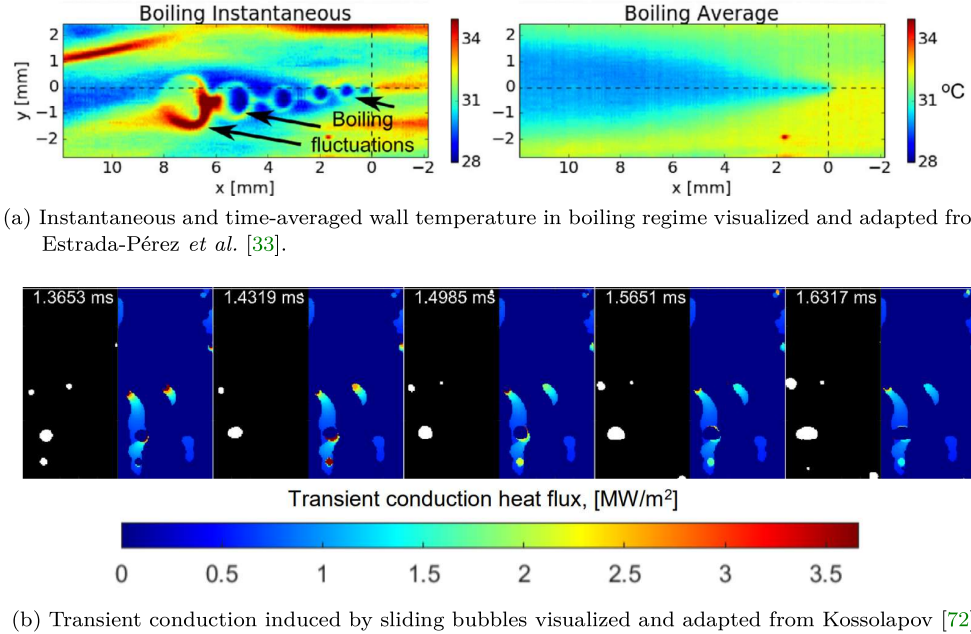


Figure 6.2: Visualization of bubble sliding thermal impact.

Those experimental observations highlight the significant magnitude of the transient heat transfer triggered by bubble movement on the wall that can represent up to 40% of the total wall heat flux [72]. All the aforementioned observations are summed-up on Figure 6.3.

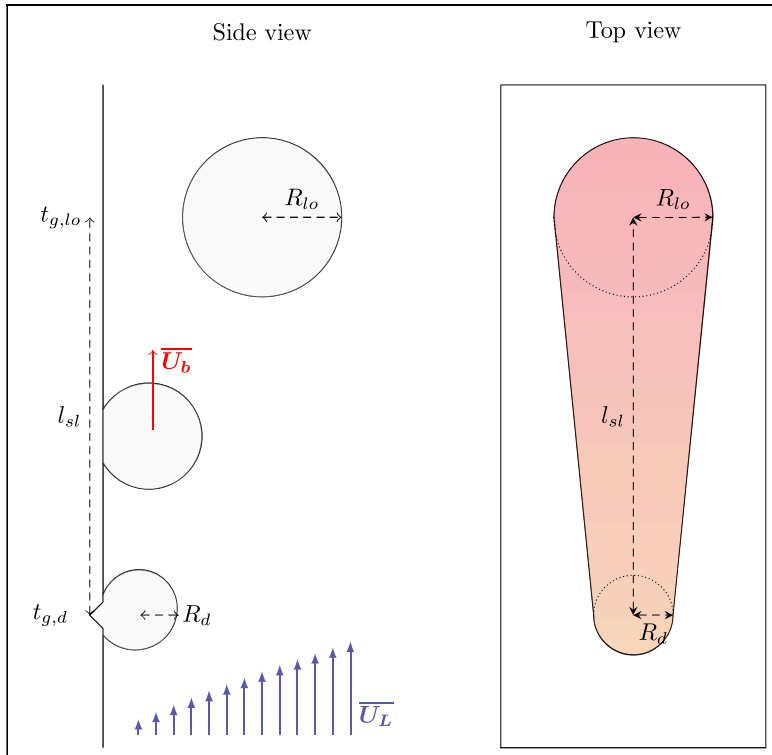


Figure 6.3: Sketch of a typical bubble lifetime in vertical flow boiling. Left depicts a typical side view of the heater with identification of departure, sliding and lift-off. Right depicts a top view of the heater, exhibiting the area that will undergo transient heat transfer.

Predicting the HFP in vertical flow boiling thus requires a description of single bubble dynamics that includes accurate estimations of bubble departure and lift-off radii R_d and R_{lo} as well as bubble sliding velocity $\overline{U_b}$ to predict the sliding length l_{sl} .

6.1.2 Existing Approaches

6.1.2.1 Departure / Lift-Off Diameters

Historically, first approaches to estimate the bubble diameter consisted of experimental-based correlations for pool boiling of horizontal surfaces through photographic studies. In those cases, departure from the nucleation site coincides with the bubble lift-off. Among the mainly used in HFP models and CFD, we can mention the law of Tolubinsky & Kostanchuk (1970)[127] that estimates the lift-off diameter D_{lo} based on the local liquid subcooling $\Delta T_L = T_{sat} - T_L$ with T_L the liquid temperature:

$$D_{lo} = D_0 e^{-\Delta T_L/45}, \quad D_0 = 15\text{mm} \quad (6.1)$$

On the other hand, authors such as Cole & Rohsenow (1968) (mentioned in [69]) proposed relationships including the influence of pressure through the capillary length $L_c = \sqrt{\frac{\sigma}{g(\rho_L - \rho_V)}}$:

$$D_{lo} = CL_c \left(\frac{\rho_L c_{p,L} T_{sat}}{\rho_V h_{LV}} \right)^{5/4} \quad (6.2)$$

$C = 1.5 \times 10^{-4}$ for water and 4.65×10^{-4} otherwise.

This equations provides a good trend for the evolution of bubble departure diameter with pressure for pool boiling as shown by Kossolapov [72].

More recently, the developments around HFP models has lead meany researchers to propose dedicated correlations for bubble departure or lift-off diameter. For instance, Zhou *et al.* (2021) [143] proposed simple correlations for the departure and lift-off diameter in horizontal flow boiling at low pressure based on their experiments:

$$\frac{D_d}{L_o} = 10^{2.4086} \left(\frac{\rho_V}{\rho_L} \right)^{-0.6613} \text{Ja}_w^{* 0.1557} \text{Ja}_L^{* -0.01592} \text{Re}_{L_o}^{-0.6647} \text{Pr}_L^{-1.8477} \sin(\theta_s)^{0.4} \quad (6.3)$$

$$\frac{D_{lo}}{L_c} = 10^{-1.1990} \left(\frac{\rho_V}{\rho_L} \right)^{-0.9785} \text{Ja}_w^{* 0.1435} \text{Ja}_L^{* -0.0119} \text{Re}_{L_c}^{-0.5129} \text{Pr}_L^{-1.8784} \quad (6.4)$$

with the Reynolds numbers based on $L_o = \frac{\rho_L \nu_L^2}{\sigma}$ and L_c the capillary length, and $\text{Ja}^* = \frac{c_{p,L} \Delta T}{h_{LV}}$ (ΔT either the wall superheat or liquid subcooling) reduced Jakob numbers that do not include the density ratio.

In the case of vertical flow boiling, Ünal (1976)[149] derived a correlation based on a semi-analytical approach of the heat transfer mechanisms around a bubble to estimate its maximum diameter, including simultaneous influences of pressure, heater material, liquid velocity and subcooling:

$$D_{lo} = 2.42 \times 10^{-5} P^{0.709} \frac{a}{\sqrt{b\varphi}} \quad (6.5)$$

$$a = \frac{\Delta T_w \lambda_w}{2\rho_V h_{LV} \sqrt{\pi \eta_w}}$$

$$b = \frac{\Delta T_L}{2(1 - \rho_V/\rho_L)}$$

$$\varphi = \max \left(1 ; \left(\frac{U_L}{U_0} \right)^{0.47} \right), \quad U_0 = 0.61 \text{ m/s}$$

Ünal validated his law against several measurements from the literature covering pressures from 1 to 177 bars, liquid velocities from 0.08 to 9.15 m/s, subcoolings from 3 to 86K and heat fluxes from 0.47 to 10.64 MW/m².

Note : The law of Ünal is used in the HFP model of Kurul & Podowski. It as also implemented in NEPTUNE_CFD and includes a correction of Borée *et al.* (Eq. 2.39) to avoid divergence in bubble diameter when reaching saturated conditions.

In the framework of their HFP model development, Basu *et al.* fitted expressions for D_d and D_{lo} based on their own measurements in vertical flow boiling at atmospheric pressure:

$$\frac{D_d}{L_c} = 1.3 \sin(\theta_s)^{0.4} [0.13 e^{-1.75 \times 10^{-4} Re_{L,D_h}} + 0.005] Ja_w^{0.45} e^{-0.0065 Ja_L} \quad (6.6)$$

$$\frac{D_{lo}}{L_c} = 1.3 \sin(\theta_s)^{0.4} [0.2 e^{-1.28 \times 10^{-4} Re_{L,D_h}} + 0.005] Ja_w^{0.45} e^{-0.0065 Ja_L} \quad (6.7)$$

They were validated for $14 \leq Ja_w \leq 56$, $1 \leq Ja_L \leq 138$, $0 \leq Re_{L,D_h} \leq 7980$ and $30^\circ \leq \theta_s \leq 90^\circ$.

Note : Basu *et al.* use these own-developed laws in their HFP formulation to estimate bubble diameters.

Similarly, Kommajosyula[71] gathered several bubble departure and lift-off diameter measurements from the literature (both in vertical and horizontal boiling) and proposed the following reduced correlation:

$$D_d = 18.9 \times 10^{-6} \left(\frac{\rho_L - \rho_V}{\rho_V} \right)^{0.27} Ja_w^{0.75} (1 + Ja_L)^{-0.3} U_{L,bulk}^{-0.26} \quad (6.8)$$

$$D_{lo} = 1.2 D_d \quad (6.9)$$

Note : This formulation is used in Kommajosyula's HFP model. Having a proportionality between D_d and D_{lo} allows the comparison with a database gathering both departure and lift-off diameter measurements.

Although this law presents coherent trends with flow conditions, the raw presence of $U_{L,bulk}$ in the expression is questionable because:

- The relationship is not dimensionless and the constant 18.9×10^{-6} must be in $\text{m}^{1.26} \cdot \text{s}^{-0.26}$;
- The negative exponent will yield diverging values when reaching pool boiling conditions, which is physically inconsistent.

In order to show the spread of predicted values by the presented correlations, we plot them for water at low and high pressure on Figure 6.4.

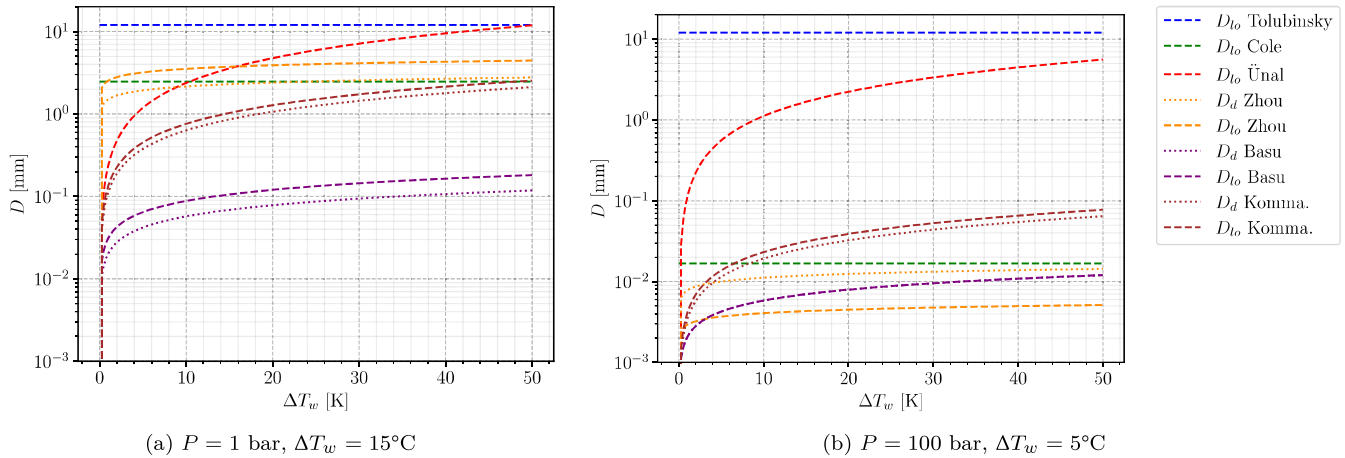


Figure 6.4: Values predicted by the diameter correlations for water. $\Delta T_L = 10^\circ\text{C}$, $G_L = 1000 \text{ kg/m}^2/\text{s}$, $\theta = 40^\circ$ and $D_h = 10 \text{ mm}$.

We observe that altogether, the predicted values for both for departure and lift-off diameters spread at least over a decade, with a global decrease if pressure is increased. Correlations of Basu, Kommajosyula and Zhou seem to present pressure dependency similar to that of Cole & Rohsenow. On the other

hand, Ünal correlation appears to weakly change with pressure, its value being more controlled by the wall superheat. Tolubinsky correlation depending solely on the liquid subcooling obviously present no variation.

6.1.2.2 Sliding Length and Velocity

Regarding bubble sliding phase, one of the most used correlations to predict bubble diameter evolution has been developed by Maity [86]. Based on atmospheric pressure visualization of boiling single bubbles in water, it predicts the resulting sliding diameter D_{sl} provided a sliding time t_{sl} and an arbitrary initial diameter D_{in} (not obligatorily the departure diameter) through:

$$\frac{(D_{sl}^2 - D_{in}^2)}{t_{sl}\eta_L \text{Ja}_w} = \frac{1}{15(0.015 + 0.023 \text{Re}_b^{0.5})(0.04 + 0.023 \text{Ja}_L^{0.5})} \quad (6.10)$$

where $\text{Re}_b = \frac{U_L D_b}{\nu_L}$

Using Maity measurements of bubble sliding velocity, Basu *et al.* proposed an estimation of the sliding distance for a single bubble $l_{sl,0}$:

$$l_{sl,0} = \int_0^{t_{sl}} U_b \, dt = \int_0^{t_{sl}} C_U \sqrt{t} \, dt = \frac{2}{3} C_U t_{sl}^{3/2} \quad (6.11)$$

$$C_U = 3.2 U_L + 1 \quad (6.12)$$

where C_U represents a correlated acceleration coefficient.

Note : Basu *et al.* use this correlation along with Eq. 6.10 in their model to estimate the bubble sliding and growth.

The estimation of the bubble sliding velocity through an explicit correlation is difficult since it varies over the bubble lifetime. Therefore, some authors simply suppose that $U_b = U_L$ such as Gilman & Baglietto who also use Eq. 6.10 for the sliding growth.

Other assumptions regarding the sliding length relies on the value of the bubble-generating site density on the heater $N_{sit,a}$. Supposing that bubbles usually lift-off after sliding a distance between two active sites gives:

$$l_{sl} = \frac{1}{\sqrt{N_{bub}}} \quad (6.13)$$

Note : This modeling choice is made by Kommajosyula.

6.1.2.3 Conclusion on Correlations

Albeit proposing coherent trend with the flow boiling conditions along with good estimations of the desired parameters on given experimental datasets, explicit correlations inherently include a limited range of application. Moreover, the constant increase of the number of works proposing data-fitted laws makes the selection of a proper relationship a complicated matter due to their potential lack of generality.

To try to overcome this drawback and come up with more generalized models, researchers have explored an alternative approach by developing Mechanistic Models based on a force-balance to precisely depict the external efforts experienced by the growing bubble. The goal is to compute the sum of the forces applied to the bubble over its growing time and to detect departure and lift-off events using associated criteria such as a change in the force balance sign. This will be the subject of the next section.

As a summary, we gather the presented correlations on Table 6.1.

Bubble Departure Diameter	
Author (Year)	Correlation
Basu <i>et al.</i> (2005)	$\frac{D_d}{L_c} = 1.3 \sin(\theta_s)^{0.4} \left[0.13 e^{-1.75 \times 10^{-4} \text{Re}_{L,D_h}} + 0.005 \right] \text{Ja}_w^{0.45} e^{-0.0065 \text{Ja}_L}$ $L_c = \sqrt{\frac{\sigma}{g(\rho_L - \rho_V)}}$
Kommajosyula (2020)	$D_d = 18.9 \times 10^{-6} \left(\frac{\rho_L - \rho_V}{\rho_V} \right)^{0.27} \text{Ja}_w^{0.75} (1 + \text{Ja}_L)^{-0.3} U_{L,bulk}^{-0.26}$
Zhou (2021)	$\frac{D_d}{L_o} = 10^{2.4086} \left(\frac{\rho_V}{\rho_L} \right)^{-0.6613} \text{Ja}_w^*^{0.1557} \text{Ja}_L^*^{-0.01592} \text{Re}_{L_o}^{-0.6647} \text{Pr}_L^{-1.8477} \sin(\theta_s)^{0.4}$ $L_o = \frac{\rho_L \nu_L^2}{\sigma}$
Bubble Lift-Off Diameter	
Author (Year)	Correlation
Tolubinsky & Kostanchuk (1970)	$D_{lo} = D_0 e^{-\Delta T_L / 45}, D_0 = 15 \text{mm}$
Cole & Rohsenow (1968)	$D_{lo} = CL_c \left(\frac{\rho_L c_{p,L} T_{sat}}{\rho_V h_{LV}} \right)^{5/4}$ $C = 1.5 \times 10^{-4} \text{ (water)} \text{ or } 4.65 \times 10^{-4} \text{ (other)}, L_c = \sqrt{\frac{\sigma}{g(\rho_L - \rho_V)}}$
Ünal (1976)	$D_{lo} = 2.42 \times 10^{-5} P^{0.709} \frac{a}{\sqrt{b\varphi}}, a = \frac{\Delta T_w \lambda_w}{2\rho_V h_{LV} \sqrt{\pi \eta_w}}$ $b = \frac{\Delta T_L}{2(1 - \rho_V/\rho_L)}, \varphi = \max \left(1 ; \left(\frac{U_L}{U_0} \right)^{0.47} \right), U_0 = 0.61 \text{ m/s}$
Basu <i>et al.</i> (2005)	$\frac{D_{lo}}{L_c} = 1.3 \sin(\theta_s)^{0.4} \left[0.2 e^{-1.28 \times 10^{-4} \text{Re}_{L,D_h}} + 0.005 \right] \text{Ja}_w^{0.45} e^{-0.0065 \text{Ja}_L}$ $L_c = \sqrt{\frac{\sigma}{g(\rho_L - \rho_V)}}$
Kommajosyula (2020)	$D_{lo} = 1.2 D_d$
Zhou (2021)	$\frac{D_{lo}}{L_c} = 10^{-1.1990} \left(\frac{\rho_V}{\rho_L} \right)^{-0.9785} \text{Ja}_w^*^{0.1435} \text{Ja}_L^*^{-0.0119} \text{Re}_{L_c}^{-0.5129} \text{Pr}_L^{-1.8784}$ $L_c = \sqrt{\frac{\sigma}{g(\rho_L - \rho_V)}}$
Sliding Length, Diameter and Velocity	
Author (Year)	Correlation
Maity (2000)	$\frac{(D_{sl}^2 - D_{in}^2)}{t_{sl} \eta_L \text{Ja}_w} = \left[15 \left(0.015 + 0.023 \text{Re}_b^{0.5} \right) \left(0.04 + 0.023 \text{Ja}_L^{0.5} \right) \right]^{-1}$ $\text{Re}_b = \frac{U_L D_b}{\nu_L}$
Basu <i>et al.</i> (2005)	$l_{sl,0} = \frac{2}{3} C_U t_{sl}^{3/2}, C_U = 3.2 U_L + 1$
Bubble Density Average Distance	$l_{sl} = \frac{1}{\sqrt{N_{bub}}}$

Table 6.1: Summary of the presented correlations

6.2 BUBBLE FORCE BALANCE IN VERTICAL FLOW BOILING

6.2.1 Introduction

The derivation of the force balance over a growing bubble on a wall in a liquid flow is a very complicated problem that many researchers have tried to tackle over the past decades. Many theoretical and numerical approaches have been conducted to estimate the forces at stake in bubble dynamics and sometimes compared to experimental visualization of bubbles in movement.

Among the first propositions of the whole force-balance closure, the work of Klausner *et al.* in 1993 [66] is probably among the most referred to. They proposed a tentatively complete force-balance for a growing bubble in a boiling flow and supposed that departure from the nucleation site is reached when the force balance becomes positive either in the direction of the flow or perpendicular to the wall. They validated their approach against measurements for horizontal flow boiling of refrigerant R113.

In the same framework, many subsequent works were published such as:

- Van Helden *et al.* [132] (1995) who assessed forces coefficients using injected air bubbles in a vertical flow ;
- Thorncroft *et al.* [125, 126] (1998, 2001) who conducted experiments on horizontal and vertical flow boiling of R113 while proposing more general formulations of the force balance that were used to predict bubble diameter measurements ;
- Duhar & Colin [32] (2006) who validated a force balance on bubbles created by air injection in a shear flow. They extended their work with boiling N-pentane experiments and studied the growth and detachment of single bubbles [30] ;
- Van Der Geld (2009) [43] used potential flow theory to analytically derive the force balance for deforming bubbles near a plane ;
- Sugrue *et al.* (2014) [121] conducted measurements on boiling bubble for water at atmospheric pressure and various surface orientations. Their measurements were then used to validate a force-balance approach predicting bubble departure by sliding [120] ;
- Mazzocco *et al.* (2018) [89] gathered several measurements of bubble departure and lift-off diameters and proposed a reassessed force-balance approach including new drag coefficient and growth law to achieve predictions with a reasonable accuracy over the database ;
- Ren *et al.* (2020) [107] measured bubble departure diameter for vertical flow boiling of water up to 5 bars which they used to validate a force-balance model.

While not exhaustive, this list aims to show that force-balance modeling has become an increasingly interesting approach for authors. It is though not exempted of limitations because each force requires a proper modeling which needs sometimes to go through empirical choices as we will later discuss. This drawback is particularly noted by Bucci *et al.* [11] who points out that traditional force balances are not equal to zero when the bubble is immobile. On the other hand, they show that this is not due to the absence of unknown forces in the balance but rather associated to the computation of well-known forces such as capillary forces. Moreover, Duhar & Colin [32] managed to reach a zero total balance for their air-injected bubbles, and emphasized the interest of force modeling to deeper understand the physical phenomena behind bubble dynamics. The difficulty to close the balance of the forces in the case of a boiling bubble is due to the approximated expression of the forces which expressions are expected to be more complicated in the case of a phase change compared to air injection.

Each of the previously listed models proposed different upgrades and modifications to the force balance over the bubble. Unfortunately, they were all validated using low pressure experiments due to the lack of pressurized measurements in the literature. In addition, the mentioned common use of empirical parameters makes it difficult to reach a general validation of those models as we will see.

Note : The HFP model of Gilman & Baglietto [47] is based on such a force balance for departure and lift-off prediction.

In this section, we aim to propose an update of the bubble force balance for vertical flow boiling with a reduced empiricism and to cover the whole bubble lifetime (departure, sliding, lift-off) while achieving a larger generality by including pressurized measurements up to 40 bar conducted by Kossolapov [72].

6.2.2 General Considerations

When trying to derive the force balance over a bubble, the first step consists of splitting the whole effort experienced by the bubble between different contributions depending on their nature. In our case, we focus on a bubble growing on a vertical wall and facing an upward flow as depicted in Figure 6.5.

The static forces are :

- The buoyancy force $\overline{F_B}$, including Archimedes force and the weight of the bubble ;
- The capillary or surface tension force $\overline{F_C}$;
- The contact pressure force $\overline{F_{CP}}$.

The hydrodynamic forces are :

- The drag and lift forces $\overline{F_D}$ and $\overline{F_L}$;
- The inertia force $\overline{F_I}$, including added-mass and Tchen force.

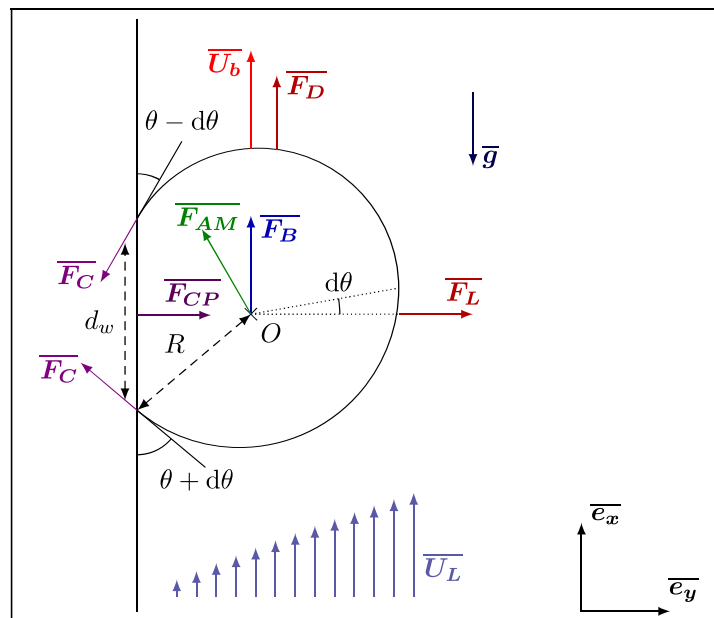


Figure 6.5: Sketch of the forces applied to the bubble facing an upward flow $\overline{U_L}$ and sliding at velocity $\overline{U_b}$

Regarding the bubble shape, we consider a quasi-spherical bubble of radius R with a circular contact area with the wall of radius r_w .

Remark : This assumption is mainly supported for high pressure boiling where bubble elongation and deformation is not observed [72]. At lower pressure, the bubble shape can somewhat deviate from a spherical shape especially before lift-off. It seems however reasonably quasi-spherical at early growth stages [86].

The bubble has a static contact angle θ and is tilted under the influence of the flow by an inclination angle $d\theta$ (half the total angle hysteresis). The resulting downstream and upstream contact angles are therefore $\theta_d = \theta - d\theta$ and $\theta_u = \theta + d\theta$. If the bubble has a shape close to a truncated sphere, we can approximate the bubble foot radius as:

$$r_w \approx R \sin \left(\frac{\theta_u + \theta_d}{2} \right) = R \sin (\theta) \quad (6.14)$$

Some authors rather take $r_w \approx \frac{1}{2}R (\sin(\theta_u) + \sin(\theta_d)) = R \sin(\theta) \cos(d\theta)$, however this expression tends to zero when reaching $d\theta \rightarrow 90^\circ$ which is undesirable regarding the expression of forces such as Contact Pressure and Surface Tension.

We suppose $V_b \approx \frac{4}{3}\pi R^3$ for the bubble volume.

6.2.3 Buoyancy and Contact Pressure Force

Following the work of Thorncroft *et al.* [126] and Duhar & Colin [32], the global force balance for a bubble growing on a wall can be written as:

$$\underbrace{\frac{4}{3}\pi R^3 \rho_V \bar{g}}_{\text{Bubble weight}} + \overline{F_C} - \underbrace{\int_{S_b} (P_L - \rho_L g z) \bar{n} \, dS}_{\text{Outer liquid pressure}} - \underbrace{\int_{S_w} P_V \bar{n} \, dS}_{\text{Inner vapor pressure}} + \underbrace{\int_{S_b} \overline{\tau_L} \cdot \bar{n}}_{\text{Viscous efforts}} = \bar{0} \quad (6.15)$$

where \bar{n} is the local normal unity vector, S_b is the bubble surface facing the liquid, S_w the wall-contact area and $\overline{\tau_L}$ the deviatoric stress tensor associated to viscous effects.

Re-writing the two pressure integrals versus the liquid pressure at the wall P_0 yields:

$$\begin{aligned} - \int_{S_b} (P_L - \rho_L g z) \bar{n} \, dS - \int_{S_w} P_V \bar{n} \, dS &= - \int_{S_b + S_w} (P_0 - \rho_L g z) \bar{n} \, dS + \int_{S_w} (P_0 - \rho_L g z - P_V) \bar{n} \, dS \\ &\quad - \int_{S_b} (P_L - P_0) \bar{n} \, dS \\ &= \int_{S_b + S_w} \rho_L g z \bar{n} \, dS + \int_{S_w} (P_0 - P_V) \bar{n} \, dS \\ &\quad - \int_{S_b} (P_L - P_0) \bar{n} \, dS \end{aligned} \quad (6.16)$$

Summing the first term on the RHS of Eq. 6.16 with the bubble weight results in the buoyancy force:

$$\overline{F_B} = V_b (\rho_V - \rho_L) \bar{g} = \frac{4}{3}\pi R^3 (\rho_L - \rho_V) g \overline{e_x} \quad (6.17)$$

The second term of Eq. 6.16 is the so-called "contact pressure force" and can be expressed versus the difference of liquid and vapor pressure at the bubble top:

$$\int_{S_w} (P_0 - P_V) \bar{n} \, dS = (P_0 - P_V) \pi r_w^2 \overline{e_y} \quad (6.18)$$

$$= (P_L - P_V - \rho_L g h) \pi r_w^2 \overline{e_y} \quad (6.19)$$

where P_L is the liquid pressure at the bubble top and h the bubble height.

Using Laplace's equation $\Delta P = 2\sigma/R_c$ and assuming that $\rho_L g h \ll \Delta P$ yields:

$$\overline{F_{CP}} \approx \frac{2\sigma}{R_c} \pi r_w^2 \overline{e_y} \approx \pi R \sigma 2 \sin(\theta)^2 \overline{e_y} \quad (6.20)$$

Here, R_c is the curvature radius of the bubble which is often assumed to be equal to $5R$ [66, 89, 120] without other explanation than avoiding an overestimation of the contact pressure force. To avoid this arbitrary choice, following the hypothesis of a nearly spherical bubble shape gives $R_c = R$.

6.2.4 Capillary Force

The capillary force acts at the triple contact line at the bubble's foot and is an important adhesive force maintaining the bubble attached to the wall. Its derivation can be done by integration of the effort exerted over the triple contact line. Noting Φ the polar angle around the bubble foot, we have :

$$\overline{F_C} = 2 \int_0^\pi \sigma r_w \bar{\tau}(\Phi) \, d\Phi \quad (6.21)$$

where $\bar{\tau}$ is the unit vector tangent to the interface and perpendicular to the contact line.

To compute the resulting components parallel and tangent to the wall, Klausner *et al.* [66] account for a contact angle difference between the upstream (receding) contact angle θ_u and downstream (advancing) contact angle θ_d . If the local contact angle is noted γ , then:

$$\bar{\tau}(\Phi) = \cos(\gamma) \cos(\Phi) \bar{e}_x + \sin(\gamma) \bar{e}_y \quad (6.22)$$

Then assuming to represent the evolution of the local contact angle γ from θ_u to θ_d using a polynomial expression of degree 3:

$$\gamma(\Phi) = \theta_d + (\theta_u - \theta_d) \left[3 \left(\frac{\Phi}{\pi} \right)^2 - 2 \left(\frac{\Phi}{\pi} \right)^3 \right], \quad 0 \leq \Phi \leq \pi \quad (6.23)$$

which verifies symmetry conditions:

$$\gamma'(0) = \theta_d, \quad \gamma(\pi) = \theta_u, \quad \gamma'(0) = \gamma'(\pi) = 0 \quad (6.24)$$

To obtain an analytic expression, Klausner *et al.* also consider a first order linear interpolation:

$$\gamma(\Phi) \approx \theta_d + (\theta_u - \theta_d) \frac{\Phi}{\pi} \quad (6.25)$$

This yields:

$$\overline{F_C} = -2r_w \sigma \frac{\pi(\theta_u - \theta_d)}{\pi^2 - (\theta_u - \theta_d)^2} (\sin(\theta_u) + \sin(\theta_d)) \bar{e}_x - 2r_w \sigma \frac{\pi}{\theta_u - \theta_d} (\cos(\theta_d) - \cos(\theta_u)) \bar{e}_y \quad (6.26)$$

By comparing the analytic expression of Eq. 6.26 with the values obtained by numerical integration of Eq. 6.23, Klausner *et al.* introduce a correction factor of 1.25 over the x component, finally giving :

$$\overline{F_C} = -2.5r_w \sigma \frac{\pi(\theta_u - \theta_d)}{\pi^2 - (\theta_u - \theta_d)^2} (\sin(\theta_u) + \sin(\theta_d)) \bar{e}_x - 2r_w \sigma \frac{\pi}{\theta_u - \theta_d} (\cos(\theta_d) - \cos(\theta_u)) \bar{e}_y \quad (6.27)$$

$$= -\pi R \sigma \underbrace{\left[2.5 \frac{r_w}{R} \frac{d\theta}{\left(\frac{\pi}{2}\right)^2 - d\theta^2} \sin(\theta) \cos(d\theta) \right]}_{f_{C,x}} \bar{e}_x - \pi R \sigma \underbrace{\left[2 \frac{r_w}{R} \sin(\theta) \frac{\sin(d\theta)}{d\theta} \right]}_{f_{C,y}} \bar{e}_y \quad (6.28)$$

Remark : We can see that $f_{C,x} \rightarrow 0$ and $f_{C,y} \rightarrow 2 \frac{r_w}{R} \sin(\theta)$ when $d\theta \rightarrow 0$. In that case, $\overline{F_C} = -\overline{F_{CP}}$.

6.2.5 Drag and Lift Forces

The external liquid flow over the bubble induces the well-known drag and lift forces, acting respectively in the flow direction and perpendicular to the flow. They are usually expressed using associated coefficients C_D and C_L defined by:

$$\overline{F_D} = \frac{1}{2} C_D \rho_L S_p \|\overline{U_L} - \overline{U_b}\| (\overline{U_L} - \overline{U_b}) \quad (6.29)$$

$$\overline{F_L} = \frac{1}{2} C_L \rho_L S_p \|\overline{U_L} - \overline{U_b}\|^2 \bar{e}_y \quad (6.30)$$

with $S_p = \pi R^2$ the projected area of the bubble in the direction of the flow.

6.2.5.1 Drag Coefficient

Derivations of analytic expressions for the drag coefficient in an infinite fluid medium exist for more than a century, starting with Hadamard-Ryzbinski (1911) [56]:

$$C_D = \frac{16}{Re_b}, \quad \text{if } Re_b < 1 \quad (6.31)$$

where $\text{Re}_b = \frac{|U_{\text{rel}}|D_B}{\nu_L}$ is the bubble Reynolds number and $U_{\text{rel}} = U_L - U_b$ the relative velocity between the bubble and the surrounding fluid.

For $\text{Re}_b \gg 1$, Levich (1962) [81] found for a potential flow:

$$C_D = \frac{48}{\text{Re}_b} \quad (6.32)$$

For intermediate values of Re_b , traditional approaches rely on expressions of the drag force for a bubble in an infinite medium based on numerical correlations as proposed by Mei & Klausner [92], used in many different mechanistic approaches [15, 107, 120, 126, 141]:

$$C_{D,U} = \frac{16}{\text{Re}_b} \left[1 + \left(\frac{8}{\text{Re}_b} + \frac{1}{2} \left(1 + \frac{3.315}{\sqrt{\text{Re}_b}} \right) \right)^{-1} \right] \quad (6.33)$$

Results from DNS conducted by Legendre *et al.* [78] proposed expressions of the drag and lift forces for a hemispherical bubble on a wall facing a viscous shear flow. Earlier, Legendre & Magnaudet [78] analytically derived coefficients to transpose drag and lift expressions for a particle to the case of a bubble. This was applied by Mazzocco *et al.* [89] to the Drag for a solid particle near a wall in a shear flow proposed by Zeng *et al.* [142].

In this work, we propose to rely on the recent work of Shi *et al.* [116] who conducted DNS of a shear flow over a spherical bubble of constant radius close to a wall for bubble Reynolds number between 10^{-1} and 10^3 and non-dimensional shear rates between -0.5 and 0.5. A sketch of the situation simulated by Shi *et al.* is depicted on Figure 6.6.

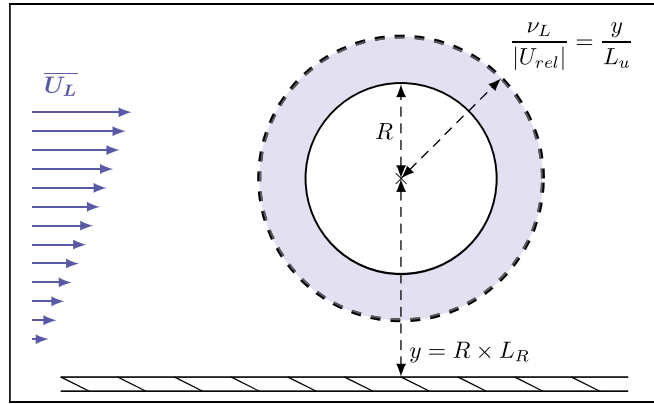


Figure 6.6: Physical situation considered by Shi *et al.* [116].

They computed the resulting drag and lift coefficients for each simulations and proposed correlations fitting their numerical results. The total Drag coefficient is expressed as a correction of the Drag coefficient for a bubble in an unbounded uniform flow $C_{D,U}$. The total drag is given by:

$$C_D = (1 + \Delta C_D) C_{D,U} \quad (6.34)$$

where ΔC_D accounts for both the effect of the shear flow and the wall vicinity.

To cover the whole range of bubble Reynolds numbers, correlations at low and high Re_b are smoothly connected using an exponential term.

$$\Delta C_D = \Delta C_{D,\text{Re}_b=O(1)} + \left(1 - e^{-0.07\text{Re}_b} \right) \Delta C_{D,\text{Re}_b \gg 1} \quad (6.35)$$

Each of those corrections is computed depending on Re_b , the non-dimensional shear rate $\text{Sr} = \frac{2\gamma R}{|U_{\text{rel}}|}$ where $\gamma = \frac{\partial U_{L,x}}{\partial y}$, the non dimensional wall distance $L_R = \frac{y}{R}$ ($L_R = 1$ being a spherical bubble laying on a wall) and non-dimensional viscous (or Stokes) length $L_u = \frac{y}{\nu_L / |U_{\text{rel}}|}$.

$$\Delta C_{D,\text{Re}_b=O(1)} = \frac{1 + \tanh(0.012\text{Re}_b^{0.8}) + \tanh(0.07\text{Re}_b^{0.8})^2}{1 + 0.16L_u(L_u + 4)} \times \left[\left(\frac{3}{8}L_R^{-1} + \frac{3}{64}L_R^{-4} \right) \left(1 - \frac{3}{8}L_R^{-1} - \frac{3}{64}L_R^{-4} \right)^{-1} - \frac{1}{16} \left(L_R^{-2} + \frac{3}{8}L_R^{-3} \right) \text{Sr} \right] \quad (6.36)$$

$$\Delta C_{D,\text{Re}_b \gg 1} = 0.47L_R^{-4} + 0.0055L_R^{-6}\text{Re}_b^{3/4} + 0.002|\text{Sr}|^{1.9}\text{Re}_b + 0.05L_R^{-7/2}\text{Sr}\text{Re}_b^{1/3} \quad (6.37)$$

Figure 6.7 shows the evolution of the drag correction ΔC_D against the bubble Reynolds number for different dimensionless distances to the wall L_R and two values of Sr. We can see that as the distance between the wall and the bubble increases the drag correction logically approaches zero and that increasing the shear rate Sr increases ΔC_D for higher values of Re_b .

Shi *et al.* [116] conducted DNS for wall distances down to $L_R = 1.5$. However, Scheiff *et al.* [113] compared the values obtained for $L_R = 1$ with measured drag coefficients of bubbles sliding on a wall and observed a good agreement, which legitimates the use of this new drag correlation by extending its application to the case of a bubble laying on a wall and using the uniform drag coefficient of Eq. 6.33.

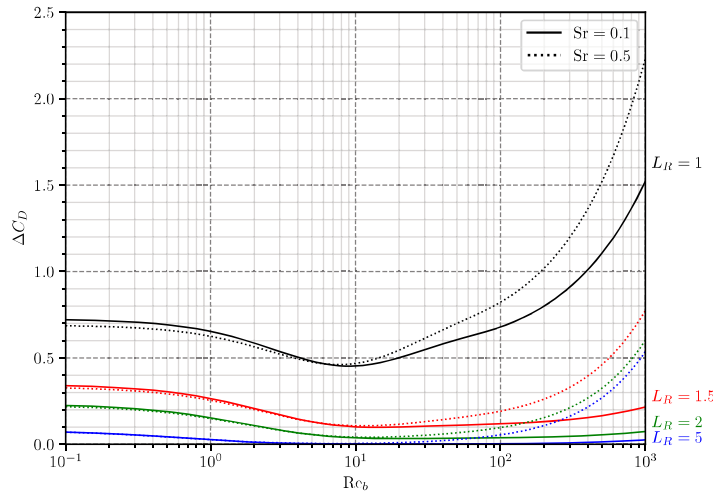


Figure 6.7: Drag correction from Shi *et al.* [116].

Remark : In PWR conditions, a static bubble of radius 0.01 mm on a wall with a bulk liquid velocity of 5 m/s leads to a non-dimensional shear rate $\text{Sr} \approx 0.7$ with $\text{Re}_b \approx 500$. In this case, the drag correction can reach 180% compared to the unbounded uniform flow formulation.

This also yields a bubble Weber number $\text{We} \approx 0.08$ and a Capillary number $\text{Ca} \approx 0.0036$ which further supports the assumption of spherical bubble shape.

6.2.5.2 Lift Coefficient

In 1987, Auton *et al.* [2] analytically derived the lift force for an inviscid fluid in unstationary motion in a weak velocity gradient and found $C_L = 0.5$, with the lift force defined as:

$$\overline{F_L} = -\rho_L C_L V_b (\overline{U_L} - \overline{U_b}) \wedge \overline{\omega} \quad (6.38)$$

where $\overline{\omega}$ is the flow vorticity.

This result was enriched by Legendre & Magnaudet (1998) [78] who used numerical results to propose a dependency of C_L on the bubble Reynolds number for a sphere in an infinite medium facing a weakly sheared flows as:

$$C_L = (C_{L,\text{Re}_b \sim 1}^2 + C_{L,\text{Re}_b \gg 1}^2)^{1/2} \quad (6.39)$$

$$= \left(\left[\frac{6}{\pi^2} \frac{2.255 (\text{Re}_b \omega^*)^{-1/2}}{\left(1 + 0.2 \frac{\text{Re}_b}{\omega^*} \right)^{3/2}} \right]^2 + \left[\frac{1}{2} \frac{1 + 16 \text{Re}_b^{-1}}{1 + 29 \text{Re}_b^{-1}} \right]^2 \right)^{1/2} \quad (6.40)$$

where $\omega^* = \frac{2R |\bar{\omega}|}{|U_{rel}|}$ is the non-dimensional vorticity of the flow, equal to Sr here for the linear shear flow case.

Later, Mei & Klausner (1994) [91] derived the lift force induced by the shear for a spherical bubble in an unbounded flow for low Reynolds numbers, based on the expression of Saffmann [112]. By interpolating this result with the solution of Auton [2], they obtained a formulation for a large range of Re_b :

$$C_L = 2.74 \sqrt{\text{Sr}} \times \left[\text{Re}_b^{-2} + (0.24 \sqrt{\text{Sr}})^4 \right]^{1/4} \quad (6.41)$$

This expression is actually used in many mechanistic force balance [15, 66, 107, 120].

In his force-balance approach, Mazzocco *et al.* [89] used a constant lift coefficient by using the upper bound for the lift of a solid particle touching a wall in a Stokes flow, multiplied by $\frac{4}{9}$ to transpose this value to the bubble case as suggested by Legendre & Magnaudet [78]. This resulted in:

$$C_L = 2.61 \quad (6.42)$$

In accordance with the computation of the drag coefficient, our model will rely on the expression of the lift coefficient proposed by Shi *et al.* [116]. Their formulation includes extra parameters compared to the drag coefficient :

- The non-dimensional Saffman length $L_\omega = \frac{y}{\sqrt{\nu_L/\omega}}$;
- The Stokes (or Oseen) length to Saffman length ratio $\varepsilon = \frac{\nu_L / |U_{rel}|}{\sqrt{\nu_L/\omega}}$, which quantifies the origin of inertial effects being either shear ($\varepsilon > 1$) or the relative slip of the bubble ($\varepsilon < 1$).

The resulting formulation of C_L corresponds to the superpositions of two contributions respectively associated to the uniform flow and the shear rate, both coupled with the wall presence.

$$C_L^W = C_{Lu}^W + C_{L\omega}^W \quad (6.43)$$

The lift associated to the uniform flow near a wall is computed as follows:

$$\begin{aligned} C_{Lu}^W &= e^{-0.22 \varepsilon^{0.8} L_\omega^{2.5}} \frac{[1 + \tanh(0.012 \text{Re}_b^{0.8}) + \tanh(0.07 \text{Re}_b^{0.8})]^2}{1 + 0.13 L_u (L_u + 0.53)} \\ &\times \left(\frac{L_R}{3} \right)^{-2.0 \tanh(0.01 \text{Re}_b)} C_{Lu}^{\text{W-in}} \\ &+ \left(1 - e^{-0.22 \text{Re}_b^{0.6}} \right) \left[C_{Lu, \text{Re}_b \rightarrow \infty}^W + 15 \tanh(0.01 \text{Re}_b) \text{Re}_b^{-1} L_R^{-4} \right] \end{aligned} \quad (6.44)$$

Where:

$$C_{Lu}^{\text{W-in}} = \frac{1}{2} \left(1 + \frac{1}{8} L_R^{-1} - \frac{33}{64} L_R^{-2} \right) \quad (6.45)$$

$$C_{Lu, \text{Re}_b \rightarrow \infty}^W = -\frac{3}{8} L_R^{-4} \left[1 + \frac{1}{8} L_R^{-3} + \frac{1}{6} L_R^{-5} \right] + O(L_R^{-10}) \quad (6.46)$$

The lift associated to the vorticity near a wall is computed as follows:

$$C_{L\omega}^W = \left[1 - \exp \left(-\frac{11}{96} \pi^2 \frac{L_\omega}{J_L(\varepsilon)} \left(1 + \frac{9}{8} L_R^{-1} - \frac{1271}{3520} L_R^{-2} \right) \right) \right] C_{L\omega, \text{Re}_b \ll 1}^U \quad (6.47)$$

$$+ \left(1 - e^{-0.3 \text{ Re}_b} \right) \left[1 + 0.23 L_R^{-7/2} \left(1 + 13 \text{ Re}_b^{-1/2} \right) \right] C_{L\omega, \text{Re}_b \gg 1}^U \quad (6.48)$$

Where:

$$J_L(\varepsilon) = 2.254 (1 + 0.2\varepsilon^{-2})^{-3/2} \quad (6.49)$$

$$C_{L\omega, \text{Re}_b \ll 1}^U = \frac{8}{\pi^2} \frac{\text{Sr}}{|\text{Sr}|} \varepsilon J_L(\varepsilon) \quad (6.50)$$

$$C_{L\omega, \text{Re}_b \gg 1}^U = \frac{2}{3} \text{Sr} (1 - 0.07 |\text{Sr}|) \frac{1 + 16 \text{Re}_b^{-1}}{1 + 29 \text{Re}_b^{-1}} \quad (6.51)$$

On Figure 6.8, we plot the values of C_L obtained by the formulation of Shi *et al.* different values of the non-dimensional wall distance L_R (extending down to $L_R = 1$) and non-dimensional shear rate Sr.

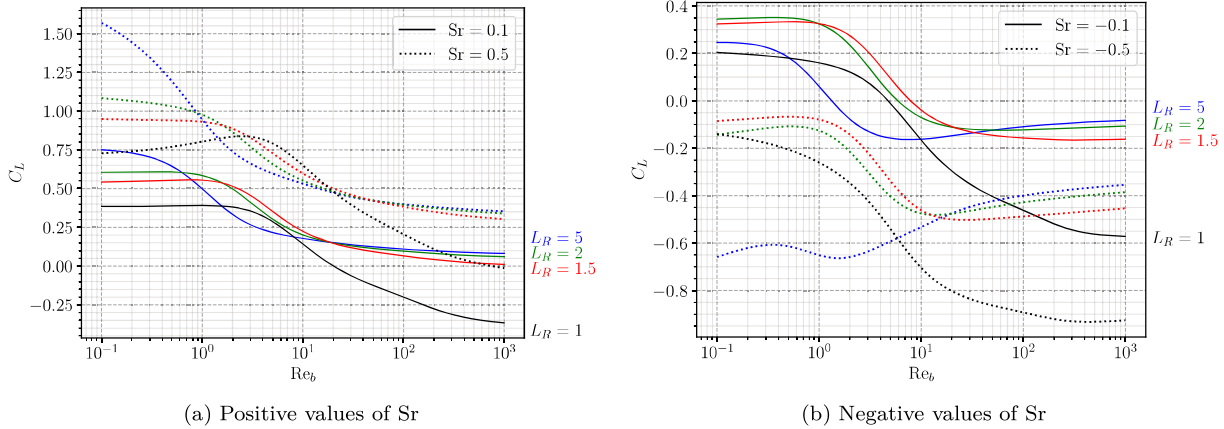


Figure 6.8: C_L computed using Shi *et al.* correlation.

We can see that the magnitude of the lift coefficient globally increases with the wall distance when $\text{Sr} > 0$ and that negative lift values are easily reached when $\text{Sr} < 0$. This means that correlations for unbounded medium may overestimate the lift experienced by the bubble compared to the situation with a wall.

The extension to the case $L_R = 1$ may be more questionable compared to the drag since the bubble touching the wall will stop any flow in between, leading to inertial and shear regimes that would be significantly different due to the redirection of the liquid at the bubble's foot towards the bulk. In particular, we can see that the values reached for $L_R = 1$ on Figure 6.8 are not following the general trend of simulated L_R :

- Negative values of C_L are reached with positive Sr at high Re_b while getting close to the wall seemed to tend to a value of $C_L \geq 0$ at high Re_b ;
- Magnitude of C_L with negative Sr are not coherent with the observed trend down to $L_R = 1.5$.

This observation suggest that we should include the effect of the wall using the lift of Shi *et al.* by limiting its use to $L_R = 1.5$ contrary to the drag which extension to $L_R = 1.0$ was coherent and validated.

Remark : In PWR conditions, taking $\text{Sr} \approx 0.7$ with $\text{Re}_b \approx 500$ for the static bubble on a wall leads to $C_L \approx 0.45$ both with Mei & Klausner (Eq. 6.41) and Shi *et al.* (Eq. 6.43). For a bubble that would slide at 90% of the local liquid velocity, this gives $\text{Sr} \approx 7$ and $\text{Re}_b \approx 50$ yielding $C_{L, \text{Mei}} \approx 4$ and $C_{L, \text{Shi}} \approx 2.8$.

6.2.6 Inertia Force

The Inertia force originates from various effects (bubble growth, freestream and bubble acceleration, etc.) and includes both added mass and Tchen forces and is expressed as presented in Magnaudet & Eames (2000) [85]:

$$\overline{F}_I = \rho_L V_b \left(\underbrace{\frac{\partial \overline{U}_L}{\partial t} + \overline{\nabla}(\overline{U}_L) \cdot \overline{U}_L}_{\text{Liquid inertia or Tchen force}} \right) + \underbrace{\frac{d}{dt} (\rho_L C_{AM} V_b (\overline{U}_L - \overline{U}_b))}_{\text{Added Mass force } \overline{F}_{AM}} \quad (6.52)$$

Since we consider a steady and quasi-parallel liquid flow, we respectively have:

$$\frac{\partial \overline{U}_L}{\partial t} = 0 \text{ and } \overline{\nabla}(\overline{U}_L) \cdot \overline{U}_L = 0 \quad (6.53)$$

Thus only remains the added mass force to be expressed in the considered force balance. In the next subsections, we detail former approaches to tackle the added mass derivation and propose a more rigorous one to re-evaluate the added mass coefficients.

6.2.6.1 Former Approaches

In previous mechanistic models, the derivation of the added mass force was conducted with different approaches. In particular, some authors chose to rely on the Rayleigh-Plesset Equation (RPE) for a growing hemispherical bubble in a quiescent flow to obtain the reaction force from the liquid, oriented perpendicularly to the wall:

$$\overline{F}_{AM,RPE} = -\rho_L \pi R^2 \left[R \ddot{R} + \frac{3}{2} \dot{R}^2 \right] \overline{e}_y \quad (6.54)$$

Then, assuming a bubble inclination angle θ_i , this force was projected along the x axis to obtain an Added Mass force parallel to the wall that hinders departure. The inclination angle value is often empirical and used for data fitting [22, 89, 107, 141].

$$\overline{F}_{AM,RPE} = -\rho_L \pi R^2 \left[R \ddot{R} + \frac{3}{2} \dot{R}^2 \right] (\sin(\theta_i) \overline{e}_x + \cos(\theta_i) \overline{e}_y) \quad (6.55)$$

This approach is questionable on different aspects. First, the RPE assumes a moving boundary in a quiescent unbounded liquid, which is physically far from the real situation of a bubble growing on a wall in a boiling flow. Moreover, the subsequent projection along the different directions regarding an unknown angle is hardly reasonable if θ_i is chosen arbitrarily. Values of θ_i selected by different authors are mentioned in Table 6.2.

On the other hand, some authors [50, 66, 126] considered two distinct contributions:

- Hemispherical bubble growth in a stagnant liquid, leading to Eq. 6.55 including the inclination angle θ_i ;
- Spherical bubble growth in a uniform unbounded and inviscid liquid flow, which yields a detaching Added Mass term due to the interaction of bubble growth with the external flow:

$$\overline{F}_{AM,U} = \frac{3}{2} \rho_L V_b \frac{\dot{R}}{R} U_L \overline{e}_x \quad (6.56)$$

This last term is usually called a "bulk growth force". By including the effect of the liquid flow, this approach can be considered as closer to the reality. However, it relies on two separate derivations associated to different physical considerations.

6.2.6.2 Proposed Approach

To tackle the added mass derivation in a proper way, we propose to follow the approach of Lamb [74] (also presented by Milne Thomson [94] or Van Winjgaarden [133]). By solving the potential flow around a bubble and its image, we can obtain the total liquid kinetic energy E_L that corresponds to a situation where a bubble is at a given distance from a wall (represented by the line normal to the line of centers of the bubbles).

Then we can use Lagrange equation to compute the resulting forces along a given coordinate q :

$$F_{AM,q} = -\frac{\partial}{\partial t} \left(\frac{\partial E_L}{\partial \dot{q}} \right) + \frac{\partial E_L}{\partial q} \quad (6.57)$$

This method was also used by Duhar [32] who developed an asymptotic expression of E_L to compute the added mass coefficient when a growing bubble approaches the wall. Here, we express the liquid kinetic energy by relying on the work of Van Der Geld [43] who derived E_L in the case of a full or truncated spherical bubble laying on a wall and facing an uniform flow parallel to the wall of velocity U_L (Eq. 6.58). If the bubble slides at a velocity $U_b = \dot{x}$, it sees a liquid velocity $U_{rel} = U_L - \dot{x}$.

$$E_L = \frac{\rho_L V_b}{2} \left(\alpha \dot{y}^2 + \text{tr}(\beta) \dot{R}^2 + \psi \dot{R} \dot{y} + \alpha_2 (U_L - \dot{x})^2 \right) \quad (6.58)$$

where (x, y) are the coordinates of the bubble's center and α , $\text{tr}(\beta)$, ψ , α_2 are polynomials of $R/y = 1/L_R$ derived by Van Der Geld for $1 < R/y < 2$ i.e. $0.5 < L_R < 1$, corresponding to contact angles $0^\circ < \theta < 60^\circ$.

For each polynomial expression (α is used as an example), we note n its degree and write:

$$\alpha = \sum_{k=0}^n \alpha_k \left(\frac{R}{y} \right)^k \quad \text{and} \quad \tilde{\alpha} = \sum_{k=0}^n k \alpha_k \left(\frac{R}{y} \right)^k \quad (6.59)$$

This allows to express the following derivatives:

$$\frac{\partial \alpha}{\partial y} = -\frac{1}{y} \tilde{\alpha} \quad \text{and} \quad \frac{\partial \alpha}{\partial t} = \left(\frac{\dot{R}}{R} - \frac{\dot{y}}{y} \right) \tilde{\alpha} \quad (6.60)$$

Noticing that the derivatives of the polynomials along x will be 0 and injecting E_L in Eq. 6.57 allows to express the added mass force in x and y directions. If we express it using geometrical ratios $\frac{R}{y} = \frac{1}{F_1}$, $\frac{\dot{y}}{\dot{R}} = F_2$ and $\frac{\ddot{y}}{\dot{R}} = F_3$, we can obtain:

$$F_{AM,x} = \rho_L V_b \left[\left(3\alpha_2 + \left(1 - \frac{F_2}{F_1} \right) \tilde{\alpha}_2 \right) \frac{\dot{R}}{R} U_{rel} - \alpha_2 \frac{\partial U_b}{\partial t} \right] \quad (6.61)$$

$$\begin{aligned} F_{AM,y} = -\rho_L V_b & \left[\left(3F_2\alpha + \frac{3}{2}\psi + \left(1 - \frac{F_2}{F_1} \right) F_2 \tilde{\alpha} + \left(1 - \frac{F_2}{F_1} \right) \frac{\tilde{\psi}}{2} + \frac{F_2}{F_1} \frac{\tilde{\alpha}}{2} + \frac{1}{F_1} \frac{\text{tr}(\tilde{\beta})}{2} + \frac{F_2}{F_1} \frac{\tilde{\psi}}{2} \right) \frac{\dot{R}^2}{R} \right. \\ & \left. + \left(F_3\alpha + \frac{\psi}{2} \right) \ddot{R} + \frac{1}{F_1} \frac{\alpha_2}{2} \frac{U_{rel}^2}{R} \right] \end{aligned} \quad (6.62)$$

In the case of a truncated sphere, $F_1 = \frac{y}{R} = \cos(\theta) = L_R$. If we suppose that the bubble keeps a nearly constant contact angle during its lifetime, we can further write $F_1 = F_2 = F_3 = \cos(\theta) = L_R$, which simplifies the forces in:

$$F_{AM,x} = \rho_L V_b \left[3\alpha_2 \frac{\dot{R}}{R} U_{rel} - \underbrace{\alpha_2}_{C_{AM,x}} \frac{\partial U_b}{\partial t} \right] \quad (6.63)$$

$$F_{AM,y} = \rho_L V_b \left[- \left(\underbrace{3 \left(L_R \alpha + \frac{\psi}{2} \right)}_{C_{AM,y1}} + \underbrace{\tilde{\alpha}}_{C_{AM,y2}} + \underbrace{\frac{1}{L_R} \frac{\text{tr}(\tilde{\beta})}{2} + \frac{\tilde{\psi}}{2}}_{C_{AM,y2}} \right) \frac{\dot{R}^2}{R} \right. \quad (6.64)$$

$$\left. - \left(L_R \alpha + \frac{\psi}{2} \right) \ddot{R} + \underbrace{\frac{-1}{L_R} \frac{\tilde{\alpha}_2}{2} \frac{U_{rel}^2}{R}}_{C_{AM,y3}} \right] \quad (6.65)$$

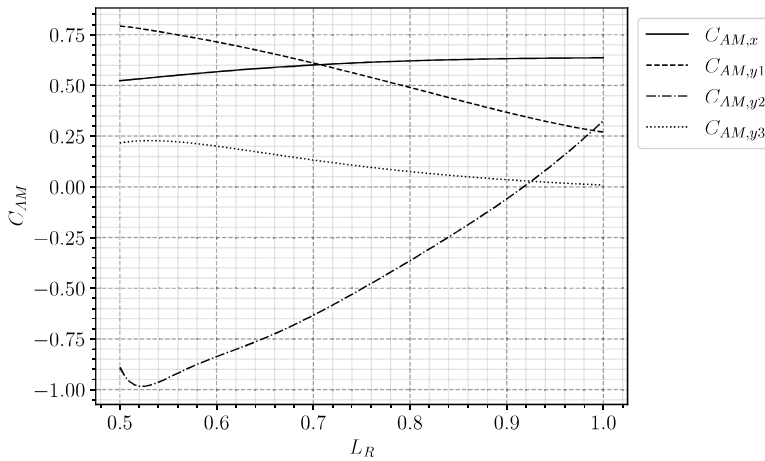


Figure 6.9: Values of the computed added mass coefficients in Eq. 6.63 and 6.65.

On Figure 6.9, we plot the values of the added mass coefficients against the values of L_R . For the case of a spherical bubble laying on a wall ($L_R = 1$), we finally have:

$$F_{AM,x} = \rho_L V_b \left[3C_{AM,x} \frac{\dot{R}}{R} U_{rel} - C_{AM,x} \frac{\partial U_b}{\partial t} \right] \quad (6.66)$$

with $C_{AM,x} \approx 0.636$.

$$F_{AM,y} = \rho_L V_b \left[-(3C_{AM,y1} + C_{AM,y2}) \frac{\dot{R}^2}{R} - C_{AM,y1} \ddot{R} + C_{AM,y3} \frac{U_{rel}^2}{R} \right] \quad (6.67)$$

with $C_{AM,y1} \approx 0.27$, $C_{AM,y2} \approx 0.326$ and $C_{AM,y3} \approx 8.77 \times 10^{-3}$.

Parallel to the wall, the coupled term $\frac{\dot{R}}{R} U_{rel}$ in Eq. 6.66 promotes detachment and sliding of the bubble if $U_{rel} > 0$ e. g. if the bubble is attached to its nucleation site. This contradicts the aforementioned approach where solely projecting the RPE on both axes lead to an Added-Mass term related to bubble growth that only hinders the departure by sliding. Moreover, Eq. 6.67 exhibits a term induced by the relative velocity that acts as a lift force, which seems to rarely appear in other approaches.

Remark : The derived values of the added mass coefficients are only valid for $0.5 < L_R < 1$ as previously mentioned. When the bubble leaves the wall, added mass calculations of Duhar [31] would be more appropriate.

Those theoretical results highlight the importance of conducting a rigorous approach when possible to deriving those transient aspects of the force balance. Otherwise, some terms may be missing and lead to contradictory physical conclusions.

In the spirit of avoiding to introduce extra empirical terms, we keep the Added Mass force as presented in Eq. 6.66 and 6.67 and consider no projection along the inclination angle.

6.2.7 Force Balance Summary

Writing Newton's second law, we have the total force balance over the bubble in both directions:

$$\begin{aligned} \rho_V \frac{\partial V_b U_{b,x}}{\partial t} = & -\pi R \sigma f_{C,x}(\theta, d\theta) + V_b (\rho_L - \rho_V) g + \frac{1}{2} C_D \rho_L \pi R^2 |U_L - U_b| (U_L - U_b) \\ & + \rho_L V_b \left[3C_{AM,x} \frac{\dot{R}}{R} (U_L - U_b) - C_{AM,x} \frac{\partial U_b}{\partial t} \right] \end{aligned} \quad (6.68)$$

$$\rho_V \frac{\partial V_b U_{b,y}}{\partial t} = -\pi R \sigma f_{C,y}(\theta, d\theta) + 2\pi R \sigma \sin(\theta)^2 + \frac{1}{2} C_L \rho_L \pi R^2 (U_L - U_b)^2 + \rho_L V_b \left[-(3C_{AM,y1} + C_{AM,y2}) \frac{\dot{R}^2}{R} - C_{AM,y1} \dot{R} + C_{AM,y3} \frac{(U_L - U_b)^2}{R} \right] \quad (6.69)$$

Those force balances will respectively be used later to study the departure by sliding (along x) and the lift-off from the wall (along y).

On Table 6.2, we sum up some of the mentioned mechanistic approaches and their models along with the proposed force balance.

	Klausner (1993) [66]	Thorncroft (2001) [126]	Sugrue (2016) [120]
Forces	$\overline{F}_B = \frac{4}{3}\pi R^3 (\rho_L - \rho_V) \bar{g}$	$\overline{F}_B = \frac{4}{3}\pi R^3 (\rho_L - \rho_V) \bar{g}$	$\overline{F}_B = \frac{4}{3}\pi R^3 (\rho_L - \rho_V) \bar{g}$
	$\overline{F}_C = \text{Eq. 6.28, } r_w = 0.045 \text{ mm}$	$\overline{F}_C = \text{Eq. 6.28, } r_w = R \sin(\theta_d)$	$\overline{F}_C = \text{Eq. 6.28, } r_w = 0.025R$
	$\overline{F}_{CP} = \text{Eq. 6.20, } R_c = 5R$	Neglected	$\overline{F}_{CP} = \text{Eq. 6.20, } R_c = 5R$
	$\overline{F}_D = C_D = \frac{16}{Re_b} \left[1 + \frac{3}{2} \left(\left(\frac{12}{Re_b} \right)^n + 0.796^n \right)^{1/n} \right], n = 0.65$	$C_D = \frac{16}{Re_b} \left[1 + \left(\frac{8}{Re_b} + \frac{1}{2} \left(1 + \frac{3.315}{\sqrt{Re_b}} \right) \right)^{-1} \right]$	$C_D = \frac{16}{Re_b} \left[1 + \frac{3}{2} \left(\left(\frac{12}{Re_b} \right)^n + 0.796^n \right)^{1/n} \right], n = 0.65$
	$\overline{F}_L = C_L = 2.74\sqrt{Sr} \times \left[Re_b^{-2} + (0.24\sqrt{Sr})^4 \right]^{\frac{1}{4}}$	$C_L = 0.71\sqrt{Sr} \times \left[\left(\frac{1.15J(\varepsilon)}{\sqrt{Re_b}} \right)^2 + \left(\frac{3\sqrt{2Sr}}{8} \right)^2 \right]^{\frac{1}{2}}$	$C_L = 2.74\sqrt{Sr} \times \left[Re_b^{-2} + (0.24\sqrt{Sr})^4 \right]^{\frac{1}{4}}$
	$\overline{F}_{AM} = \frac{3}{2}\rho_L V_b \frac{\dot{R}}{R} U_L \bar{e}_x - \rho_L \pi R^2 \left(\frac{3}{2}\dot{R}^2 + R\ddot{R} \right) \times (\cos(\theta_i) \bar{e}_y + \sin(\theta_i) \bar{e}_x), \theta_i = 10^\circ$	$\overline{F}_{AM} = 2\pi\rho_L R^2 \dot{R} U_L \bar{e}_x - \rho_L \pi R^2 \left(\frac{3}{2}\dot{R}^2 + R\ddot{R} \right) \times (\cos(\theta_i) \bar{e}_y + \sin(\theta_i) \bar{e}_x), \theta_i = 45^\circ$	$\overline{F}_{AM} = -\rho_L \pi R^2 \left(\frac{3}{2}\dot{R}^2 + R\ddot{R} \right) \times (\cos(\theta_i) \bar{e}_y + \sin(\theta_i) \bar{e}_x), \theta_i = 10^\circ$
	Mazzocco (2018) [89]	Ren (2020) [107]	Present model
Forces	$\overline{F}_B = \frac{4}{3}\pi R^3 (\rho_L - \rho_V) \bar{g}$	$\overline{F}_B = \frac{4}{3}\pi R^3 (\rho_L - \rho_V) \bar{g}$	$\overline{F}_B = \frac{4}{3}\pi R^3 (\rho_L - \rho_V) \bar{g}$
	$\overline{F}_C = \text{Eq. 6.28, } r_w = R/15$	$\overline{F}_C = \text{Eq. 6.28, } r_w = 0.2R$	$\overline{F}_C = \text{Eq. 6.28, } r_w = R \sin(\theta)$
	$\overline{F}_{CP} = \text{Eq. 6.20, } R_c = 5R$	$\overline{F}_{CP} = \text{Eq. 6.20, } R_c = 5R$	$\overline{F}_{CP} = \text{Eq. 6.20, } R_c = R$
	$\overline{F}_D = C_D = 1.13 \frac{24}{Re_b} \left(1 + 0.104 Re_b^{0.753} \right)$	$C_D = \frac{16}{Re_b} \left[1 + \frac{3}{2} \left(\left(\frac{12}{Re_b} \right)^n + 0.796^n \right)^{1/n} \right], n = 0.65$	$C_D = C_{D,U} (1 + \Delta C_D)$ $C_{D,U}$ by Eq. 6.33, ΔC_D by Eq. 6.35
	$\overline{F}_L = C_L = 2.61$	$C_L = 2.74\sqrt{Sr} \times \left[Re_b^{-2} + (0.24\sqrt{Sr})^4 \right]^{\frac{1}{4}}$	C_L by Shi <i>et al.</i> [116]
	$\overline{F}_{AM} = -\frac{1}{4}\pi\rho_L K^4 (\cos(\theta_i) \bar{e}_y + \sin(\theta_i) \bar{e}_x), \sin(\theta_i) = 0.2, \cos(\theta_i) = 1$	$\overline{F}_{AM} = -\rho_L \pi R^2 \left(\frac{3}{2}\dot{R}^2 + R\ddot{R} \right) \times (\cos(\theta_i) \bar{e}_y + \sin(\theta_i) \bar{e}_x), \theta_i = 15^\circ$	$\frac{F_{AM,x}}{\rho_L V_b} = C_{AM,x} \left[3 \frac{\dot{R}}{R} U_{rel} - \frac{\partial U_b}{\partial t} \right], C_{AM,x} = 0.636, F_{AM,y}$ by Eq. 6.67.

Table 6.2: Summary of different force-balance mechanistic approaches.

6.2.8 Liquid Velocity

To compute the liquid velocity and shear rate at bubble center height, we use the wall law of Reichardt [106], which describes the velocity profile from the viscous sublayer to the logarithmic region in a single-phase flow.

$$\begin{aligned} U_L^+ &= \frac{1}{\kappa} \ln(1 + \kappa y^+) + c \left(1 - e^{-y^+/\chi} + \frac{y^+}{\chi} e^{-y^+/3} \right) \\ U_L &= U_L^+ U_\tau \end{aligned} \quad (6.70)$$

with $\kappa = 0.41$, $\chi = 11$ and $c = 7.8$.

$$\begin{aligned} \frac{\partial U_L^+}{\partial y^+} &= \frac{1}{1 + \kappa y^+} + \frac{c}{\chi} \left(e^{-y^+/\chi} + \left(1 - \frac{y^+}{3} \right) e^{-y^+/3} \right) \\ \frac{\partial U_L}{\partial y} &= \gamma = \frac{U_\tau^2}{\nu_L} \frac{\partial U_L^+}{\partial y^+} \end{aligned} \quad (6.71)$$

The friction velocity is computed using Mac Adams correlation [90].

$$U_\tau = \sqrt{\frac{\tau_w}{\nu_L}} \quad (6.72)$$

$$\tau_w = 0.018 \text{ Re}_{D_h}^{-0.182} \frac{G_L^2}{\rho_L} \quad (6.73)$$

6.3 BUBBLE GROWTH

6.3.1 Introduction

In order to properly represent the bubble dynamics, it is mandatory to model the evolution of the bubble radius over time *i.e.* the bubble growth law. Since the bubble radius R and its derivatives \dot{R} and \ddot{R} appear in the force balance (notably in the expression of the added mass force 6.65), failing to predict the evolution of the bubble with time will definitely result in a force unbalance.

The problem of the bubble growth during its lifetime on the wall, including the sliding phase, is still an open question that aims to cover various types of heat transfer mechanisms. First, two growth regimes exist for a boiling bubble:

- Inertial growth, which occurs at the beginning of nucleation for low temperature difference between liquid and vapor. The evolution of the bubble size can be solved by the mass and momentum balances, through the solution of Rayleigh (1917) [105]. The form of the bubble growth is usually $R(t) = A \times t$ (Mikic & Rohsenow, [93]).
- Heat diffusion growth happening post the inertial phase. This type of bubble growth has been widely studied by different authors [93, 101, 115, 147] and is usually of the form $R(t) = B\sqrt{t}$, derivable using the energy balance around the bubble.

Those two regimes can be compared using the non-dimensional time t^+ defined as:

$$t^+ = \frac{A^2}{B^2} t \quad (6.74)$$

where

$$A = \sqrt{b \frac{h_{LV} \rho_V \Delta T_w}{\rho_L T_{sat}}} \text{ and } B = \sqrt{\frac{12}{\pi} \eta_L \text{Ja}} \quad (6.75)$$

with $b = \frac{2}{3}$ for a bubble in an infinite liquid medium and $b = \frac{\pi}{7}$ for a spherical bubble laying on a wall.

So that when $t^+ \ll 1$, $R(t) = At$ (inertial growth) and when $t^+ \gg 1$, $R(t) = B\sqrt{t}$ (heat diffusion growth). A general solution asymptotically covering the two regimes has been derived by Mikic & Rohsenow:

$$R^+ = \frac{2}{3} \left[(t^+ + 1)^{3/2} + t^{+3/2} - 1 \right], \quad R^+ = \frac{R}{B^2/A}, \quad t^+ = \frac{t}{B^2/A^2} \quad (6.76)$$

In most cases associated to wall nucleation and boiling flows, experimental observations showed that bubbles' lifetime is long enough to be mostly of heat conduction nature [72, 86, 145].

Remark : Estimating the time t at which the diffusive growth radius equals the inertia growth radius yields:

- $t \approx 0.39 \mu s$ for water at 1 bar and $\Delta T_w = 15 \text{ K}$
- $t \approx 1.6 \times 10^{-4} \mu s$ for water at 150 bar and $\Delta T_w = 5 \text{ K}$

which insists on the validity of the nearly pure diffusive growth hypothesis.

6.3.2 Heat Diffusion in Uniformly Superheated Liquid

The analytic derivation of a bubble growth law in a pure heat diffusion regime has been tackled by various authors, mostly for the case of a bubble in a uniformly superheated and quiescent liquid. An reference solution is the work of Plesset & Zwick (1954) [101] who found an asymptotic solution for high values of Ja:

$$R(t) = \frac{2\sqrt{3}}{\sqrt{\pi}} \text{Ja} \sqrt{\eta_L t} \quad (6.77)$$

This result was generalized by Scriven (1959) [115] who derived whatever the value of Ja:

$$R(t) = 2\mathcal{F}(\text{Ja}) \text{Ja} \sqrt{\eta_L t} \quad (6.78)$$

where \mathcal{F} is implicitly defined by assuming $\frac{\rho_L}{\rho_V} \gg 1$:

$$\mathcal{F}(\text{Ja}) = \frac{F}{2\text{Ja}^2}, \text{ and } \text{Ja} = F \exp\left(\frac{3}{2}F\right) \int_1^\infty \frac{1}{x^2} \exp\left(-\frac{F}{x} - \frac{F}{2}x^2\right) dx \quad (6.79)$$

which falls back to $\mathcal{F}(\text{Ja}) \rightarrow \frac{\sqrt{3}}{\sqrt{\pi}}$ when $\text{Ja} \gg 1$.

The general formulation of \mathcal{F} has been verified by Legendre *et al.* [77] with Direct Numerical Simulation of spherical bubble growth in a quiescent superheated liquid.

Usually, most authors are accepting $R(t) = K \text{Ja}_w \sqrt{\eta_L t}$ for the bubble growth. With K usually expressed as $K = \frac{2b}{\sqrt{\pi}}$ with b being used as an adjustable constant depending on the flow conditions, the fluid and the heater properties, or derived analytically as presented before ($b = \sqrt{3}$ [101], $b = \frac{\pi}{2}$ [38], $1 \leq b \leq \sqrt{3}$ [147], $b = 1.56$ [140], $b = 0.24$ [139], etc.).

When the bubble presents a relative velocity with the ambient liquid, the disturbance of the thermal boundary layer around the liquid-vapor interface will impact its growth. This phenomenon has been numerically studied by Legendre *et al.* [77] who found that the ratio between the growth rate \dot{R} and the relative velocity U_{rel} was controlling the growth regime as follows:

- If $\frac{\dot{R}}{U_{rel}} \gg 1$, the regime is close to the static heat diffusion and correspond to the Scriven formulation (Eq. 6.78) ;
- If $\frac{\dot{R}}{U_{rel}} \ll 1$, the relative velocity impacts the thermal boundary layer formation and leads to a growth matching the solution of Ruckenstein (1964) [110] where the Nusselt number at the liquid-vapor interface is:

$$\text{Nu} = 2\sqrt{\frac{\text{Pe}(t)}{\pi}}, \text{ Pe}(t) = \text{Pr}_L \times \text{Re}_b(t) \quad (6.80)$$

In this case, the bubble growth is accelerated and $R \propto t^{2/3}$.

6.3.3 Microlayer Evaporation

In addition to the traditional heat diffusion from superheated liquid to the bubble through the liquid-vapor interface, bubble growth can also be enhanced by the evaporation of a so-called "microlayer". This term denotes a very thin layer of liquid (typically $\sim \mu\text{m}$ [72]) which is trapped between the heated wall and the bubble base, as shown on Figure 6.10. The existence of this microlayer has now been supported by both experimental visualizations [17, 18, 70, 72] and numerical investigations [12, 53, 131].

Parallel to the heat diffusion approach, some authors computed the bubble growth by considering a pure microlayer evaporation regime. A well-known model of this type has been derived by Cooper & Lloyd in 1969 [23] and considers the wall thermal properties so that:

$$R(t) = 2.5 \frac{\text{Ja}}{\sqrt{\text{Pr}_L}} \sqrt{\eta_L t} \text{ if } \lambda_w \gg \lambda_L \quad (6.81)$$

$$R(t) = \frac{2}{\sqrt{\pi}} \sqrt{\frac{\lambda_w \rho_w c_{p,w}}{\lambda_L \rho_L c_{p,L}}} \text{ if } \lambda_w \ll \lambda_L \quad (6.82)$$

Remark : The parameter $\sqrt{\frac{\lambda_w \rho_w c_{p,w}}{\lambda_L \rho_L c_{p,L}}}$ that accounts for the wall properties is the same used in the correlation of Ünal for the maximum bubble diameter (Eq. 6.5).

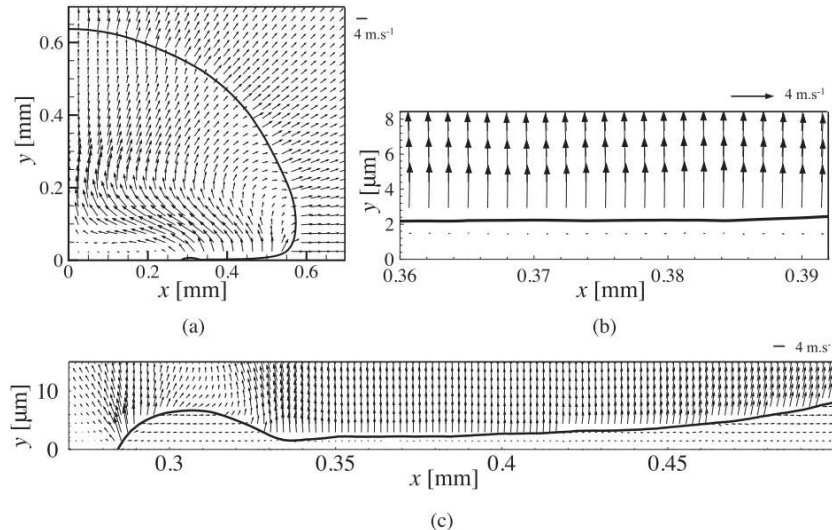


Figure 6.10: Microlayer appearing beneath the bubble in DNS conducted by and adapted from Urbano *et al.* [131].

The microlayer is also often taken into account for HFP modeling by enhancing the boiling heat flux through a computation of the microlayer volume [28, 71].

However, the presence of a liquid microlayer beneath the nucleated bubble is not assured for every boiling conditions. Indeed, experimental observations recently realized by Kossolapov [72] showed that the microlayer only existed for pressures below 3 bars when using water as working fluid. Moreover, Direct Numerical Simulations of Urbano *et al.* [131] where a full coupling between mass, momentum and energy balance was achieved managed to detect whether if the bubble grows in a contact-line regime or if a microlayer appears. They proposed a criterion based on the capillary and Jakob numbers determining the formation of a microlayer, further validated by extra Direct Numerical Simulations from Búres & Sato [12]:

$$\frac{\text{JaCa}}{(\theta - \theta_0)^3} > \frac{1}{A^3}, \quad \theta_0 = 5^\circ, \quad A = 313 \quad (6.83)$$

Remark : Computing the capillary number using $\dot{R} = \frac{K\text{Ja}}{2} \sqrt{\frac{\eta L}{t}}$ as the interface velocity, we use Urbano *et al.* criterion to compute the time t_{max} after which the microlayer would cease to exist. Applying this to PWR conditions ($K = 1$, $\Delta T_w = 5K$) yields $t_{max} < 10^{-11}\text{s}$ for $6^\circ \leq \theta \leq 90^\circ$, meaning that there is no time during the bubble growth during which a microlayer could grow. This agrees with the observation that increasing pressure would lead to microlayer disappearance.

We will not further detail the study of the microlayer regime since its existence is very unlikely if not impossible in the pressurized conditions typical of a PWR.

6.3.4 Bubble Growth in Subcooled Flow Boiling

If we consider the full problem of bubble growth in subcooled flow boiling, the analytic expressions presented above may fall out of their validation range since extra physical phenomena will be at stake. This more generic type of growth lack of proper theoretical derivations due to the complexity of the considered system (turbulence, condensation, convection, etc.). That is why authors trying to represent such complex bubble growth often combine different heat transfer mechanisms such as:

- Evaporation due to conduction from the superheated liquid near the bubble base ;
- Evaporation of the liquid microlayer ;
- Condensation on top of the bubble when it reaches subcooled liquid ;
- Convective heat transfer due to relative velocity between the bubble and the liquid.

To our knowledge, such models always consider empirical or fitted parameters. For instance Yoo *et al.* [139] wrote for a sliding bubble:

$$\frac{\partial R}{\partial t} = \underbrace{\gamma \text{Pr}_L^{-0.5} \text{Ja}_w \sqrt{\frac{\eta_L}{t}} \frac{A_{ML}}{A_b}}_{\text{Microlayer}} + \underbrace{(1-f) \frac{b}{\sqrt{\pi}} \text{Ja}_w \sqrt{\frac{\eta_L}{t}}}_{\text{Superheated liquid}} - \underbrace{\frac{f \Delta T_L C}{1 - \rho_V / \rho_L} R}_{\text{Subcooled convection}} \quad (6.84)$$

where $\gamma = \sqrt{\frac{\lambda_w \rho_w c_{p,w}}{\lambda_L \rho_L c_{p,L}}}$, $\frac{A_{ML}}{A_b} = 1.22 \gamma^{-0.79} \exp(-0.204 \text{Ja}_w)$, $f = 0.5$, $b = 0.24$ and $C = 0.1$.

Their model was validated against low pressure sliding of boiling bubbles for different fluids (Water [86], FC87 [125], R113 [136]). They account for wall properties through the parameter γ in the microlayer term while assuming that 50% of the bubble faces subcooled liquid ($f = 0.5$) and condenses following the formulation of Levenspiel [80].

Zhou *et al.* [145] also proposed a similar modeling of the bubble growth, validated on their own measurements for boiling water at low pressure:

$$\begin{aligned} \frac{\partial R}{\partial t} = & \underbrace{\frac{1}{C} \text{Pr}_L^{-0.5} \text{Ja}_w \sqrt{\frac{\eta_L}{t}}}_{\text{Microlayer}} + \underbrace{\sqrt{\frac{3}{\pi}} \text{Ja}_T \sqrt{\frac{\eta_L}{t}} \min\left(\frac{y_{sat}}{2R}, 1\right)}_{\text{Superheated liquid}} \\ & - \underbrace{\frac{\eta_L}{2R} \text{Ja}_L (2 + 0.6 \text{Re}_b^{0.5} \text{Pr}_L^{0.3}) \max\left(\frac{H - y_{sat}}{2R}, 0\right)}_{\text{Subcooled convection}} \end{aligned} \quad (6.85)$$

where $C = 1.45$, Ja_T is the Jakob number taken at $\min(\bar{T} - T_{sat}, 0)$, \bar{T} the average liquid temperature around the bubble, $H = R(1 + \cos(\theta))$.

While they consider a constant coefficient for the microlayer evaporation, they propose a finer modeling of the condensation term by evaluating the height y_{sat} at which $T_L = T_{sat}$ using the turbulent wall law of Kader [63]. The condensation is modeled by the Ranz & Marshall correlation [104] that accounts for the relative velocity through the bubble Reynolds number.

Remark : As mentioned before, those model rely on numerous empirical parameters due to the variety of considered phenomena. In particular, microlayer evaporation is systematically considered which could be questioned regarding the observations made in Subsection 6.3.3.

Contrary to those models, Mazzocco *et al.* [89] propose to keep the radius as $K \text{Ja}_w \sqrt{\eta_L t}$ and to include subcooling and microlayer influence in the value of K :

$$K = \frac{1.243}{\sqrt{\text{Pr}_L}} + 1.945 \chi \quad (6.86)$$

with

$$\chi = 1.55 \text{ (saturated flow)} \text{ or } \chi = -0.05 \frac{\Delta T_L}{\Delta T_w} \text{ (subcooled flow)} \quad (6.87)$$

Remark : This approach is interesting because it keeps the simple growth law in $t^{1/2}$, but K has to be set to 0 for regimes where $\frac{\Delta T_L}{\Delta T_w}$ is very large.

6.3.5 Analytic Approach of Bubble Growth in a Linear Thermal Boundary Layer

In this Subsection, we propose an analytic derivation of bubble growth for a truncated sphere laying on a wall in a boundary layer with a linear temperature profile. The considered geometrical and thermal definitions are depicted on Figure 6.11.

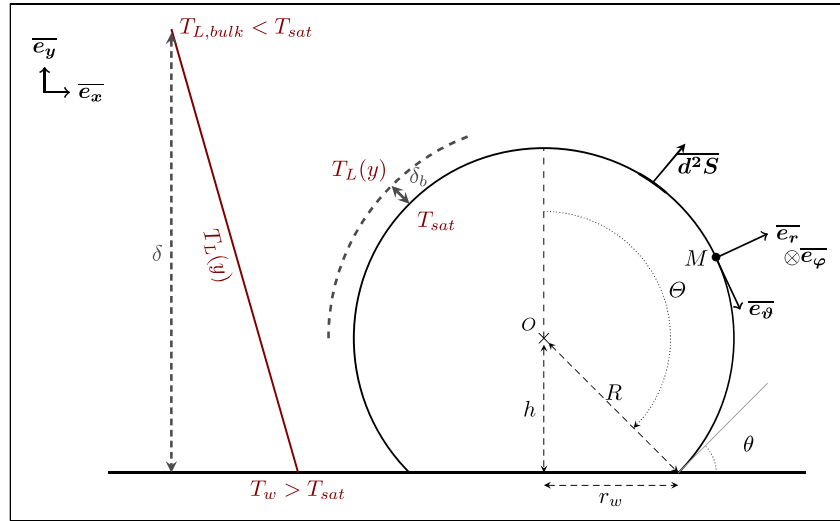


Figure 6.11: Studied geometry

We consider an established single-phase thermal boundary layer of thickness δ . When the bubble starts to grow, another boundary layer of thickness δ_b grows between the liquid-vapor interface and the surrounding liquid whose temperature depends on the wall distance y .

The liquid temperature is assumed to follow a linear profile:

$$T_L(y) = T_w + \frac{T_{L,bulk} - T_w}{\delta} y \quad (6.88)$$

Assuming that the vapor stays at a temperature close to T_{sat} , the radial component of the temperature gradient at the bubble's interface can be expressed as:

$$\bar{\nabla}(T) \cdot \bar{e}_r = \frac{\partial T}{\partial r}(R, \vartheta, \varphi) \approx \frac{T_L(y) - T_{sat}}{\delta_b} \quad (6.89)$$

Note : It is implicitly supposed that the heat flux within the vapor bubble is negligible, which is relatively reasonable since the vapor thermal conductivity is 7 to 28 times lower than that of the liquid water between 1 bar and 100 bar.

Applying Fourier's law to the liquid close to the bubble to estimate the heat flux density vector $\bar{j}_Q = -\lambda_L \bar{\nabla}(T)$. Between t and $t + dt$ the heat exchanged through d^2S is:

$$d^2Q_b \approx -\frac{\lambda_L}{\delta_b} \left[\Delta T_w R^2 \sin(\vartheta) - \frac{\Delta T_w + \Delta T_L}{\delta} R^3 [\cos(\vartheta) - \cos(\Theta)] \sin(\theta) \right] d\vartheta d\varphi \quad (6.90)$$

Then assuming that δ_b is constant between t and $t + dt$, the total heat flux can be expressed by integrating over the bubble's surface:

$$Q_b = \frac{2\pi\lambda_L R^2}{\delta_b} (1 + \cos(\theta)) \left[\Delta T_w - \frac{R}{2\delta} (\Delta T_w + \Delta T_L) (1 + \cos(\theta)) \right] \quad (6.91)$$

Writing the mass balance by considering that the heat flux contributes solely to phase change:

$$\frac{\partial V_b}{\partial t} = \frac{Q_b}{\rho_V h_{LV}} \quad (6.92)$$

$$V_b = \frac{4}{3}\pi R^3 f_V, \quad f_V = \frac{1}{4} (2 - \cos(\theta)) (1 + \cos(\theta))^2 \quad (6.93)$$

Writing this in terms of bubble radius:

$$\frac{\partial R}{\partial t} = \frac{\text{Ja}_w \eta_L}{2\delta_b f_V} (1 + \cos(\theta)) \left[1 - \frac{R}{2\delta} \left(1 + \frac{\text{Ja}_L}{\text{Ja}_w} \right) (1 + \cos(\theta)) \right] \quad (6.94)$$

Which reduces to the following differential equation:

$$\frac{\partial R}{\partial t} + aR = b \quad (6.95)$$

$$a = \frac{\text{Ja}_w \eta_L}{4\delta_b \delta f_V} \left(1 + \frac{\text{Ja}_L}{\text{Ja}_w} \right) (1 + \cos(\theta))^2 \quad \text{and} \quad b = \frac{\text{Ja}_w \eta_L}{2\delta_b f_V} (1 + \cos(\theta)) \quad (6.96)$$

Solutions of this differential equation depend on the hypothesis over δ and δ_b . If we assume that the bubble grows in a fully established liquid flow then δ can be considered as constant.

When the bubble will start to nucleate, the liquid-vapor interface will delimit a frontier through which a transient heat transfer between the vapor at constant temperature T_{sat} and liquid at $T_L(y)$ will occur. To estimate the associated local boundary layer thickness δ_b , we can rely on the solution of semi-infinite transient conduction as treated in Del Valle & Kenning [26] or Mikic & Rohsenow [93]:

$$\delta_b = \sqrt{\eta_L t} \quad (6.97)$$

The differential equation Eq. 6.95 becomes:

$$\frac{\partial R}{\partial t} + a(t)R = b(t) \quad (6.98)$$

$$a(t) = \frac{\text{Ja}_w \sqrt{\eta_L}}{4\delta f_V \sqrt{t}} \left(1 + \frac{\text{Ja}_L}{\text{Ja}_w} \right) (1 + \cos(\theta))^2 = K_a t^{-1/2} \quad (6.99)$$

$$b(t) = \frac{\text{Ja}_w \sqrt{\eta_L}}{2f_V \sqrt{t}} (1 + \cos(\theta)) = K_b t^{-1/2} \quad (6.100)$$

With the initial condition $R(t=0) = 0$, the solution to this differential equation is:

$$R(t) = R_\infty \left(1 - e^{-2K_a \sqrt{t}} \right) \quad (6.101)$$

$$R_\infty = \frac{K_b}{K_a} = \frac{2\delta}{\left(1 + \frac{\text{Ja}_L}{\text{Ja}_w} \right) (1 + \cos(\theta))} \quad (6.102)$$

This type of bubble growth presents interesting properties. First, it degenerates to the uniformly superheated liquid solution when $t \rightarrow 0$:

$$R(t) \underset{t \rightarrow 0}{\sim} \frac{1 + \cos(\theta)}{f_V} \text{Ja}_w \sqrt{\eta_L t} \quad (6.103)$$

with a purely geometrical growth constant depending on the contact angle, equal to 2 for the spherical case.

Moreover, this growth law accounts for the liquid subcooling and thus presents an equilibrium radius R_∞ when $t \rightarrow \infty$, corresponding to the bubble size at which the vaporization from the superheated liquid is exactly compensated by the condensation at the bubble top.

To the best of our knowledge, this simple bubble growth law has never been proposed in the literature. However, this equation has some limitations :

- It requires the knowledge of the liquid thermal boundary layer thickness δ which estimation can be tricky ;
- This law can't be applied if $T_{L,bulk} > T_{sat}$.

Remark : It is worthy to note that this solution is derived solely using the energy balance at the liquid-vapor interface. No momentum balance was used when solving this physical problem, which can be considered as a limit of the approach.

In addition, no modeling of the micro-region accounting for the specific phase change regime near the contact line have been considered.

6.3.6 Comparison with DNS Results

To assess the validity of Eq. 6.101, we will compare the radius time profile with DNS results by Urbano *et al.* [130] who simulated the same physical situation as depicted in Figure 6.11 for pool boiling. They also solved the heat conduction in the wall and studied the growth dynamics depending on the values of ΔT_L and ΔT_w as well as the equilibrium diameter reached by the bubble.

Note : The wall temperature in Urbano *et al.* work is imposed on the outer side of the simulated wall thickness contrary to the model where it is imposed directly at the inner side.

In their analysis, Urbano *et al.* derived the same equilibrium radius as in Eq. 6.102 by equating the condensation and vaporization heat fluxes. By comparing with the equilibrium radius reached in their simulations, they found that a corrective factor $C = 1.15829$ was needed to correct Eq. 6.102. This difference could be explained by the heat conduction in the wall that is not accounted for in the theoretical approach.

DNS results obtained for three couples of subcooling ΔT_L and superheat ΔT_w are used for comparison. Results are displayed on Figure 6.12 with and without the corrective factor on R_∞ suggested by Urbano *et al.*

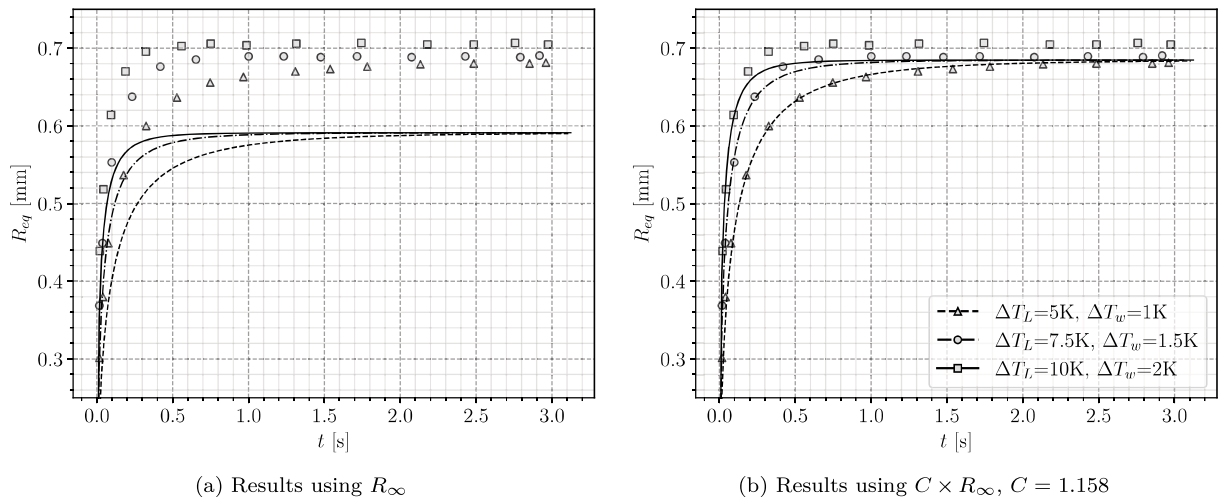


Figure 6.12: Comparison with DNS results of Urbano *et al.* [130] ($\delta = 3\text{mm}$ and $\theta = 50^\circ$). Lines : Model predictions - Markers : DNS

The analytical formulation of the bubble growth matches very well with the DNS results when the equilibrium radius is corrected. The different growth regime induced by the pairs $(\Delta T_L, \Delta T_w)$ are correctly captured by the model. DNS results present different equilibrium radius values when the subcooling and superheat changes, which can not be accounted for by the model.

Remark : Those results are encouraging and validate the modeling of δ_b with the semi-infinite conduction model (Eq. 6.97).

6.3.7 Comparison with Experimental Measurements

6.3.7.1 Low Pressure Measurements

To further evaluate the proposed model, we compare the result with experimental measurements of bubble radius in vertical boiling of water at atmospheric pressure by Maity [86]. The choice of δ is adapted to each case and $\theta = 45^\circ$ is the average measured contact angle in the experiments.

In addition, we also plot the predictions by the heat diffusion solution $R = KJa_w\sqrt{\eta_L t}$ with $K = \frac{2b}{\sqrt{\pi}}$ and $1 \leq b \leq \sqrt{\pi}$. A solution with an optimized value of K is also represented. The models of Mazzocco and Yoo *et al.* are also compared. The results are presented on Figure 6.13.

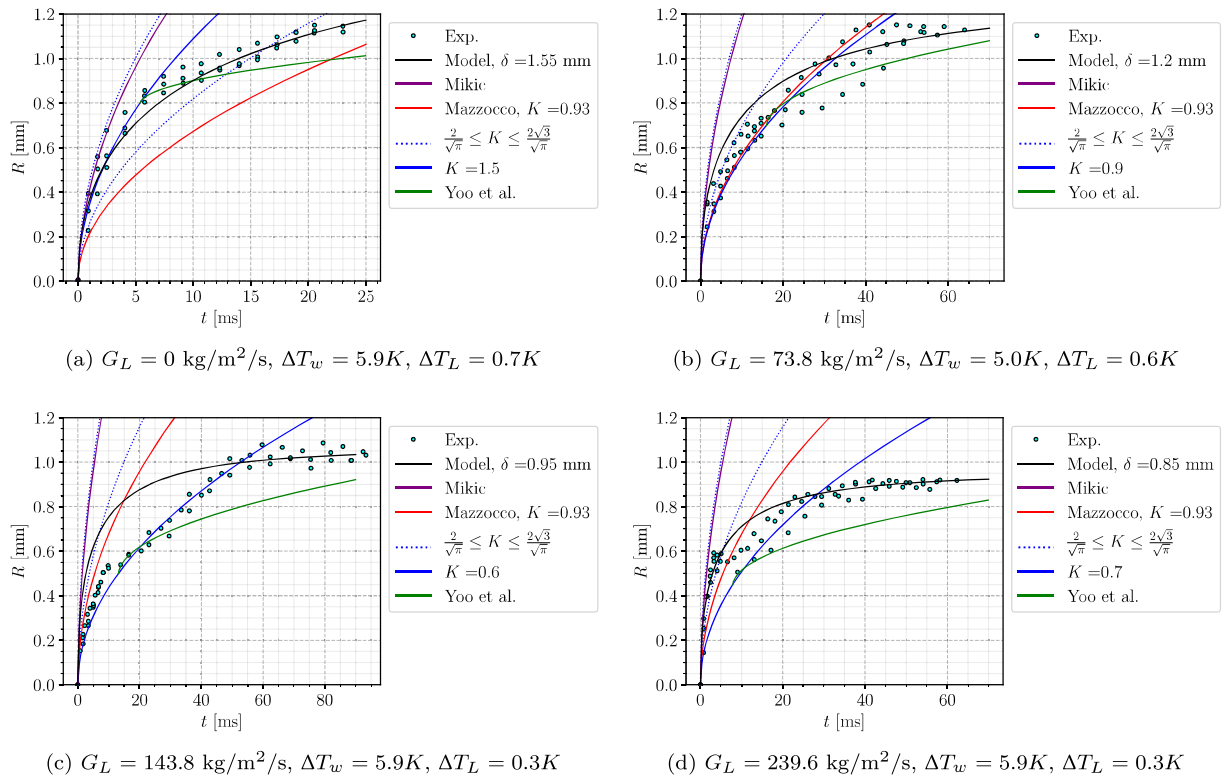


Figure 6.13: Comparison with experimental measurements of Maity [86].

The new formulation globally reproduces the experimental results better than the other models. In particular, the progressively damped growth rate when the bubble start to face colder liquid seems to correctly captures the nonlinear experimental growth. Values of δ needed to produce those results were between 0.85 mm and 1.55mm, which reasonably agrees with measurements of Maity in his experiment for horizontal flow giving δ roughly between 1 mm and 1.5 mm. We can note that the optimal value of δ decreases as liquid mass flux increases, which is physically coherent as the thermal boundary layer will diminish in size with the Reynolds number.

Remark : Actually, the thermal boundary layer thickness δ depends on many parameters such as the liquid Prandtl number and mass flow rate, the heater properties and heat flux, etc.

If the total wall heat flux ϕ_w is transmitted to the liquid by conductive heat transfer in the linear boundary layer, we can write:

$$\phi_w = \lambda_L \frac{\Delta T_L + \Delta T_w}{\delta} \quad (6.104)$$

On the other hand, the fitted value of K is often smaller than the lower bound $\frac{2}{\sqrt{\pi}}$ suggested by Zuber [147]. This is a consequence of the subcooled flow which deviates from the uniformly superheated liquid from which those values were derived. This fitted profile manages to capture some stages of bubble growth but can not predict the asymptotic behavior where bubble reaches a quasi-constant radius. We see that the model of Mikic & Rohsenow produces results that are nearly identical to the $K = 2\sqrt{3/\pi}$ solution. The growth constant computed by Mazzocco *et al.* (Eq. 6.86) is constant over the four cases and lower than $2/\sqrt{\pi}$ which is slightly better than other analytic values of K but underestimates the pool boiling case.

Finally, we see that the model of Yoo *et al.* underestimates the bubble radius. We suspect this could come from the assumption considering that half of the bubble faces subcooled liquid ($f = 0.5$, Eq. 6.84), which is hardly reasonable especially at early growth stages.

To test the sensitivity of the model to the value of δ , we plot on Figure 6.14 the Maity case at $G_L = 239.6 \text{ kg/m}^2/\text{s}$ for values of $\delta \pm 50\%$.

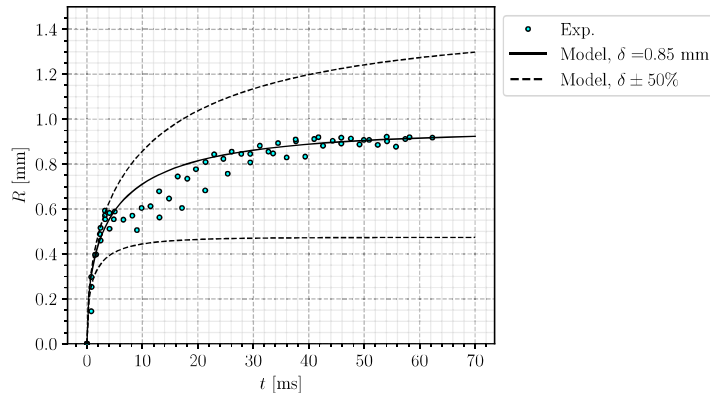


Figure 6.14: $G_L = 239.6 \text{ kg/m}^2/\text{s}$, $\Delta T_w = 5.9K$, $\Delta T_L = 0.3K$

The value of δ controls the value of R_∞ and thus significantly impacts the transient growth profile. The estimation of the thermal boundary layer thickness is then an important aspect to ensure a correct prediction of the bubble growth.

6.3.7.2 High Pressure Measurements

The model is now compared to higher pressure measurement (20 bar and 40 bar) for water boiling by Kossolapov [72]. All the experiments are conducted with 10K of subcooling, and we take a contact angle of $\theta = 80^\circ$ (typical for water and ITO). The range of the measured diameters over time are represented since Kossolapov observed the growth of thousands of bubbles over the heater surface. Results are presented on Figure 6.15.

The values of δ needed to match the experimental measurements using Eq. 6.101 are much smaller than the low pressure case, with $\delta \leq 0.1 \text{ mm}$. The higher mass fluxes in Kossolapov measurements could explain lower values of δ , nevertheless they do not follow a particular trend with G_L .

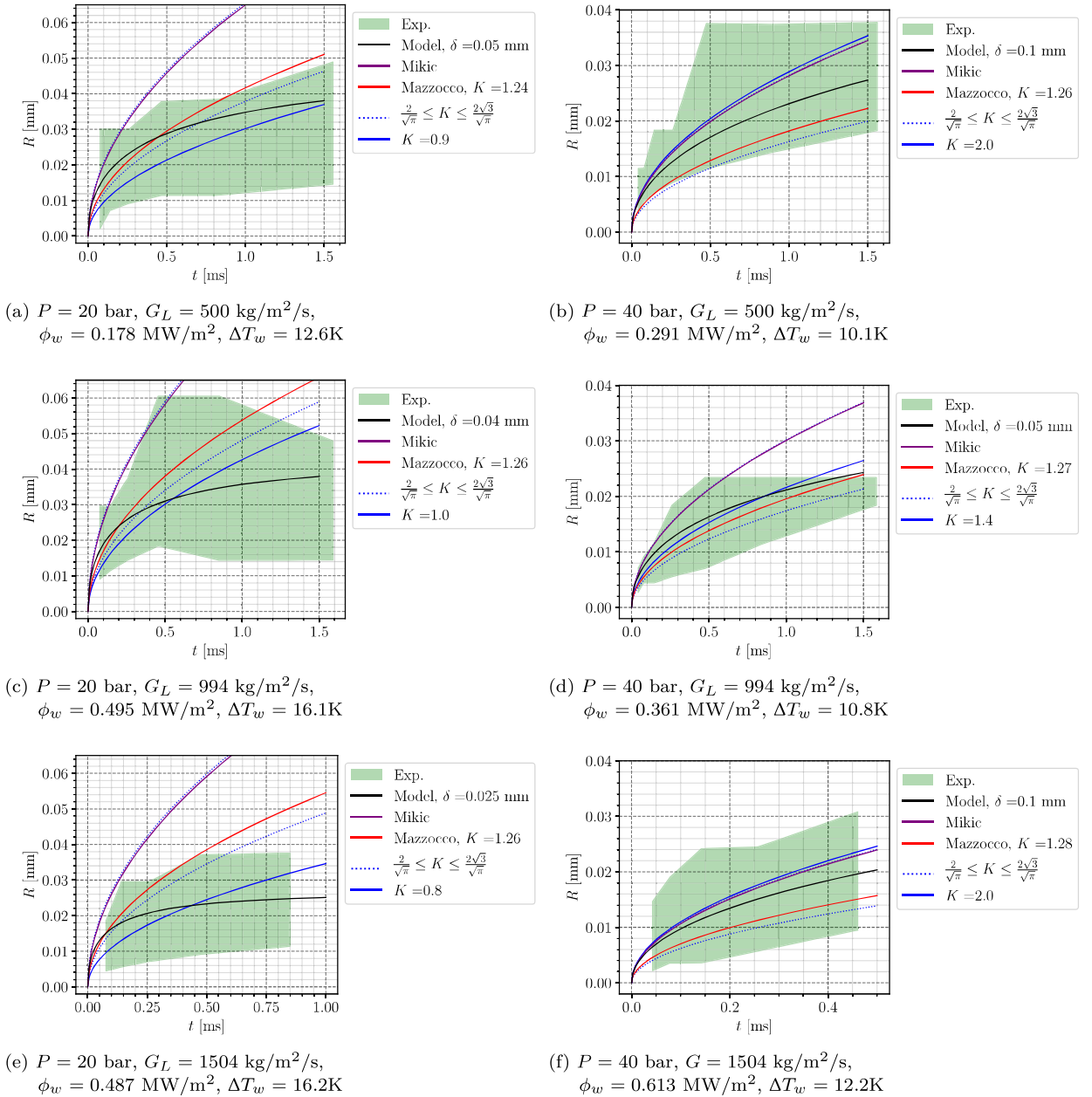


Figure 6.15: Comparison with experimental measurements of Kossolapov [72]. ΔT_w values are recalculated from analytical growth profiles fitted by the author.

Contrary to low pressure measurements, the Plesset & Zwick solution with $\frac{2}{\sqrt{\pi}} \leq K \leq \frac{2\sqrt{3}}{\sqrt{\pi}}$ provides an acceptable estimation of the bubble radius. This is probably due to the smaller bubble size in pressurized boiling (roughly 10 times smaller compared to atmospheric pressure).

Remark : The non-dimensional positions of the center of gravity of the bubble $R^+ = \frac{R u_\tau}{\nu_L}$ rise up to 40 for Maity cases and 20 for Kossolapov cases while having larger liquid mass fluxes. This supports the fact that bubbles at higher pressure are less likely to be impacted by subcooled liquid, spending most of their lifetime between the viscous and buffer layer.

Note that this assumption is true if the thermal and hydrodynamic boundary layers are close, which is often assumed in numerical simulations under the assumption of a unity turbulent Prandtl number $\text{Pr}_T \approx 1$ (Eq. 2.43).

6.3.8 Conclusions on Bubble Growth Modeling

- Recent experimental and numerical research have shown that the presence of a liquid microlayer contributing to the bubble growth strongly depends on the boiling conditions. In particular, disappearance of this microlayer at pressures higher than 3 bar has been observed by Kossolapov [72]. This microlayer should thus not be systematically taken into account.
- A new formulation derived from the heat diffusion in a linear temperature profile has been proposed (Eq. 6.101). Provided a correct value of the thermal boundary thickness δ , validation both on DNS and low pressure measurements shows that the model better captures the growth regime of bubbles in subcooled boiling compared to traditional models. However, this improvement appears limited at higher pressure when bubbles are smaller, where the Plesset & Zwick treatment also proposes an acceptable estimation of the bubble growth.
- Mechanistic models that includes several heat transfer mechanisms require a certain number of empirical closures that limits the model generality, making them unsuitable for application to any boiling conditions.
- Whatever the conditions, a proper choice of the growth constant K in the $R = K \text{Ja}_w \sqrt{\eta_L t}$ solution for a uniform liquid superheat can yield reasonable results. Moreover, it presents interesting mathematical properties such as the time independence of the products $R\dot{R}$ and $R^3\ddot{R}$ that appear in the bubble force balance (Eq. 6.69).

All things considered, it seems that the proposed new growth law of Eq. 6.101 can be of greater interest for low pressure boiling where larger bubbles are more impacted by the bulk flow. Although it provides finer physical representation of bubble radius evolution, its application is limited by the estimation of δ to which the model is strongly sensitive. **On the other hand, less precise yet acceptable predictions of bubble growth are achieved using the $t^{1/2}$ law with a growth constant K close to unity.**

6.4 DEPARTURE BY SLIDING

The question of departure by sliding being central for bubble dynamics in vertical flow boiling, we will tackle the problem by starting with a non-dimensional analysis before moving to predictions of experimental measurements of departure diameters.

6.4.1 Non-Dimensional Analysis

To study the departure by sliding, we rely on force balance parallel to the wall (Eq. 6.68). Before departure, the bubble grows on its nucleation site while staying immobile, thus with a sliding velocity $U_b = \frac{\partial U_b}{\partial t} = 0$. The force balance parallel to the wall becomes:

$$-\pi R \sigma f_{C,x} + \frac{4}{3} \pi R^3 (\rho_L - \rho_V) g + \frac{1}{2} C_D \rho_L \pi R^2 U_L^2 + \frac{4}{3} \pi R^3 \rho_L 3 C_{AM,x} \frac{\dot{R}}{R} U_L = 0 \quad (6.105)$$

We can note that in this equation, departure by sliding is promoted by the buoyancy, the drag and the added mass forces. Only the capillary force keeps the bubble attached to its nucleation site, which will be discussed later. As discussed in the previous section, the bubble growth is modeled as:

$$R(t) = K \text{Ja}_w \sqrt{\eta_L t} \quad (6.106)$$

with K as an adjustable constant.

Re-writing Eq. 6.105 in non-dimensional form by dividing the LHS by the added mass force yields:

$$-\frac{1}{2} \frac{f_{C,x}}{K^2 C_{AM,x}} \frac{1}{\text{Ca}} \frac{\text{Pr}_L}{\text{Ja}_w^2} + \frac{1}{3} \frac{1}{K^2 C_{AM,x}} \frac{\text{Re}_b}{\text{Fr}} \frac{\text{Pr}_L}{\text{Ja}_w^2} + \frac{1}{8} \frac{C_D}{K^2 C_{AM,x}} \text{Re}_b \frac{\text{Pr}_L}{\text{Ja}_w^2} + 1 = 0 \quad (6.107)$$

where we have the following non-dimensional numbers:

$$\begin{aligned} \text{Re}_b &= \frac{2R U_L}{\nu_L} ; \quad \text{Fr} = \frac{\rho_L U_L^2}{(\rho_L - \rho_V) g R} ; \quad \text{We} = \frac{\rho_L U_L^2 R}{\sigma} ; \quad \text{Eo} = \frac{(\rho_L - \rho_V) g R^2}{\sigma} ; \\ \text{Ja}_w &= \frac{(T_w - T_{sat}) \rho_L c_{P,L}}{\rho_V h_{LV}} ; \quad \text{Pr}_L = \frac{\nu_L}{\eta_L} ; \quad \frac{\dot{R}}{U_L} = \frac{K^2 \text{Ja}_w^2}{\text{Pr}_L \text{Re}_b} ; \quad \text{Ca} = \frac{\mu_L U_L}{\sigma} \end{aligned}$$

Eq. 6.107 exhibits terms that can be used to compare the magnitude of each detaching forces and obtain the following conditions:

$$\text{Added mass force greater than drag if: } \frac{\text{Ja}_w^2}{\text{Pr}_L} > \frac{1}{8} \frac{C_D}{C_{AM,x}} \frac{1}{K^2} \text{Re}_b \quad (\text{Bd. 1})$$

$$\text{Added mass greater than buoyancy if: } \frac{\text{Ja}_w^2}{\text{Pr}_L} > \frac{1}{3} \frac{1}{C_{AM,x} K^2} \frac{\text{Re}_b}{\text{Fr}} \quad (\text{Bd. 2})$$

$$\text{Drag greater than buoyancy if: } \text{Fr} > \frac{8}{3} \frac{1}{C_D} \quad (\text{Bd. 3})$$

Those three conditions can be seen as boundaries in a $(\text{Ja}_w^2/\text{Pr}_L ; \text{Re}_b)$ plane. With a given fluid and bubble diameter $D = 2R$, we can represent the different regimes of force dominance by plotting those three boundaries simultaneously on a regime map. Eq. Bd. 3 corresponds to a vertical line in the plane since $C_D \sim \frac{1}{\text{Re}_b}$. An example of such a map is presented on Figure 6.16.

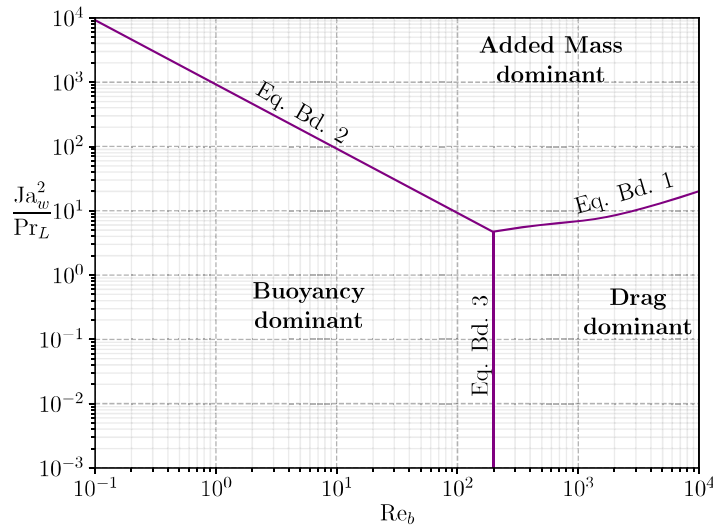


Figure 6.16: Regime map regarding departure by sliding. Boundaries plotted for water at 1 bar and $D_d = 0.5\text{mm}$. ($K = 2$)

This allows to visualize the operating conditions under which each of the detaching forces will be dominant. Logically, buoyancy dominates for low Fr numbers, thus low Re_b regimes contrary to drag. Added mass dominates when values of $\text{Ja}_w^2/\text{Pr}_L$ are high *i.e.* when bubble grows rapidly.

6.4.1.1 Influence of Pressure

On Figure 6.17, we draw the regime map for 3 different pressures and associated orders of magnitude of bubble departure diameter [69].

The impact of pressure is mostly seen through the decrease of bubble departure diameter. As pressure increases, buoyancy force decreases while drag and added mass forces display much larger dominance zones. The competition between those two terms mainly relies on the competition between liquid flow velocity and wall superheat or heat flux.

6.4.1.2 Comparison between Fluids

On Figure 6.18, we compare the dominance zones for R12 at 26 bar and water at 155 bar. Moderately pressurized R12 (10 to 30 bar) has often been used as a simulating fluid to mimic water in PWR since

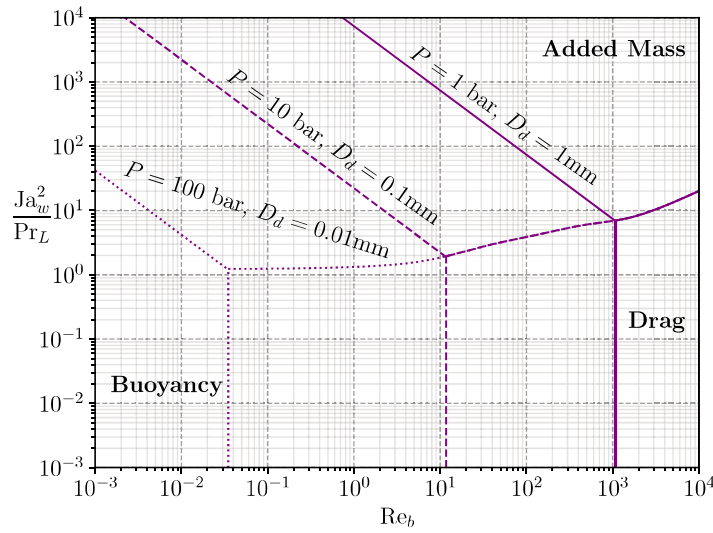


Figure 6.17: Regime map plotted for water at different pressures and bubble departure diameters. ($K = 2$)

it has the same density ratio and Weber number for instance (see Chapter 3 related to the DEBORA experiments).

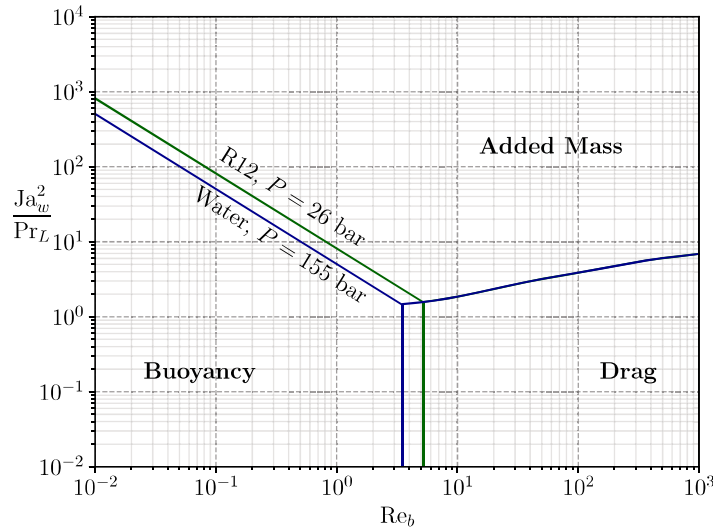


Figure 6.18: Regime map for R12 as simulating fluid for PWR. $D_d = 0.05\text{mm}$ is chosen according to R12 measurements from Garnier *et al.* [41] who observed bubbles of $\sim 0.1\text{mm}$ diameter after lift-off. The same value is taken for water. ($K = 2$)

Assuming that the conservation of Weber and Boiling numbers may lead to similar bubble departure diameters, we can observe that the boundaries between the two fluids are very close. This qualitatively indicates that R12 shall present bubble departure by sliding mechanisms similar to what happens in PWR.

Remark : This approach could easily be applied to comfort the confidence one may have in extrapolating the observations done using a simulating fluid to industrial applications.

6.4.2 Application to Experimental Data

Now we want to apply this non-dimensional approach to experimental measurement in order to determine the actual bubble departure by sliding regimes. We rely on 7 experiments in which bubble departure diameters in vertical flow boiling were measured. The operating conditions are gathered in Table 6.3.

Author	Fluid	D_h [mm]	P [bar]	G_L [kg/m ² /s]	ΔT_L [K]	ϕ_w [kW/m ²]	ΔT_w [K]	D_d [mm] (N_{mes})
Thorncroft [125] (1998)	FC-87	12.7	N.A.	0 - 319	0.99 - 3.27	2.83 - 11.8	0.54 - 6.89	0.094 - 0.237 (10)
Maity [86] (2000)	Water	20	1.01	0 - 239.6	0.3 - 0.7	N.A.	5 - 5.9	0.788 - 1.71 (9)
Chen [15] (2012)	Water	3.8	1.2 - 3.35	214 - 702	14.5 - 30.3	83.6 - 334	N.A.	0.549 - 2.255 (22)
Sugrue [120] (2014)	Water	16.6	1.01	250 - 400	10 - 20	50 - 100	2 - 6	0.229 - 0.391 (16)
Guan [50] (2014)	Water	9	1.01	87.3 - 319.2	8.5 - 10.5	68.2 - 104	4.5 - 8.5	0.62 - 1.85 (12)
Ren [107] (2020)	Water	3.8	2 - 5.5	488.4 - 1654	28.7 - 51	160.7 - 643.2	N.A.	0.045 - 0.111 (42)
Kossolapov [72] (2021)	Water	11.8	19.9 - 39.8	500 - 1500	10	178 - 613	10.1 - 16.2	0.01 - 0.047 (11)

Table 6.3: Bubble departure diameters data sets in vertical flow boiling

If the value of ΔT_w is not available in the considered data-set, we estimate it ΔT_w using Frost & Dzakowic correlation [39]:

$$\Delta T_w = \text{Pr}_{L,sat} \sqrt{\frac{8\sigma\phi_w T_{sat}}{\lambda_L \rho_V h_{LV}}} \quad (6.108)$$

To place experimental measurements on the non-dimensional map, we need a bubble detachment diameter value D_d to plot the dominance zones. Since measured D_d vary significantly in each experiment, we draw the boundaries for the maximum and minimum values of D_d as shown on Figure 6.19a. If the considered data covers different pressures, boundaries for each pressure are plotted to exhibit its impact (Figures 6.19d, 6.19e and 6.19f). We chose a value of $K = 1$ to draw the boundaries.

The Figure 6.19 shows that for most of the low pressure experiments, the detaching forces are the added mass and the buoyancy. Smaller bubbles are mainly detached under the effect of the added mass force (Figures 6.19c, 6.19d and 6.19e). When the bubbles detach at higher diameters, the impact of the buoyancy force naturally increases and is comparable to the added mass force (Figures 6.19a and 6.19b).

When the pressure increases, we observe that the experimental measurements gradually move towards the drag dominant zone as seen on Figures 6.19e and 6.19f. This main difference in the dynamic regime when bubble departs by sliding arises from multiple effects:

- The decrease of ρ_L / ρ_V with pressure, thus reducing Ja_w and the impact of the detaching added mass term ;
- The higher liquid mass fluxes in Kossolapov experiments, increasing the impact of the drag ;
- The decrease of D_d with pressure, reducing the magnitude of buoyancy.

However, we see that some measurements lie close to the added mass / drag boundary (Figure 6.19f), indicating that the added mass force still plays a significant role for bubble detachment. This means that regardless of the operating pressure, the detaching term associated to the coupling between bubble growth and outer liquid flow should not be neglected in the force balance (Eq. 6.105).

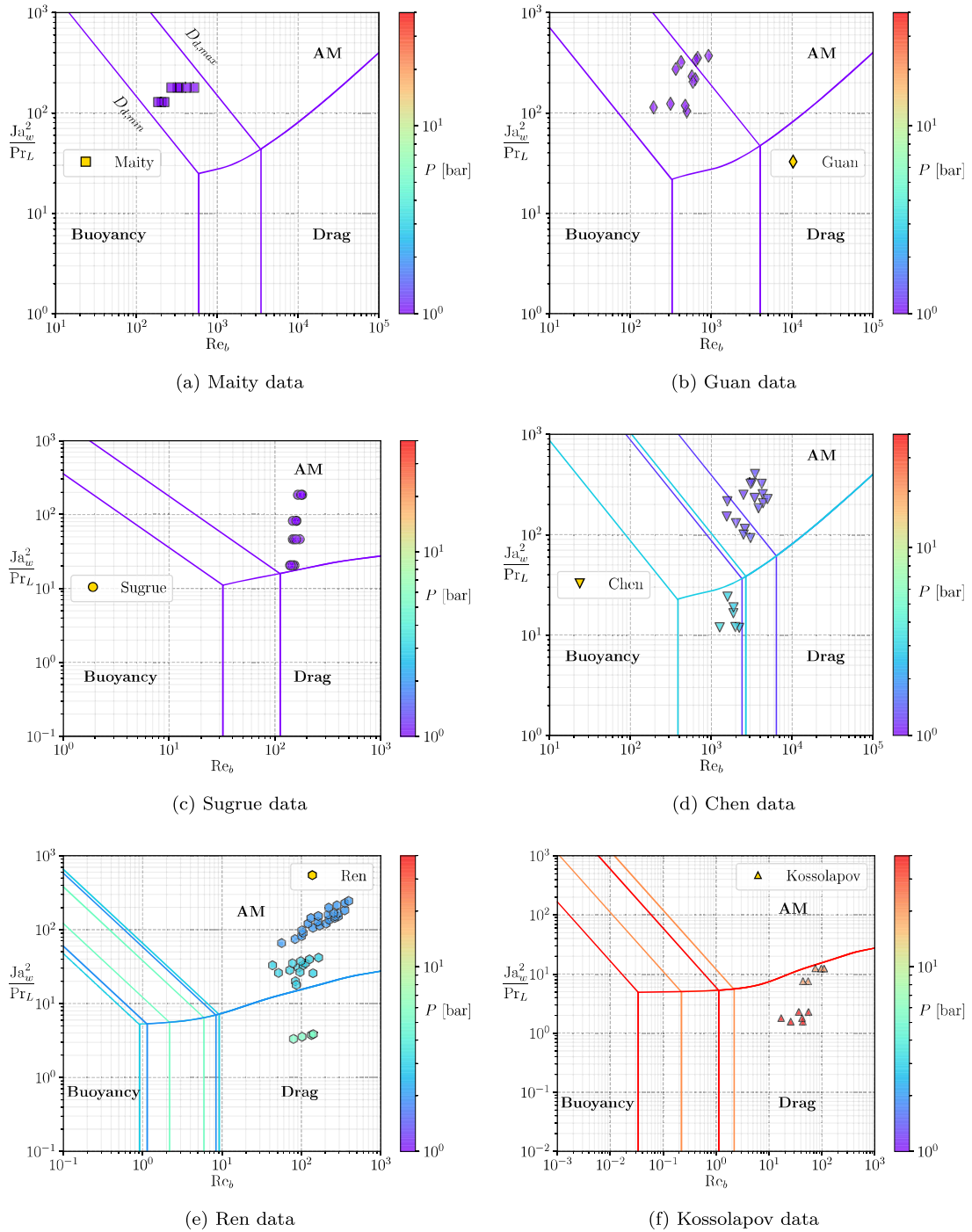


Figure 6.19: Regime maps for each water data sets from Table 6.3.

6.4.3 Departure Diameter Prediction

6.4.3.1 About the Use of Empiricism

As previously mentioned, the case of bubble detachment in vertical flow boiling is particular since only one force maintains the bubble attached to its nucleation site: the capillary force (Eq. 6.105). Its expression depends on the contact angle θ , the half-angle of hysteresis $d\theta$ and the bubble foot radius r_w (or ratio to bubble diameter r_w/R) and is thus very sensitive to those values.

Paradoxically, those terms are among the least precisely known due to the difficulty of measurement and associated uncertainties. For instance, conducting precise evaluations of the contact angle near the bubble

base through optical techniques can be challenging because of the strong temperature gradients close to the heated surface leading to a strong deformation of the bubble image.

Consequently, empirical choices have to be made in order to set a value to those parameters, often by relying on data-fitting or approximate measurements in other conditions. For instance, contact angles are often taken as arbitrary average values [107] or measurements in room conditions [120] and applied over a whole set of experiments. This is questionable since contact angle is unlikely to remain unchanged over different operating conditions and surfaces with varying roughness, properties and wall superheat. [118].

However, no better information except those given by the authors can be used to evaluate the capillary force since no generic model exist to compute the contact angle and hysteresis. In this work, admitting a significant uncertainty (typically 5°, as in Guan [50]), we will use the following values for the contact angles :

- $\theta_u = 25.3^\circ$ and $\theta_d = 6.6^\circ$ for Thorncroft data (measured values for FC-87 on nichrome [126]) ;
- $\theta_u = 50^\circ$ and $\theta_d = 40^\circ$ for Maity data (measured average contact angles for each bubble during its lifetime [86]) ;
- $\theta_u = 130^\circ$ and $\theta_d = 65^\circ$ for Chen data (chosen values in their study following measurements for water on stainless steel at high temperature by Kandlikar *et al.* [64]) ;
- $\theta_u = 91^\circ$ and $\theta_d = 8^\circ$ for Sugrue data (measured values at room temperature [122]) ;
- $\theta_u = 75^\circ$ and $\theta_d = 30^\circ$ for Guan data (measured average value through experimental visualizations [50]) ;
- $\theta_u = 45^\circ$ and $\theta_d = 36^\circ$ for Ren data (chosen values in their study [107]) ;
- $\theta = 80^\circ$ for Kossolapov data (typical contact angle for water on ITO [72]) and $d\theta = 1^\circ$ assuming that the very small bubbles at high pressure are nearly not tilted.

Similarly, the bubble foot radius r_w is often empirically assumed to be either constant [66] proportional to the bubble radius [89, 120] or to follow a linear or logarithmic law of R [50, 145]. That is why we chose to use the truncated sphere hypothesis (Eq. 6.14) to compute r_w using R and θ .

Finally, we would like to acknowledge that the empiricism to evaluate those parameters represents one of the biggest flaws of the force-balance approach. Indeed, such a model aims to detect small sign changes in a sum of a few μN of forces that are decades larger as pointed out by Bucci *et al.* [11]. Mechanistic models are thus strongly sensitive to any extra parameter included in the modeling of the forces.

6.4.3.2 Growth Constant Value

As discussed in Section 6.3, a value close to one or lower for the contant K in the bubble growth rate usually provides reasonable approximation of the bubble radius. In particular, subcooled flow boiling may need smaller values of K , as well as fluids with high Prandtl numbers.

To avoid a systematic overestimation of the added mass term which could lead to strong underestimations of the departure diameter in cases that would present strong subcoolings, liquid velocity or working fluids with low thermal conductivity, we will use:

$$K = \frac{2b}{\sqrt{\pi}}, \quad b = 0.24 \quad (6.109)$$

as proposed by Yoo *et al.* [139] to model the superheated liquid diffusion growth term.

6.4.3.3 Predictions

We consider the non-dimensional force balance before departure.

$$C_{AM,x}K^2 \frac{\text{Ja}_w^2}{\text{Pr}_L} + \frac{1}{3} \frac{\text{Re}_b}{\text{Fr}} + \frac{1}{8} C_D \text{Re}_b = \frac{1}{2} \frac{f_{C,x}}{\text{Ca}} \quad (6.110)$$

Since we only have the capillary term hindering departure as a first approach, we can suppose that departure is reached when:

$$C_{AM,x}K^2 \frac{\text{Ja}_w^2}{\text{Pr}_L} + \frac{1}{3} \frac{\text{Re}_b}{\text{Fr}} + \frac{1}{8} C_D \text{Re}_b > \frac{1}{2} \frac{f_{C,x}}{\text{Ca}} \quad (6.111)$$

which is similar to considering that the other forces overcome the capillary force.

On Figure 6.20, we show the predictions obtained with the proposed modeling and those obtained with Mazzocco's recent model [89] (see Table 6.2).

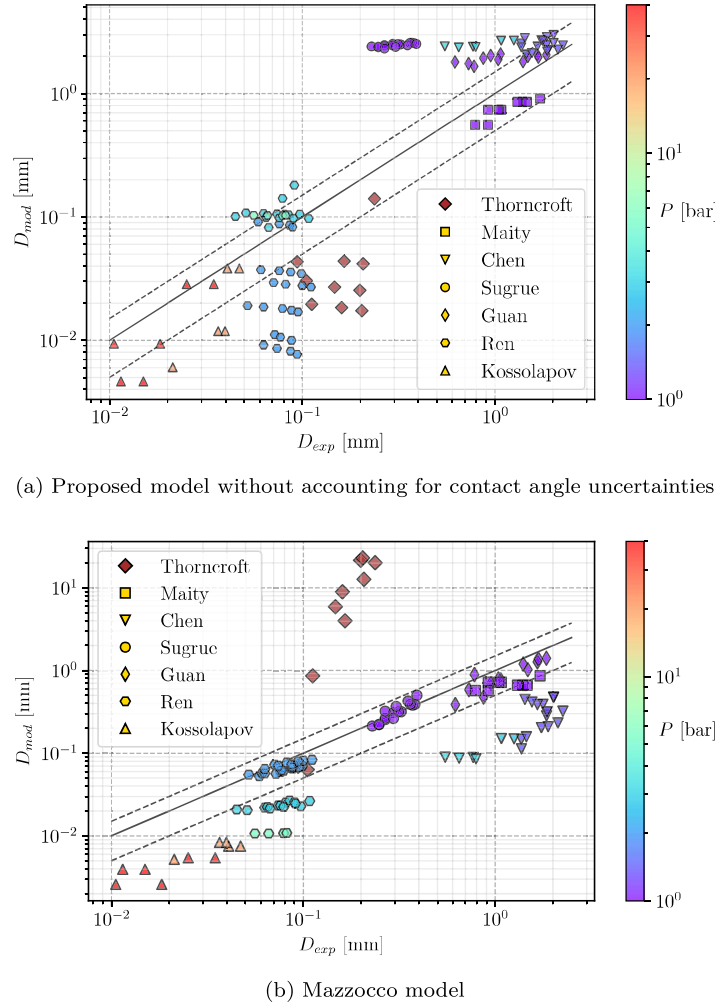


Figure 6.20: Predicted bubble departure diameters. $\pm 50\%$ error bars are indicated.

The model has an acceptable trend on some experimental sets, but strong overestimation occur on the cases of Sugrue. Moreover, we observe significant underestimations on the data of Ren at 2 bar and Thorncroft.

Mazzocco's model provides a good accuracy on the data of Sugrue, Guan, Maity and Ren (2 bar). However, we observe very large overestimation over Thorncroft's measurements and significant underestimation on Chen, Ren (3 and 5 bar) and Kossolapov measurements.

6.4.4 Discussion and accounting for parameters uncertainties

The aforementioned errors observed for the proposed model may originate from various reasons:

- The contact angle proposed for Sugrue cases is high with a large hysteresis, suggesting strongly deformed and flattened bubbles under the truncated sphere hypothesis. Based on images from Sugrue's work [121], a comparison between a real bubble with the assumed shape is presented on Figure 6.21. This shows a huge difference which indicates that the contact angle and hysteresis values may be overestimated. Using the available images, the ratio of the bubble diameter to the

apparent bubble foot would lead to an average contact angle $\theta \approx 20^\circ$ for a truncated sphere. Noting that a larger inclination is observed for the bubbles under higher mass fluxes leads us to suppose a value $d\theta \approx 15^\circ$. This represent a similar inclination to contact angle ratio ($d\theta/\theta$) compared to the initially proposed values. The resulting new shape is also presented on Figure 6.21 and seem to better represent the actual bubble.

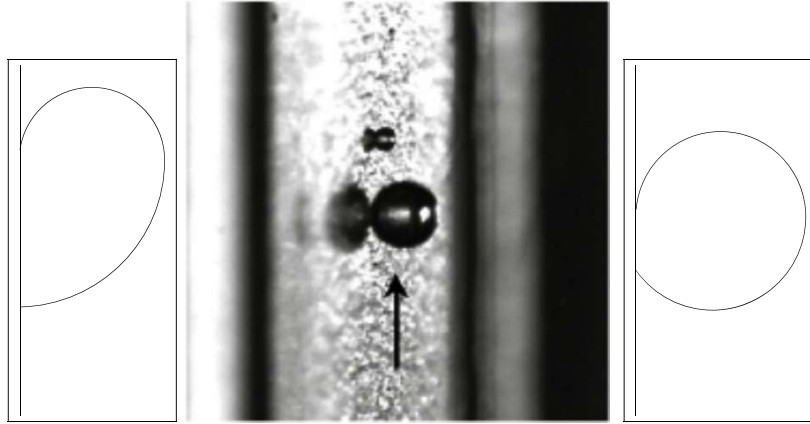


Figure 6.21: Initially assumed, real and reassessed bubble shape for Sugrue cases (picture adapted from [121]).

- For cases where limited under and overestimation is observed, we may allow to account for an uncertainty as high as 5° for the average contact angle θ and half-hysteresis $d\theta$.
- As mentioned earlier, applying the same contact angle and hysteresis over a wide range of measurements is a strong assumption, especially for cases where different pressures and bubble diameter variations are observed. Thus, we may slightly distinguish the applied values of θ and $d\theta$ for different pressures within a given experiment, keeping a change no larger than 5° .
- Kossolapov cases at $G_L = 500 \text{ kg/m}^2/\text{s}$ are better predicted. Cases under higher mass fluxes (1000 and $1500 \text{ kg/m}^2/\text{s}$) present underestimation that could come from the value of $d\theta$. At such mass fluxes, the Weber number can be up to a decade higher and bubbles may thus accept a larger inclination before detachment.
- Cases of Ren and Chen rely on chosen values for θ and $d\theta$ and not on measured ones. They are therefore subject to strong uncertainties. We can note that the values for Chen cases are significantly high.
- The proposed growth law is still rather simple and may miss significant information, especially regarding bubble size and fluid properties such as the Prandtl number.
- Errors on Thorncroft cases may be linked to uncertainties regarding FC-87 properties. Indeed, we use the values given at $T_{sat} = 29^\circ$ at 1 bar in his work [125]. However, the saturation temperature indicated in his test matrix is close to 40° which means that measurements were conducted at a higher pressure, for which we do not have FC-87 properties.

Therefore, using modified values of θ and $d\theta$ among experimental data sets with no more than a 5° change (except for Sugrue cases reassessed values) leads to predictions on Figure 6.22.

The predictive capacity of the model is significantly enhanced, especially on Sugrue's cases which tends to indicate that the contact angle reassessment was justified under the truncated sphere hypothesis. Table 6.4 summarizes the average errors obtained with the present model and Mazzocco's one.

The proposed model achieves an overall better predictive capability even when excluding measurements from Thorncroft on which Mazzocco's model strongly overestimates the departure diameter. Mazzocco's model is still better on Sugrue and Guan cases since it was built and validated using those measurements. It better predicts results from Ren but only for the 2 bar cases while it underestimates the departure diameter for higher pressures. Those results are a coupled effect of his optimized growth law along with the imposed value of r_w/R and the use of the inclination angle to hinder departure as mentioned in 6.2.6.

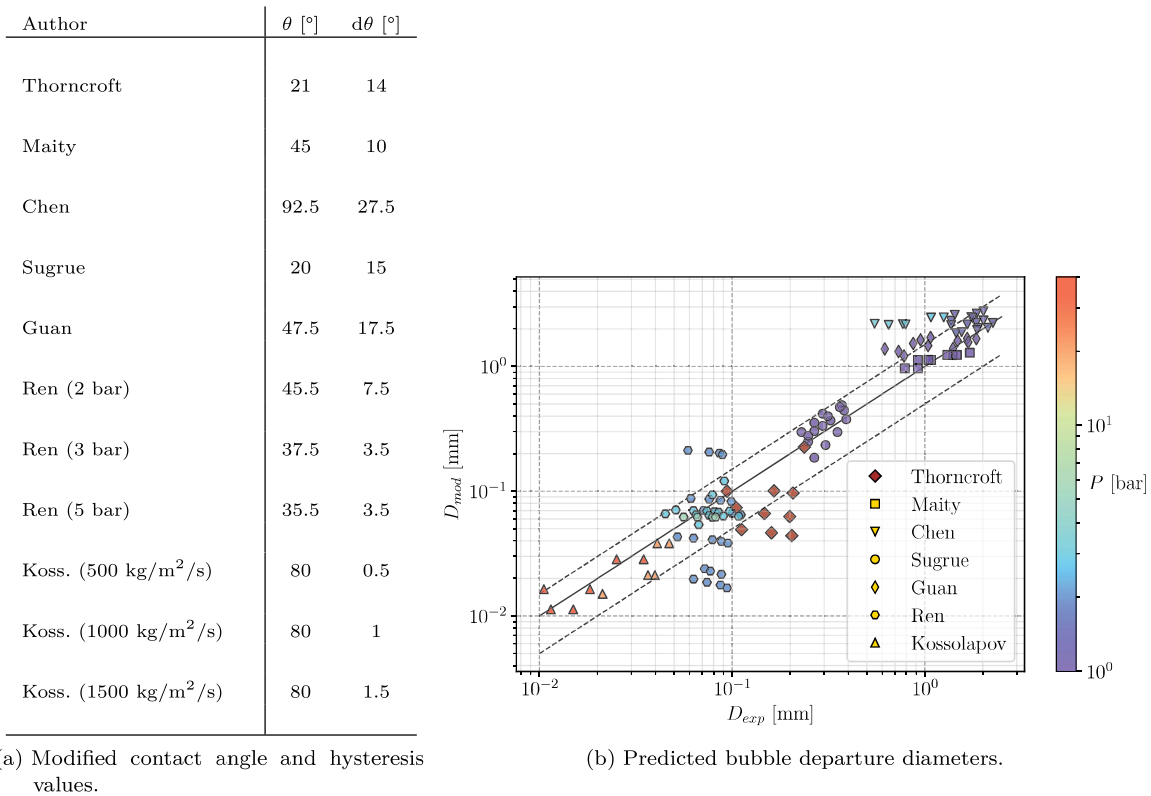


Figure 6.22: Proposed model performance while accounting for contact angle uncertainties

Author	Mazzocco	Present model
Thorncroft	4874%	46.2%
Maity	39.7%	13.8%
Chen	83.8%	73.6%
Sugrue	9.73%	21%
Guan	25.5%	44.5%
Ren	40.32%	47%
Kossolapov	78.3%	24.2%
Total (without Thorncroft)	46.58%	43.3%

Table 6.4: Average relative error reached by the models.

The approach demonstrated the importance and the strong influence of the contact angle and hysteresis. A small change of their value (staying in the uncertainty range of 5°) allowed to reach reasonable predictions over a large range of bubble departure diameters with the proposed model, using a reduced number of empirical parameters.

6.5 SLIDING PHASE

6.5.1 Modeling

After departure, bubbles slide over a distance l_{sl} which scales the impact of the sliding phenomenon over the wall heat transfer. Achieving good prediction of bubble sliding velocity is then important if one wishes

to correctly quantify its impact. Following the force balance framework presented in Section 6.2, we can write Newton's second law parallel to the wall for the sliding bubble.

$$\rho_V \frac{d(V_b U_b)}{dt} = -\pi R \sigma f_{C,x} + \frac{4}{3} \pi R^3 (\rho_L - \rho_V) g + \frac{1}{2} C_D \rho_L \pi R^2 U_L^2 + \frac{4}{3} \pi R^3 \rho_L \left[3C_{AM,x} \frac{\dot{R}}{R} U_{rel} - C_{AM,x} \frac{dU_b}{dt} \right] \quad (6.112)$$

This equation can be re-written to express the bubble acceleration.

$$\left(1 + \frac{\rho_L}{\rho_V} C_{AM,x} \right) \frac{dU_b}{dt} = \left(\frac{\rho_L}{\rho_V} - 1 \right) g + \frac{3}{8} \frac{C_D}{R} \frac{\rho_L}{\rho_V} (U_L - U_b) |U_L - U_b| + 3 \frac{\dot{R}}{R} \left[C_{AM,x} \frac{\rho_L}{\rho_V} (U_L - U_b) - U_b \right] - \frac{3}{4} \frac{\sigma}{\rho_V} \frac{f_{C,x}}{R^2} \quad (6.113)$$

Then, we numerically solve this equation from the moment when $R \geq R_d$ using a first order Euler scheme for a duration close to the experimental sliding time. To assess the validity of Eq 6.113, we modify the growth constant K in order to roughly match experimental radius measurements. The goal is to verify if the force balance allows a good prediction of bubble velocity provided a correct bubble growth. Next sections compare obtained results against low and high pressure data.

6.5.2 Low Pressure Sliding

Maity [86] provided simultaneous measurements of bubble radius and velocity over time in vertical boiling for three liquid mass fluxes near saturation conditions. The contact angles were kept the same as in 6.4.3 since Maity provided average values over the bubble lifetime.

Results are displayed on Figure 6.23. The model seems to fairly good predict bubble sliding velocity for the 3 cases. The moment of departure is a bit underestimated as previously observed (Figure 6.20).

The biggest discrepancy is observed for the case at $G_L = 143.8 \text{ kg/m}^2/\text{s}$. The slope of the velocity profile is close to the experiments, but the bubble reaches a nearly constant acceleration too rapidly which yields an approximately constant overestimation of 0.1 m/s.

The case with $G_L = 239.6 \text{ kg/m}^2/\text{s}$ is well predicted regarding the velocity. However, the growth profile was difficult to match since measurements exhibit significant changes in growth regime after departure, which is probably due to the bubble being large enough to be impacted by the bulk flow. We can note that values of K between 0.5 and 1 were used to better fit the bubble radius time profile.

Regarding the relative velocity between the bubble and the surrounding liquid, the ratio $\frac{U_b}{U_L}$ greatly overcomes 1 which means the bubble slides much faster than the liquid. This is a consequence of both the low values of G_L along with the large bubble sizes inducing a great acceleration by the buoyancy force.

6.5.3 High Pressure Sliding

In his work, Kossolapov [72] conducted measurements of radius and sliding length over thousands of individual bubbles and then provided the associated statistical distributions. To compare our model with his measurements, we took the upper and lower bounds of R and l_{sl} over time and plotted the associated bands of measured values as shown on Figure 6.24 and 6.25.

Comparisons were done for cases at 20 bar and 40 bar and 3 different values of G_L . The value of $d\theta$ for the simulations was kept really small (2° at 20 bar and 0.5° at 40 bar) since bubble tilt is supposed to reduce during sliding because the relative velocity regarding the liquid flow is diminishing. Moreover, higher pressure means smaller bubbles that are even more unlikely to present a significant contact angle hysteresis. We also want to mention that neglecting the capillary term in Eq. 6.113 had a minor impact over the results except that the bubble accelerates a little bit faster.

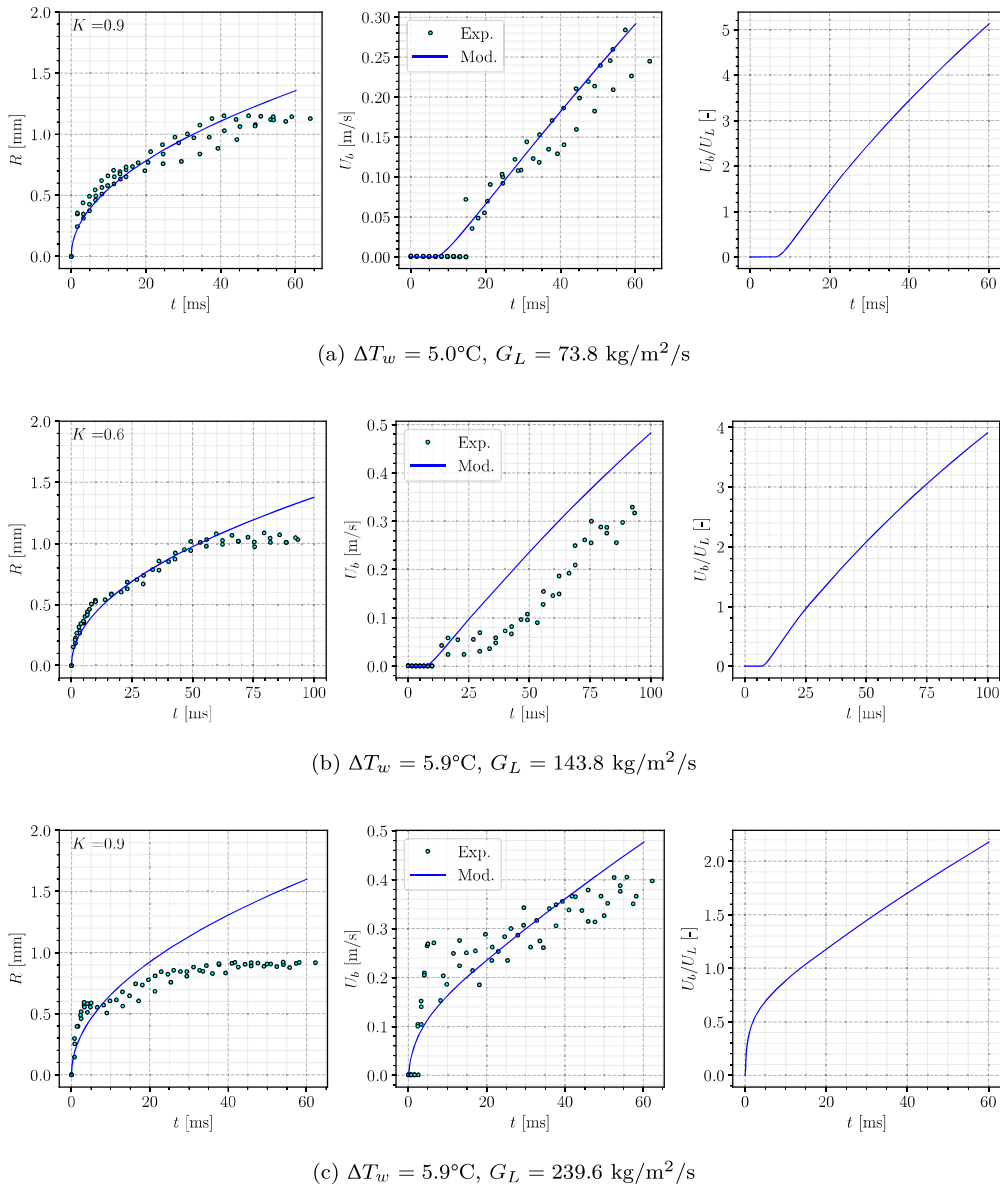


Figure 6.23: Bubble sliding velocity predictions on Maity cases

The obtained results are in good agreement with the sliding length profile vs. time, which means bubble sliding velocity is well predicted for those cases. Values of K between 0.8 and 2 were needed to match the bubble radius measurements.

We see that bubbles are rapidly reaching sliding velocities between 80% and 95% of the local liquid velocity. Only the 20 bar case at $G_L = 500 \text{ kg/m}^2/\text{s}$ where the bubble departs slightly later, reaching approximately 55% of the liquid velocity.

6.5.4 Comparison of Forces in Sliding Stage

In order to identify the main accelerating forces, we compare the amplitude of the forces during the sliding phase for one low pressure case of Maity and one high pressure case of Kossolapov (Figure 6.26).

It appears that at high pressure and liquid velocity, the drag force is the main driving force and stays positive since the bubble do not slide faster than the rapid surrounding liquid (reaching approximately 80% of the local liquid velocity). On the other hand, larger bubbles observed at low pressure and liquid velocity are accelerated by buoyancy due to their larger volume, with a nearly negligible Drag force. In both cases, the added mass force can not be neglected especially when bubble velocity rises by limiting its

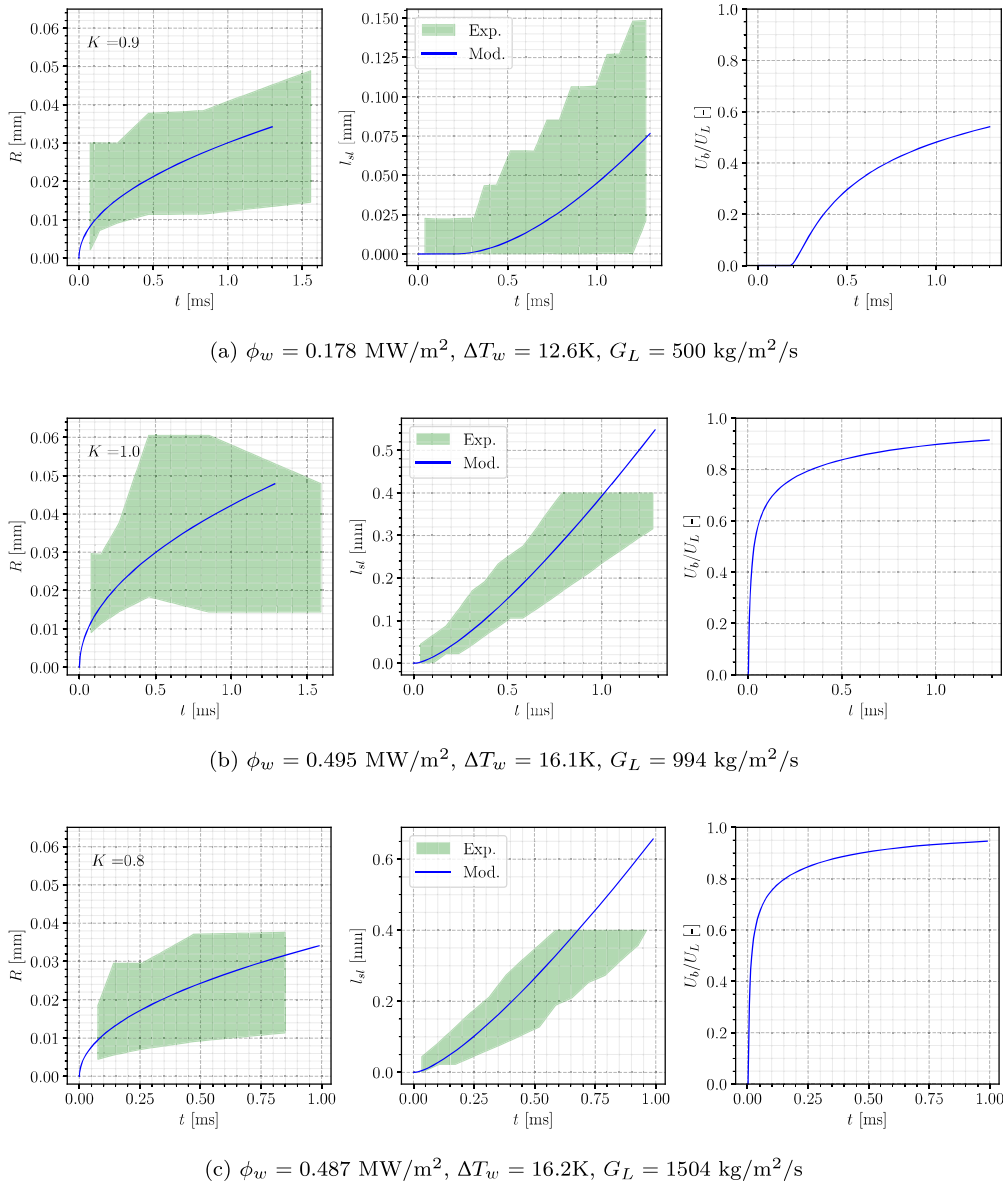


Figure 6.24: Bubble sliding length predictions on Kossolapov cases - $P = 20$ bar

acceleration induced by the larger force (buoyancy or drag in the presented cases). This further emphasizes the importance of a proper derivation of the added mass force regardless of the boiling conditions. The capillary force seem to be a limited but constant slowing term in both cases. Finally, the amplitude of the forces involved can span from roughly $10 \times 10^{-4} \text{ N}$ at low pressure (much greater than the rate of change of bubble momentum laying around 10^{-9} N) down to a few nN at higher pressure (same order of magnitude as the rate of change of bubble momentum), especially due to the bubble size.

This comparison highlights the fact that the proposed model is able to represent different forces hierarchy depending on the flow conditions and to acceptably predict the associated bubble sliding velocity, which is an encouraging point regarding its generality.

6.6 BUBBLE LIFT-OFF

6.6.1 Introduction

The question of lift-off for a single bubble in vertical boiling is trickier than for horizontal boiling. Indeed, in horizontal boiling, lift-off is ensured thanks to the buoyancy force that will continuously increase as

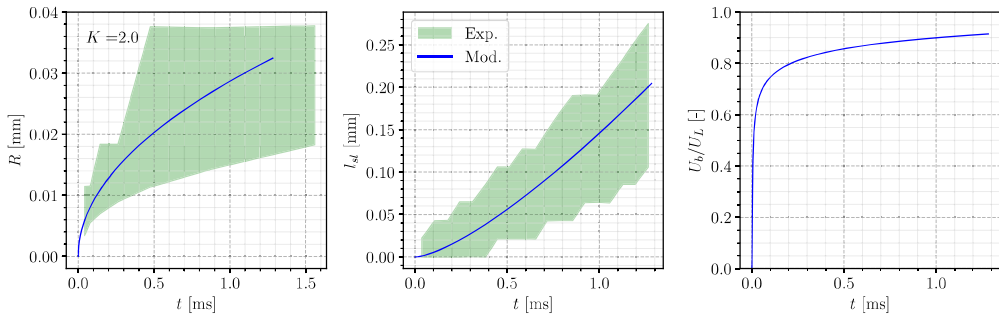
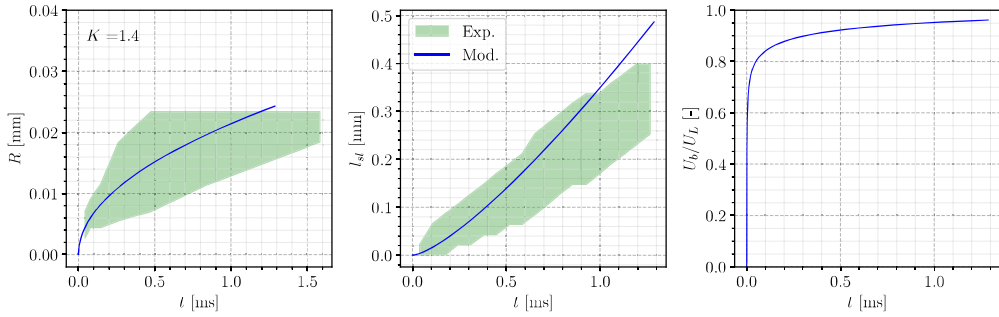
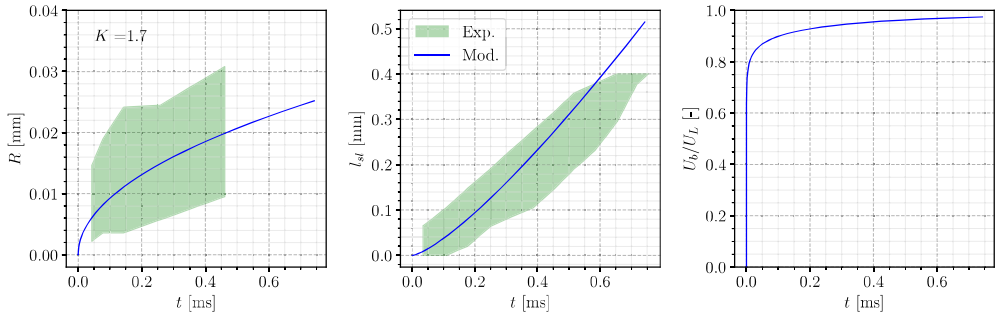
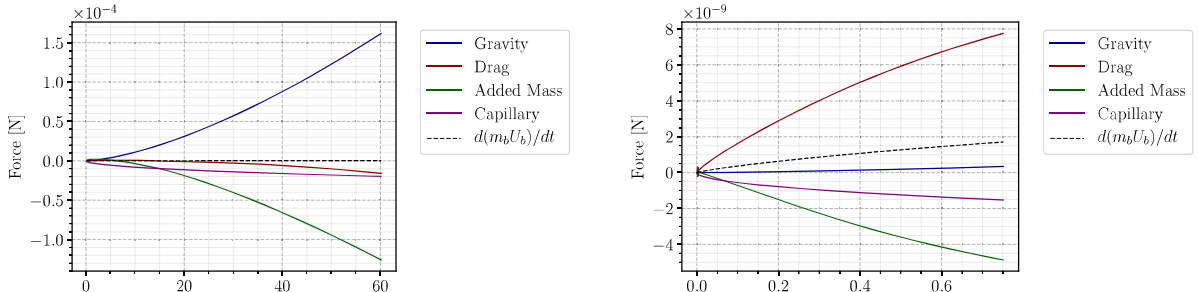
(a) $\phi_w = 0.291 \text{ MW/m}^2, \Delta T_w = 10.1\text{K}, G_L = 500 \text{ kg/m}^2/\text{s}$ (b) $\phi_w = 0.361 \text{ MW/m}^2, \Delta T_w = 10.8\text{K}, G_L = 994 \text{ kg/m}^2/\text{s}$ (c) $\phi_w = 0.613 \text{ MW/m}^2, \Delta T_w = 12.2\text{K}, G_L = 1504 \text{ kg/m}^2/\text{s}$ Figure 6.25: Bubble sliding length predictions on Kossolapov cases - $P = 40$ bar(a) Maity : $\Delta T_w = 5.9^\circ \text{C}, G_L = 239.6 \text{ kg/m}^2/\text{s}$ (b) Kossolapov : $P = 40 \text{ bar}, \phi_w = 0.613 \text{ MW/m}^2, G_L = 1504 \text{ kg/m}^2/\text{s}$

Figure 6.26: Amplitude of each force during sliding

the bubble grows. It can also be promoted by the lift force if the bubble slides slower than the liquid. This facilitates the identification of the moment when bubble leaves the surface (Figure 6.27).

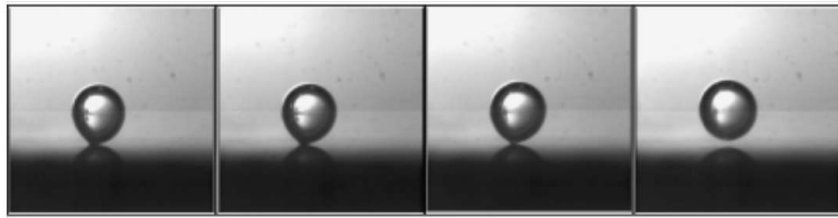
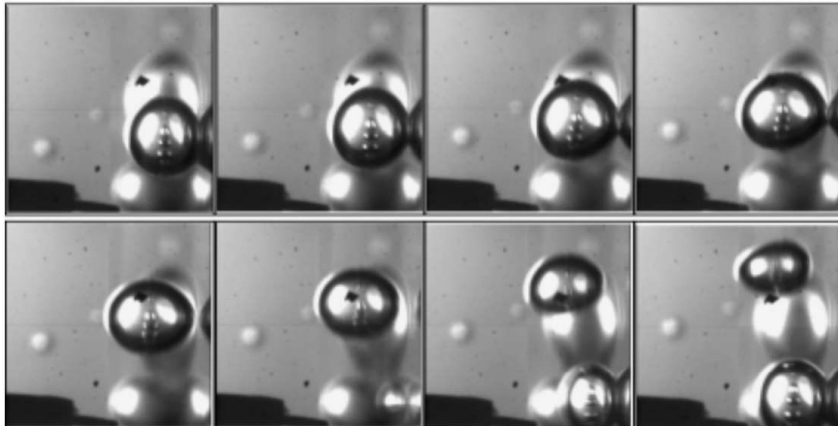


Figure 6.27: Visualization of bubble lift-off in horizontal boiling conducted by and adapted from Maity [86]. The detachment of the bubble base from the surface is clear in the last frame.

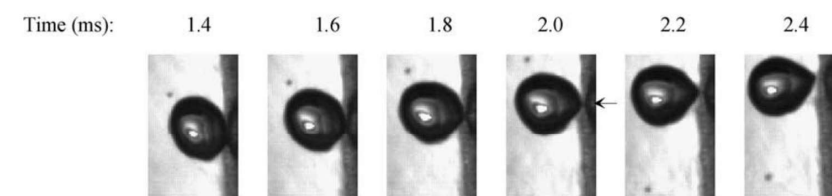
However, in vertical boiling, the lift-off from the surface only results from the competition between the added mass force and lift force (capillary force and contact pressure compensating each other for a truncated sphere). The added mass force keeps the bubble attached and the lift force which can either promote lift-off or push the bubble against the wall depending on the value of the lift coefficient C_L . As seen in Subsection 6.2.5, the lift coefficient can become negative when reaching negative relative velocity U_{rel} , yielding negative non-dimensional shear rates Sr in Eq. 6.43. In this case, the force balance perpendicular to the wall (Eq. 6.69) will never become positive and thus never predict bubble lift-off using criterion based on the force balance sign.

In addition, those two forces are difficult to precisely evaluate since they rely on complex phenomena such as the bubble growth (R , \dot{R} , \ddot{R}) and the fine hydrodynamics of a bubble attached to a wall. A small error on the evaluation of one of those forces can therefore lead to erroneous predictions of the lift-off phenomenon.

On the experimental side, different behavior for boiling bubbles in vertical boiling have been observed. Single bubble experiments such as those of Maity [86] and Situ *et al.* [117] observed bubble lift-off for single bubble at atmospheric pressure as shown on Figure 6.28.



(a) Lift-off observed in Maity experiment [86]



Diameter (mm): 0.574 0.588 0.609 0.617 0.615 0.605

(b) Lift-off observed in Situ experiment [117]

Figure 6.28: Visualization of bubble lift-off in vertical boiling. The moment when bubble leaves the surface appears less clearly than for horizontal boiling.

Although bubble lift-off is observed for those single bubble cases, the exact moment of lift-off is complicated to identify since the bubbles sometimes stay very close to the wall and can even re-attach to the wall, presenting a bouncing motion while moving close to the wall as in Yoo *et al.* [137].

Contrary to those observations, other authors who realized experimental visualizations of vertical flow boiling of surfaces with numerous bubbles saw that single bubbles did not leave the wall by themselves. For instance, Scheiff [114] observed different possible behaviors in highly subcooled liquid:

- Bubble growth up to an equilibrium diameter while sliding on the wall and keeping the same size.
- Rapid sudden growth of bubbles can enlarge them up to the subcooled liquid, yielding to condensation while sliding on the wall.
- Bubble lift-off under application of a high heat flux (rapid growth) or after coalescence with another bubble on its path.

Similar behaviors of bubbles sliding along the wall and not leaving it until a coalescence occurs have also been reported for vertical flow boiling by Prodanovic *et al.* [103] or Thorncroft *et al.* [125]. In particular, Prodanovic *et al.* mentioned that bubbles that would detach from the wall by themselves cannot be interpreted as typical bubble behavior in those conditions since there were very few of them. Typical experimental visualizations of this nature are presented on Figure 6.29

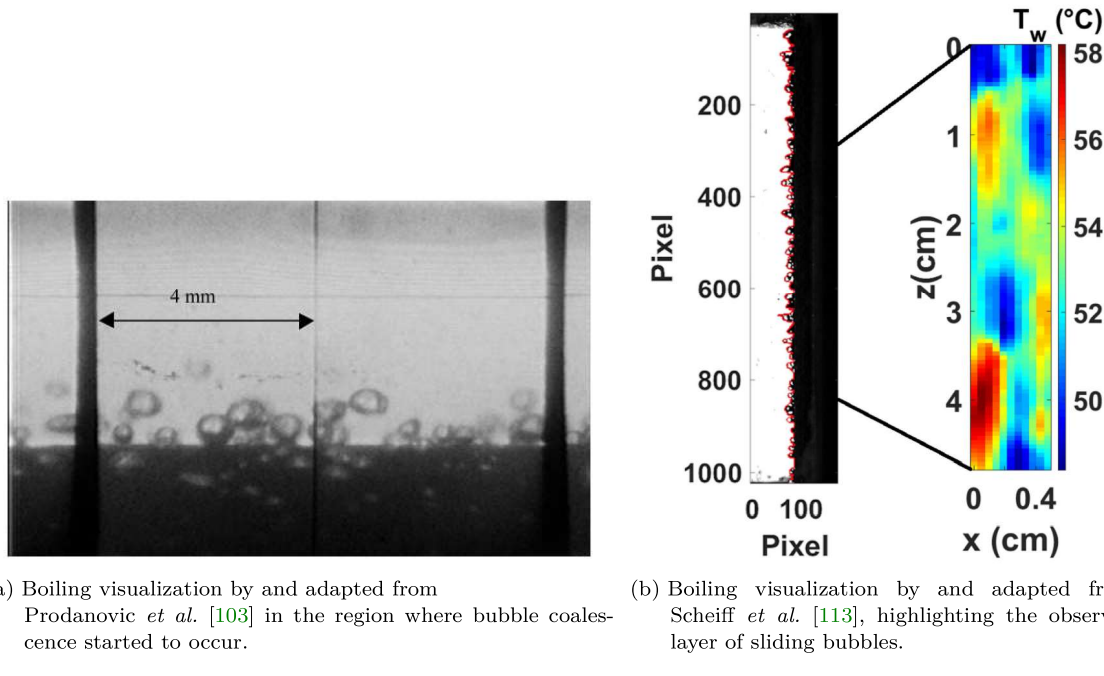


Figure 6.29: Visualization of boiling surfaces in vertical boiling, where single bubble lift-off is not systematically observed.

Generally speaking, it seems that single bubbles in vertical boiling are not likely to present a lift-off behavior by themselves in every flow conditions that could be explored. As concluded by Okawa *et al.* [99] and discussed in Yoo *et al.* [137], it seems that a more general trigger for bubble lift-off would be either associated to strong deformation / elongation of the bubble shape (inducing a change in the lift coefficient) or to a coalescence event between two bubbles.

Note : Such a lift-off mechanism is considered by Gilman & Baglietto [47] who consider lift-off when the Eotvos number of the bubble reaches 0.1.

To further discuss this question, we will nevertheless try to consider the bubble lift-off as a single event and therefore try to attribute a given lift-off diameter D_{lo} based on available experimental measurements.

6.6.2 Experimental Measurements of Lift-Off Diameter

Observations and measurements of bubble diameter in various flow conditions have been conducted by numerous authors since the middle of the XXth century. Although recent experimental techniques allow to identify the moment at which bubble diameter is measured (departure from nucleation site, lift-off, etc.), older experiments could not ensure the nature of the bubbles that were observed.

For instance, the work of Ünal [149] measured the maximum bubble diameter and used other experimental results (Gunther [55], Griffith [49], Treshchев [129] and Tolubinsky [127]) to build a correlation. However, it can not be clearly stated that those measurements were single bubbles lifting off the surface or bubbles resulting of coalescence.

Remark : As explained by Ünal, their measurements (detailed in De Munk [98]) are based on enlarged photographic observations of the bubble population near the boiling surface from which they extracted the maximum diameter, meaning there is no evidence that it was actually a lift-off diameter of a single bubble.

This was also pointed out by Kossolapov [72] who showed that at very high pressure, old measurements of bubble diameter were larger for flow boiling compared to pool boiling, which is intuitively unphysical. This could be explained as mentioned above if those measurements were actually coalesced bubbles which would naturally exhibit larger diameters than single bubbles at lift-off.

However, those measurements can still be interesting since their evolution with the operating conditions should present trends similar to single bubble experiments. To do so, we gathered several experimental data sets of maximum / lift-off diameter from the literature for vertical subcooled flow boiling of water. The experimental conditions of the data set are presented on Table 6.5.

6.6.3 Influence of the Flow Boiling Conditions

To evaluate the influence of the flow boiling conditions over the various experimental measurements, we have represented the values of the non-dimensional lift-off diameter $\frac{D_{lo}}{L_c}$ (L_c is the capillary length) versus 6 dimensionless flow parameters:

- The reduced Jakob numbers of superheat and subcooling Ja_w^* and Ja_L^* . With $Ja^* = \frac{c_{p,L}\Delta T}{h_{LV}}$ which excludes the impact of pressure through the density ratio.
- The density ratio $\rho^* = \frac{\rho_L}{\rho_V}$, scaling the operating pressure.
- The saturated liquid Prandtl number Pr_L , quantifying the liquid thermal properties.
- The local wall Reynolds number $Re_\tau = \frac{\rho_L U_\tau L_c}{\mu_L}$, evaluating the impact of the liquid flow, with U_τ the shear friction velocity as in Eq. 6.72.
- The capillary number Ca which can be related to bubble deformability under viscous effects.

The results are presented on Figure 6.30.

The experimental values of $\frac{D_{lo}}{L_c}$ display the following trends:

- Increase with Ja_w^* ;
- Decrease with Ja_L^* ;
- Increase with ρ^* ;
- Increase with Pr_L ;
- Decrease with Re_τ and Ca .

Author	Fluid	D_h [mm]	P [bar]	G_L [kg/m ² /s]	ΔT_L [K]	ϕ_w [kW/m ²]	ΔT_w [K]	D_{lo} [mm] (N_{mes})
Gunther [55] (1951)	Water	6.92	1 - 1.7	1492 - 6070	33 - 86	2.3 - 10.64	N.A.	0.32 - 1.02 (12)
Griffith [49] (1958)	Water	12.7	34.5 - 103	4651 - 7593	11 - 80	3.25 - 8.53	N.A.	0.081 - 0.146 (6)
Treshchev [129] (1969)	Water	10.18	5 - 50	1643 - 1789	30 - 62	1.4 - 2.9	N.A.	0.12 - 0.26 (3)
Tolubinsky [127] (1970)	Water	10	1 - 10	72.6 - 198.4	5 - 60	0.47	N.A.	0.19 - 1.24 (9)
Ünal [149] (1976)	Water	8	139 - 177	2082 - 2171	3 - 5.9	0.38 - 0.55	N.A.	0.11 - 0.18 (7)
Maity [86] (2000)	Water	20	1.01	0 - 239.6	0.3 - 0.7	N.A.	5 - 5.9	1.8 - 2.4 (4)
Prodanovic [103] (2002)	Water	9.3	1.01 - 3	76.7 - 815.8	10 - 60	0.1 - 1.2	N.A.	0.366 - 2.68 (44)
Situ [117] (2005)	Water	19.1	1.01	471.8 - 910.8	1.5 - 20	0.06 - 0.2	N.A.	0.145 - 0.605 (90)
Chu [13] (2010)	Water	22.25	1.45	301 - 702	3.4 - 22.6	0.135 - 0.201	N.A.	0.51 - 1.71 (14)
Ahmadi [1] (2012)	Water	13.3	0.96 - 1.13	169 - 497	8.4 - 20.6	0.16 - 0.318	11.4 - 18.4	0.12 - 3.9 (13)
Okawa [100] (2018)	Water	14	1.27 - 1.86	252 - 490	10 - 39	0.161 - 0.487	N.A.	0.64 - 0.188 (10)

Table 6.5: Bubble lift-off diameters data sets in vertical flow boiling

A great range of D_{lo} values at low pressure (for which we have the larger number of measurements) are reached in the experiments. This further indicates the complicated behavior of bubble lift-off, for which similar flow conditions can lead to very different bubble diameters.

Remark : This variation could be associated to the heater material and surface morphology, which are not quantified here.

Moreover, we can observe that measurements from Ünal do not follow the general tendency of other data as on Figure 6.30c, with values of D_{lo}/L_c above the trend, further supporting the assumption that those experimental values were actually those of coalesced bubbles.

6.6.4 Predicting the Lift-Off with a Force Balance

As previously discussed, the prediction of the lift-off using the force balance perpendicular to the wall (Eq. 6.69) is complicated because:

- The spherical shape without tilt ($d\theta = 0$) leads to exact compensation between contact pressure force and capillary force. Leaving only the added mass force and lift force to predict the lift-off.
- Those two forces can both be directed towards the wall depending on the flow conditions, making it impossible for a single bubble to lift-off by itself.
- The estimation of those forces rely on complicated description of thermal and hydrodynamic phenomena, making any uncertainty a source of large errors on lift-off prediction.

This difficulty has already been pointed out by Montout [97] who faced difficulties in consistently using the force balance perpendicular to the wall for bubble lift-off. Depending on the flow conditions, the force

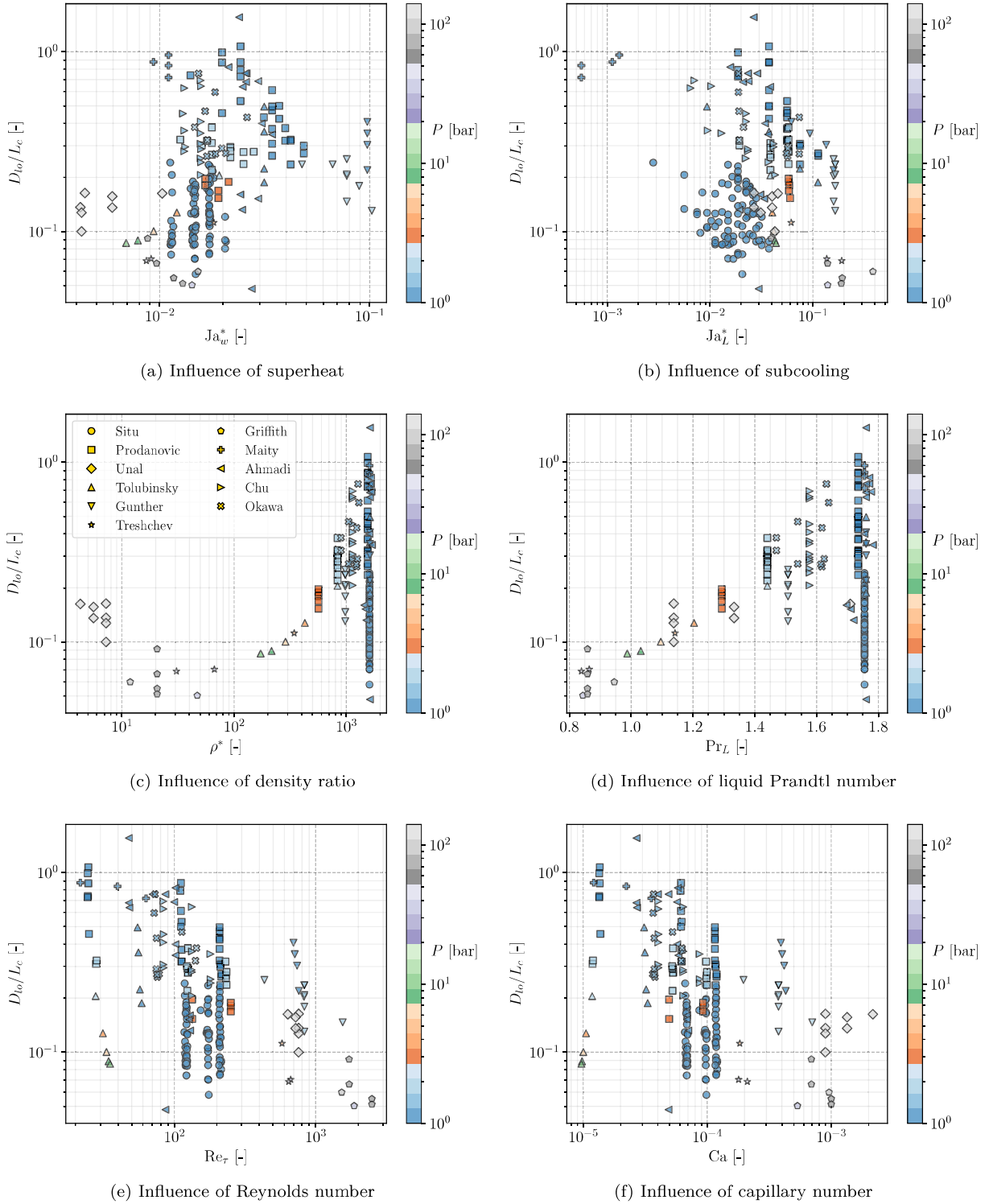


Figure 6.30: Evolution of D_{lo}/L_c depending on the flow conditions.

balance would sometimes predict an immediate lift-off right after or even before departure by sliding, which is in contradiction with aforementioned experimental observation.

Following a similar approach to the departure diameter (Section 6.4), we can rearrange Eq. 6.69 into the following non-dimensional force balance perpendicular to the wall, supposing that $U_{b,y} = \dot{R}$:

$$\underbrace{\rho^* \left(\frac{C_L}{8} + \frac{C_{AM,y3}}{3} \right)}_{\text{Promotes lift-off}} - \underbrace{\frac{1}{3} \left[\rho^* (2C_{AM,y1} + C_{AM,y2}) + \frac{2}{3} \right] \left(\frac{K^2 \text{Ja}_w^2}{\text{Pr}_L \text{Re}_b} \right)^2}_{\text{Hinders lift-off}} > 0 \quad (6.114)$$

This formulation sums up the competition between the lift-off promoted by the first term on the LHS combining effect of the lift force and the added mass force due to the external flow versus the growth terms that will hinder the lift-off by pushing the bubble against the wall.

Remark : Eq. 6.114 mathematical formulation present some coherent trend with physical observations:

- The hindering term will increase with bubble growth rate (*i.e.* Ja_w increase) thus increasing R_{lo} ;
- The hindering term will reduce with the liquid velocity (*i.e.* Re_τ or Re_b increase), thus reducing R_{lo} .

Other influence of the flow parameters are less directly possible to anticipate.

The solving of the equation of bubble departure (Eq. 6.105) and sliding (Eq. 6.113) while checking when Eq. 6.114 detects lift-off can be performed to estimate the lift-off diameter D_{lo} . Applied over the experimental database of Table 6.5, this yields the predictions of Figure 6.31.

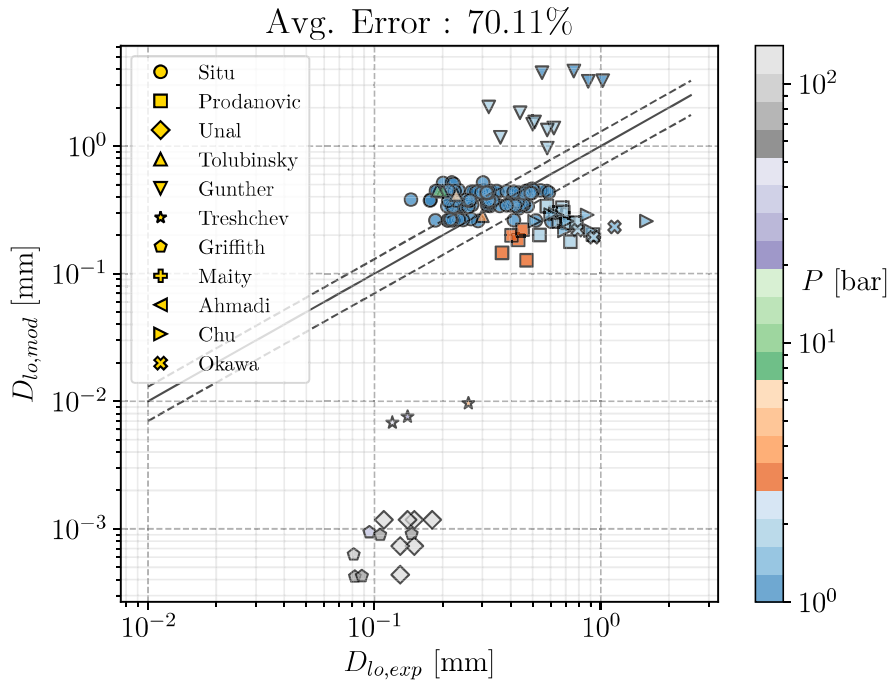


Figure 6.31: Prediction of Eq. 6.114 versus data from Table 6.5. Value of $K = 0.24$ was used and only converged points are presented, same generic value used in Figure 6.22.

First, it is important to note that among every experimental data used for comparisons, many points did not converge to a lift-off diameter value, Eq. 6.114 failing to become positive at any moment of the simulated bubble lifetime. As a consequence, 61 measurements (27 from Prodanovic, 5 from Tolubinsky, 3 from Maity, 13 from Ahmadi, 6 from Chu, 7 from Okawa) out of 211 could not be compared to the force balance approach.

For the converged cases, this yields an acceptable order of magnitude at low pressure especially for Situ data. On the contrary, high pressure measurements are greatly underestimated with lift-off diameters lower than $1\mu\text{m}$.

At last, even though the force-balance approach presents many interests for modeling grounds, its application to lift-off prediction in vertical boiling seems a bit tricky contrary to the departure by sliding. The sole competition based on fine hydrodynamics (lift and added mass) and the bubble growth (for which a proper complete modeling is still unavailable) makes it a very complicated solution to address the lift-off diameter estimation problem.

6.6.5 A Simple Non-Dimensional Correlation

Alternatively, in case it would prove to be necessary to define a lift-off diameter value for the HFP model, we propose a simple direct correlation based on non-dimensional parameters characterizing the boiling conditions. We chose to model the value of the non-dimensional lift-off diameter D_{lo}/L_c using the liquid Prandtl number Pr_L at saturation, the density ratio $\rho^* = \rho_L/\rho_V$, the reduced Jakob numbers Ja_w^* and Ja_L^* and the wall Reynolds number Re_τ . Using the `sklearn` module to estimate the value of the coefficient for the multilinear regression over the data of Table 6.5 yields:

$$\frac{D_{lo}}{L_c} = e^{8.43\text{Pr}_L^{-0.005}} \left(\frac{\rho_L}{\rho_V} \right)^{-0.36} \text{Ja}_w^{*1.15} (1 + \text{Ja}_L)^{-6.68} (1 + \text{Re}_\tau)^{-0.53} \quad (6.115)$$

We chose to correlate $(1 + \text{Ja}_L)$ and $(1 + \text{Re}_\tau)$ so that the formulation degenerates those terms to 1 for saturated and pool boiling conditions. This simple care is often forgotten in similar approaches [71, 144] where the resulting correlations either diverges or tend to 0 when reaching those conditions.

The correlation is compared to Kommajosyula's correlation [71] on Figure 6.32.

The proposed formulation, though simple, allows to reach an average error of approximately 45% over the whole data set versus approximately 94% of error for Kommajosyula's formulation. Even if the approach may lack of detailed physical modeling, it seems appropriate to obtain an acceptable order of magnitude of the lift-off (or maximum observed) bubble diameter over various flow conditions including high pressure.

Remark : The use of Re_τ instead of the bulk liquid velocity of Reynolds number allows the correlation to be more easily applied in CFD computations where obtaining bulk quantities from wall cells can be tricky depending on the geometry.

6.6.6 Conclusion on the Lift-Off

As discussed in this section, the question of the bubble lift-off in vertical flow boiling is very complicated and can not be answered in a straightforward way. First, we saw that the lift-off is not always observed for individual bubbles that can slide for a very long time before leaving the surface as a result of a coalescence by colliding with an other bubble. This difficulty was also experienced when using the force-balance approach to predict the lift-off diameter, with bubble lifetime and sliding simulations that would not converge, *i. e.* yield a positive force balance perpendicular to the wall that would detach the bubble.

Moreover, existing database, though diverse, are lacking of high pressure measurements using recent experimental techniques. The existing high-pressure data present a qualitative uncertainty regarding the nature of the measured bubbles that can result of coalescence events.

Finally, the question of lift-off in the framework of the HFP model can be answered in three ways:

- 1) No lift-off diameter value is attributed to single bubbles. It is thus computed by solving the bubble sliding until it collides and coalesces with an other bubble growing on its nucleation site. This approach is likely to be the most representative of the general behavior of bubbles in vertical boiling according to experiments. However, it may lead to very large, if not unphysical, values of sliding length at low heat fluxes values where the average distance between bubbles would increase greatly.
- 2) Same as above 1) but the lift-off is considered when a non-dimensional number representative of bubble deformation reaches a critical value. Several bubble coalescence can thus occur until that moment occurs.

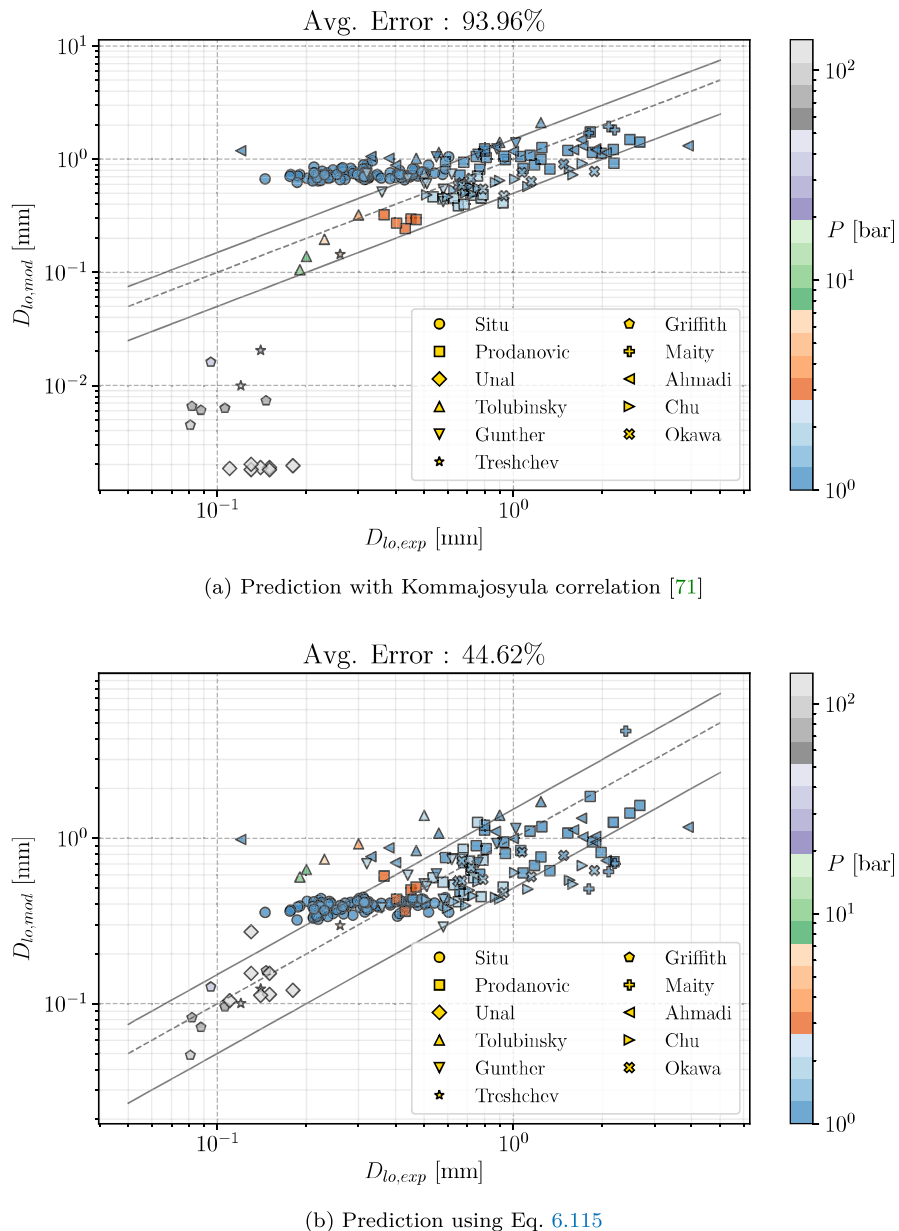


Figure 6.32: Comparison of simple direct correlations with data from Table 6.5

- 3) A lift-off / maximum diameter is attributed for single bubble behaviors and sliding is computed between the fixed values of D_d and D_{lo} , with coalescence that can be considered between those two events and trigger earlier lift-off. This choice would be in fewer concordance with experimental observations but would allow to consider distinct bubble lifetime scenario including full single bubbles.

6.7 CONCLUSION

In this chapter, we discussed the different aspects of boiling bubble dynamics in vertical flow boiling. This is a pivotal aspect of the HFP to reach modeling representative of the boiling phenomenon. However, the great variety of both experimental observations and existing models demonstrate the high complexity of the physics at stake here. At last, we can conclude that:

- The problem of bubble growth in complicated conditions (external flow, subcooling, wall presence) remains an open question that could benefit from new experimental insights trying to account for those effects. A new model based on simple heat diffusion accounting for subcooling was proposed and could achieve better predictions compared to traditional model when using a correct value of the thermal boundary layer thickness δ . However, a general precise estimation of δ is complicated

and simpler model of the form $R = KJa_w\sqrt{\eta_L t}$ can also propose reasonable predictions provided an optimal choice of K .

- Modeling the bubble dynamics through a force balance faces modeling uncertainties that still have to be leveraged, especially regarding wall-related effects (contact angle, thermal properties, etc.). Nonetheless, the development of a simpler force balance with less empiricism and enhanced forces expressions allowed to reach acceptable predictions of the departure by sliding diameter D_d over a large database in vertical boiling.
- The same force balance was also able to propose good estimations of the bubble sliding velocity along the wall, both at low and high pressure.
- A similar approach was more complicated to apply for lift-off predictions due to the high sensitivity of the force balance perpendicular to the wall. Moreover, single bubble lift-off can not be considered as a general bubble behavior in vertical boiling according to many experimental observations.
- The many different correlations for bubble dynamics predictions are tied to their establishment range and can lack of generality or present undesirable mathematical behavior (*e. g.* divergence or tending to 0 in pool boiling or saturated conditions). A direct correlation was proposed to estimate the bubble lift-off diameter (or maximum bubble diameter for a single bubble) based on a large experimental database in vertical boiling. The simple use of terms in the form $(1 + Ja_L^*)^a$ and $(1 + Re_\tau)^b$ that degenerates to 1 in pool or saturated boiling allow the correlation to be applied in any flow conditions.

7

CLOSURE LAWS AND CONSTRUCTION OF A NEW HEAT FLUX PARTITIONING MODEL

Contents

7.1	Introduction	113
7.2	Single-Phase Heat Transfer Coefficient	114
7.3	Nucleation Site Density	116
7.3.1	Existing Correlations	117
7.3.2	Comparison with Experimental Measurements	119
7.4	Growth time	120
7.5	Waiting Time	121
7.5.1	Existing Models	121
7.5.2	Experimental Measurements	123
7.5.3	Evaluation of the Models	124
7.6	Considerations on Bubble Interactions and Nucleation Sites Deactivation	126
7.6.1	Nucleation Site Distribution	126
7.6.2	Static Deactivation	128
7.6.3	Static Coalescence	129
7.6.4	Sliding Coalescence	130
7.7	Bubble Sliding Length	131
7.8	Single Bubble Quenching Area	133
7.9	Assembling a New Heat Flux Partitioning	134
7.9.1	Liquid Convective Heat Flux	134
7.9.2	Static Coalescence Evaporation Heat Flux	135
7.9.3	Sliding Coalescence Evaporation Heat Flux	135
7.9.4	Quenching Heat Flux	135
7.9.5	Vapor Convective Heat Flux	136
7.9.6	Liquid Convection Area	136
7.9.7	Model Summary	136
7.10	Conclusion	139

7.1 INTRODUCTION

When constructing a Heat Flux Partitioning model, different modeling steps have to be followed:

- Definition of the heat transfer mechanisms to be accounted for ;
- Identification of the physical parameters requiring a specific computation ;
- Conduct analytic approaches or correlation selection to choose dedicated closure laws.

In this work, we want to account for four different heat fluxes:

- The liquid convective heat-flux :
- The evaporation heat flux ;
- The transient conduction / quenching heat flux including the impact of sliding bubbles ;

- The vapor convective heat flux located at dry spot locations beneath bubble footprints.

The evaluation of those different heat fluxes requires to model a certain number of parameters, namely:

- The single-phase heat transfer coefficient toward the liquid phase $h_{c,L}$;
- The nucleation site density N_{sit} , representing the number of cavities per unit of area where bubbles will be allowed to nucleate ;
- The different times involved in the bubble nucleation cycle, *i.e.* the growth time until bubble departure by sliding $t_{g,d}$ and the waiting time between two nucleation events on a site t_w ;
- The bubble dynamics at the wall, including bubble departure radius R_d , sliding velocity U_b , lift-off (discussed in Chapter 6), sliding length l_{sl} and area $A_{q,1b}$;
- Possible interactions between bubbles (coalescence) or nucleation sites (deactivation).

In this Chapter, we will go through each physical parameter and discuss their modeling in the light of experimental measurements when possible. Finally, a new model formulation for the Heat Flux Partitioning is proposed in Section 7.9.

7.2 SINGLE-PHASE HEAT TRANSFER COEFFICIENT

The choice of a proper correlation to compute the single-phase heat transfer coefficient is a first but unavoidable step to build a HFP model. Indeed, if the single-phase convection term is badly computed, the resulting boiling model will fail to predict the wall temperature. For instance, if the liquid convective HTC is overestimated, it would result in a delayed increase of the boiling and quenching heat fluxes which would in turn lead to an overprediction of the wall temperature.

To assess existing correlations for the single-phase HTC, we will use wall temperature measurements extracted from experimental boiling curves for water where $T_w \leq T_{sat}$. They correspond to the single-phase part of the experimental data later used to assess the HFP model. As discussed before, good prediction of the single-phase HTC is very important in the frame of boiling heat transfer, which means achieving good wall temperature predictions prior to the Onset of Nucleate Boiling. The chosen data are presented on Table 7.1.

Author	D_h [mm]	P [bar]	G_L [kg/m ² /s]	ΔT_L [K]	ϕ_w [MW/m ²]	$T_{sat} - T_w$ [K]	N_{mes} [-]
Kossolapov [72] (2021)	12	10.5	500 - 2000	10	0.1 - 0.6	0.22 - 9.5	12
Richenderfer [108] (2018)	15	1 - 5	1000 - 2000	10-20	0.1 - 0.63	1 - 18.7	13
Jens-Lottes [61] (1951)	5.74	137.9	2617.5	53.3 - 92.2	0.91 - 2.37	0.33 - 44.1	15
Kennel [65] (1948)	4.3 - 13.2	2 - 6.2	284 - 10 577	11.1 - 83.3	0.035 - 1.89	0.35 - 69	52

Table 7.1: Experimental data range of wall temperature measurements from the single-phase part of boiling curves. N_{mes} is the number of measurements of each data set.

On Figure 7.1, we compare the results of wall temperature prediction in the single-phase region obtained with the correlation of Dittus-Boelter (Eq. 3.20) and Gnielinski (Eq. 3.21).

Note : The Gnielinski correlation is used in Kommajosyula's HFP model to compute the liquid heat transfer coefficient.

The two correlations are of similar efficiency regarding wall temperature predictions over the considered data sets. They both have very good agreement with Kennel data and clear overestimations of ΔT_w on Richenderfer and Kossolapov measurements. The slope difference compared to the parity implies that the correlations are predicting too small Nusselt numbers for those cases. Regarding Jens-Lottes data, both models underestimate the wall temperatures, with better results achieved by Gnielinski correlation.

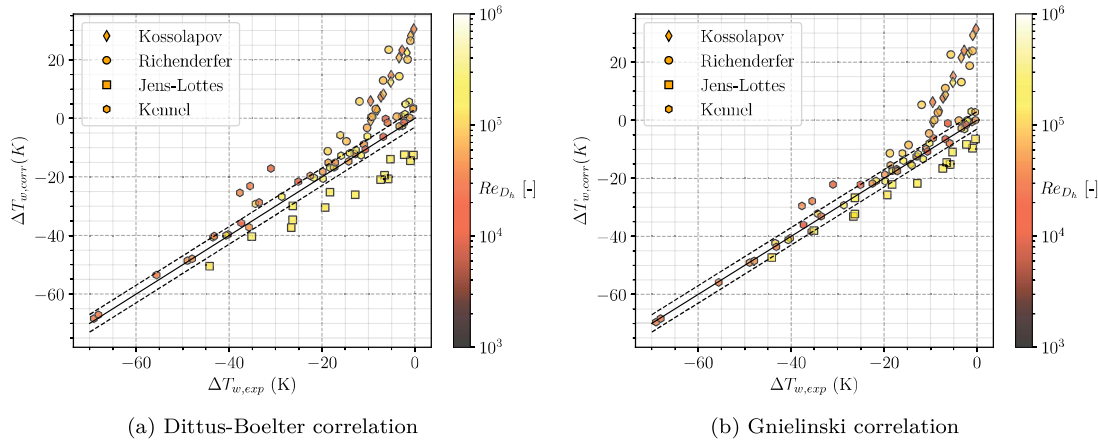


Figure 7.1: Predictive capability of wall temperature by single-phase heat transfer correlations. $\pm 3K$ error bars indicated.

Remark : We tested different friction factor along with different values of wall roughness in the Gnielinski correlation and observed a negligible impact on the overall results. This allows to stay with a simple formulation for the friction coefficient.

The error obtained on Richenderfer and Kossolapov data can be explained by the definition of the HTC computed by Gnielinski correlation. Indeed, Gnielinski correlated a Nusselt number associated to a forced convection coefficient $h_{fc,Gniel}$ in the case of an internal flow with a completely heated wall. However, only one side of the channel is heated in Richenderfer and Kossolapov experiments. If S_{heat} denotes this actual heated surface, then Gnielinski correlation estimates the HTC for a surface $4S_{heat}$. With the same imposed total heat power Φ_w and bulk liquid temperature T_L , we have:

$$h_{fc,Gniel} = \frac{\Phi_w}{(T_{w,Gniel} - T_L) 4S_{heat}} \quad (7.1)$$

$$h_{fc,exp} = \frac{\Phi_w}{(T_{w,exp} - T_L) S_{heat}} \quad (7.2)$$

Writing $T_{w,Gniel} = T_{w,real}$ then yields:

$$h_{fc,exp} = 4h_{fc,Gniel} \quad (7.3)$$

Remark : This correction can be interpreted as using the thermal diameter instead of the hydraulic diameter, which is 4 times smaller when only one side of the channel is heated.

On Figure 7.2 we display the predictions of Gnielinski correlation including this correction by a factor 4 on the HTC for Richenderfer and Kossolapov cases. On the same Figure, we also present predictions achieved with the local HTC estimation implemented in NCFD (Eq. 2.35), using a value of $y^+ = 100$.

The NCFD approach yields predictions similar to the 1D correlations (Figure 7.1) with larger underestimations on Jens-Lottes measurements, confirming its correct behavior for single-phase flows as observed on DEBORA simulations (Chapter 4). On the other hand, we see that applying a constant correction to the Gnielinski correlation (4 for Kossolapov and Richenderfer cases) suffices to yield accurate predictions on the whole range of wall temperature measurements.

Remark : The NCFD law was tested without running CFD simulations. Eq. 2.33 was re-written in python to allow its testing outside of the whole code. The use of $y^+ = 100$ as well as the Mac Adams correlation (Eq. 6.72) for the friction velocity U_τ may induce a difference with the predictions that could be achieved by running a complete CFD computation of the considered cases.

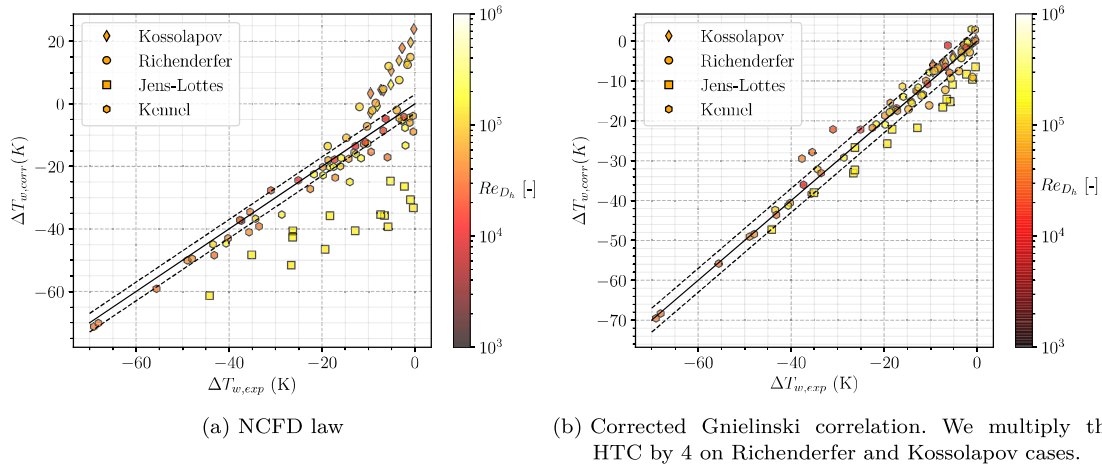


Figure 7.2: Predictive capability of wall temperature by NCFD law and Gnielinski correlation including corrections. $\pm 3K$ error bars indicated (dashed lines).

The average errors obtained with each model are summed up on Table 7.2

Model	Kossolapov err. [K]	Richenderfer err. [K]	Jens-Lottes err. [K]	Kennel err. [K]
Dittus-Boelter [29]	19.67	15.07	10.09	3.13
Gnielinski [48]	20.31	14.06	6.09	1.74
NCFD law [52]	15.52	9.25	23.69	3.36
Corrected Gnielinski	1.34	3.08	6.09	1.74

Table 7.2: Average errors achieved by the considered models on each data sets.

Recalling that Gnielinski correlation was also providing good results on the DEBORA cases with R12 (Chapter 3) further indicates it as a proper choice regarding single-phase HTC estimation in the HFP model.

Note : We will later allow the use of the correction factor when needed to ensure a proper representation of the single-phase part when trying to assess the models associated to boiling.

7.3 NUCLEATION SITE DENSITY

The Nucleation Site Density is among the most influencing parameters over the HFP models predictions, particularly regarding wall temperature [37]. Indeed, its value directly controls the density of bubbles generated at the heater and therefore impacts both the boiling (ϕ_e) and quenching (ϕ_q) heat fluxes to the first order. Being able to come up with correct predictions of the NSD is thus critical if one wishes to properly capture the thermal behavior of the boiling surface.

In particular, a distinction has to be made between the density of sites or cavities over the surface, which is an intrinsic property of the material, versus the active sites density, *i.e.* the cavities that will actually reach thermal-hydraulics conditions to allow nucleation, which usually depends on the cavity radius R_c . The smallest cavities are less likely to be flooded by the liquid due to capillary effects and can thus become a place where a vapor bubble will grow.

The active nucleation site density, noted N_{sit} , is the one of interest when trying to model wall boiling since it control the density of bubbles that can be generated on the heater. Its value is actually influenced by

many parameters being either linked to thermal-hydraulics (wall temperature, pressure, operating fluid) or the heater material (roughness, wettability, thermal conductivity, diffusivity, etc.). That is why it is often estimated through empirical correlations, for which many different expression have been proposed over the years since the end of the XXth century as discussed below.

7.3.1 Existing Correlations

One of the firstly identified behavior of the NSD was its power dependency with the wall superheat ($N_{sit} \propto \Delta T_w^m$), which is form adopted in the correlation of Lemmert & Chawla [79] :

$$N_{sit} = [210 (T_w - T_{sat})]^{1.8} \quad (7.4)$$

Note : This law is used in the HFP model of Kurul & Podowski and NEPTUNE_CFD to compute N_{sit} .

However, such an expression misses the influence of other parameters such as pressure, which has been proven to be strongly impacting the range of active cavities that can generate bubbles as shown on Figure 7.3 and induces a larger bubble density over the heater.

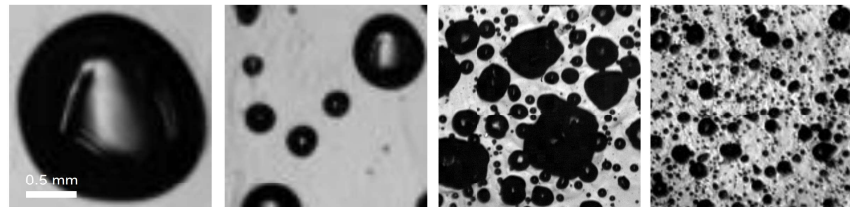


Figure 7.3: HSV Visualization of bubble density at various pressures adapted from Kossolapov [72] (left to right: 1.01 bar, 3 bar, 19.8 bar, 75.8 bar).

Moreover, experimental measurements such as in Borishanskii [9] showed that the power dependency on the wall superheat changes by increasing both with pressure and the superheat value itself. This was accounted for by Hibiki & Ishii in 2003 [57] who came up with a new correlation that requires an estimation of the minimum activated cavity radius R_c :

$$N_{sit} = N_0 \left(1 - \exp \left(-\frac{\theta^2}{8\mu^2} \right) \right) \left[\exp \left(f(\rho^+) \frac{\lambda'}{R_c} \right) - 1 \right] \quad (7.5)$$

$$R_c = \frac{2\sigma \left(1 + \frac{\rho_V}{\rho_L} \right) / P}{\exp \left(\frac{h_{LV} \Delta T_w}{R_g M T_w T_{sat}} \right) - 1} \quad (7.6)$$

$$f(\rho^+) = -0.01064 + 0.48246\rho^+ - 0.22712\rho^{+2} + 0.05468\rho^{+3} \quad (7.7)$$

with θ the contact angle, R_c the cavity radius, σ the surface tension, h_{LV} the latent enthalpy of vaporization, P the operating pressure, T_w and T_{sat} the wall and saturation temperature in Kelvins, $R_g = 8.314 \text{ J}/\text{mol/K}$ the perfect gas constant, M the molar mass of the fluid (18 g/mol for water), $N_0 = 4.72 \times 10^5 \text{ m}^{-2}$, $\mu = 0.722 \text{ rad}$, $\lambda' = 2.5 \times 10^{-3} \text{ m}$ and $\rho^+ = \log_{10} \left(\frac{\rho_L - \rho_V}{\rho_V} \right)$.

Note : This law is used in the HFP model of Gilman & Baglietto [47] and Kommajosyula [71].

We can note that it also includes the value of the static contact angle θ which can be used as a parameter to accounts for wall properties, since it is dependent on the wall roughness, wettability and the operating fluid. Indeed, a high-wetting material (low values of θ) will allow smaller cavities to be flooded by the surrounding liquid, thus hindering non-condensable gases to be captured inside and become a potentially active nucleation site (Figure 7.4).

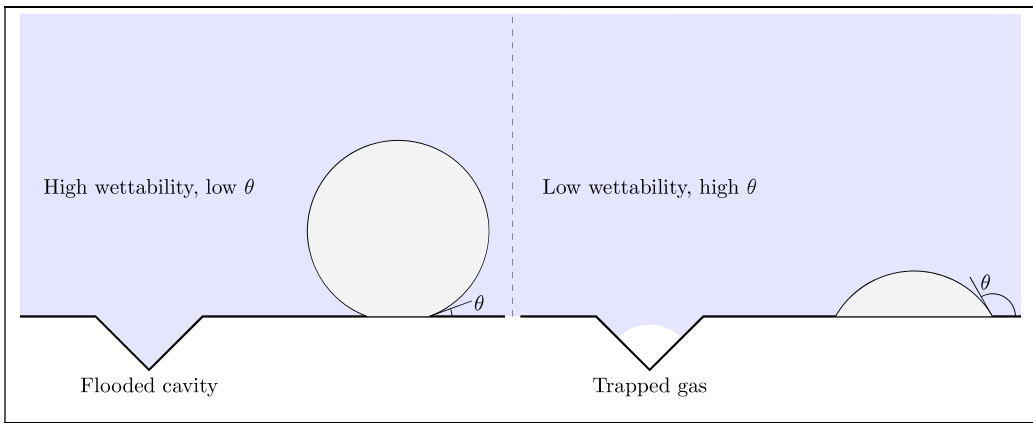


Figure 7.4: Sketch of the link between bubble contact angle and wettability / cavity flooding

This influence of the contact angle on the NSD was confirmed by experimental observations of Basu *et al.* [3] and was also included in a law correlated on their own measurements :

$$N_{sit} = \begin{cases} 0.34 [1 - \cos(\theta)] \Delta T_w^2 & \text{if } \Delta T_{w,ONB} < \Delta T_w < 15 K \\ 3.4 \times 10^{-5} [1 - \cos(\theta)] \Delta T_w^{5.3} & \text{if } \Delta T_w > 15 K \end{cases} \quad (7.8)$$

Similarly, Zhou *et al.* [145] correlated their measurements, including an influence of the pressure:

$$N_{sit} = N_0 (1 - \cos(\theta)) [\exp(f(P) \Delta T_w) - 1] \quad (7.9)$$

$$f(P) = 0.218 \ln\left(\frac{P}{P_0}\right) + 0.1907 \quad (7.10)$$

with $N_0 = 55\,395.26 \text{ m}^{-2}$ and $P_0 = 1.01 \text{ bar}$.

Finally, one of the most recent NSD correlation has been proposed by Li *et al.* in 2018 [82] and validated over a large range of measurements by including a more realistic power law for ΔT_w . It avoids the divergence of N_{sit} observed in Hibiki & Ishii law (Eq. 7.5) when reaching high pressure and superheats. It also includes the impact of pressure and contact angle and its evolution with temperature *e.g.* its decrease close to 0 ° when approaching the critical temperature [118]:

$$N_{sit} = N_0 e^{f(P)} \Delta T_w^{A \Delta T_w + B} (1 - \cos(\theta)) \quad (7.11)$$

$$f(P) = 26.006 - 3.678e^{-2P} - 21.907e^{-P/24.065} \quad (7.12)$$

$$A = -2 \times 10^{-4} P^2 + 0.0108P + 0.0119 \quad (7.13)$$

$$B = 0.122P + 1.988 \quad (7.14)$$

$$1 - \cos(\theta) = (1 - \cos(\theta_0)) \left(\frac{T_c - T_{sat}}{T_c - T_0} \right)^\gamma \quad (7.15)$$

with P in MPa, θ_0 the contact angle at room temperature T_0 , and default value being for water $\theta_0 = 41.37^\circ$, $T_c = 374^\circ\text{C}$ $T_0 = 25^\circ\text{C}$, $\gamma = 0.719$.

Remark : We can question the absence of bulk liquid velocity and temperature in the presented law since they should logically influence the nucleation process. However, this impact is rather limited as observed in experimental measurements of Zhou *et al.* [145] and Kossolapov [72].

7.3.2 Comparison with Experimental Measurements

In order to assess existing NSD correlations and choose the most pertinent to include in a HFP model, we gather NSD measurements from 4 different authors. The different operating conditions of the chosen data sets are gathered on Table 7.3.

Author	Fluid	P [bar]	G_L [kg/m ² /s]	ΔT_L [K]	ΔT_w [K]	θ_0 [°]	N_{mes} [-]
Zhou [145] (2020)	Water	1.21 - 3.12	482.7 - 1930.6	8 - 15	6.7 - 20.2	51	60
Richenderfer [108] (2018)	Water	1.01	500 - 1000	10	21.7 - 42.8	80	49
Kossolapov [72] (2021)	Water	1.01 - 75.8	500 - 2000	80	10	80°	63
Borishanskii [9] (1966)	Water	1.01 - 198	N.A.	N.A.	1.75 - 17.3	45	132

Table 7.3: Nucleation Site Density data in flow boiling

We then compare the predictions achieved by the model of Lemmert & Chawla (Eq. 7.4), Hibiki & Ishii (Eq. 7.5), Zhou *et al.* (Eq. 7.9) and Li *et al.* (Eq. 7.11). The comparison with measurements are presented on Figure 7.5.

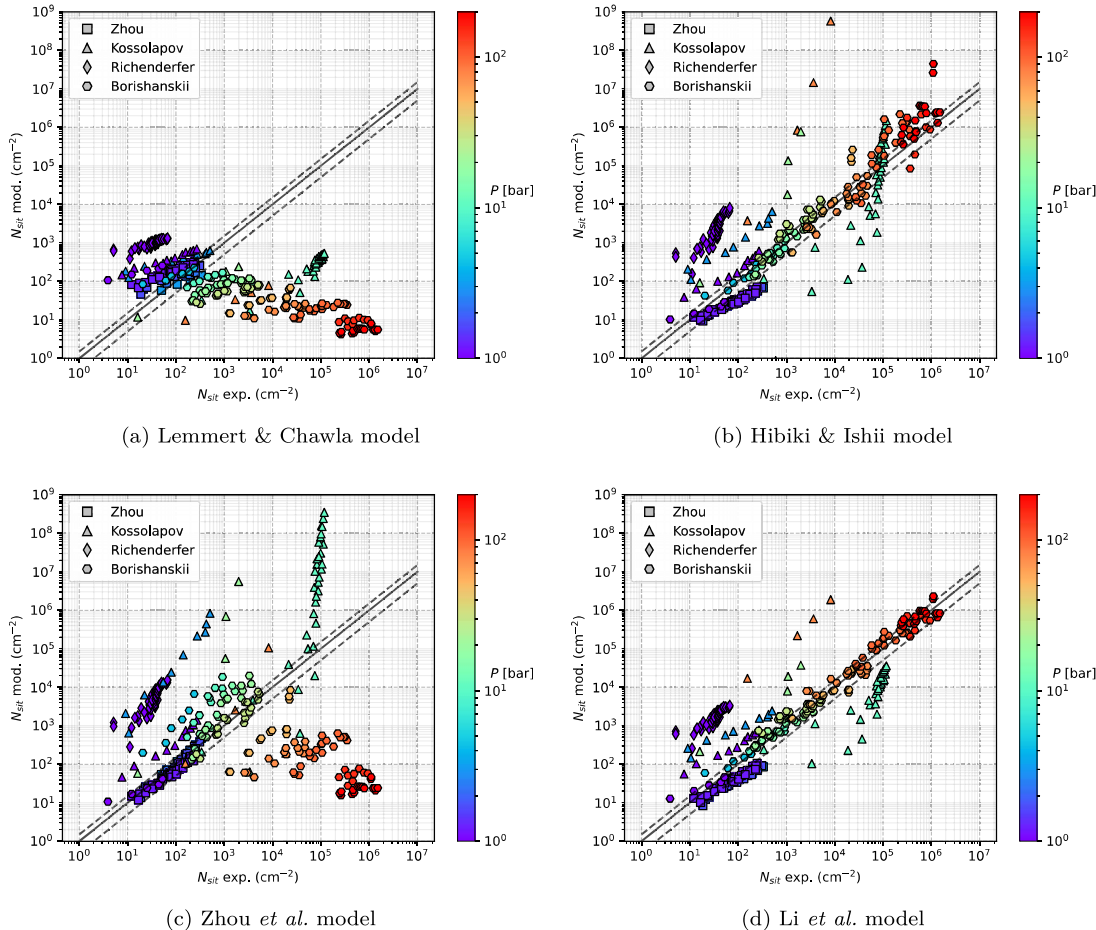


Figure 7.5: Predictions of the chosen models against the experimental data of Table 7.3 with $\pm 50\%$ error bars.
The contact angles

The Lemmert & Chawla model appears to fail in predicting the NSD at high pressures. This is a logical drawback of its sole dependence on the wall superheat. More importantly it increasingly underestimates the NSD as pressure increases, which makes it a clearly unsuitable correlation to compute N_{sit} particularly for pressurized flows such as in PWR.

Although the model of Zhou *et al.* includes a pressure term, its partial calibration on data covering a low range of pressure may explain the large error observed when compared to higher pressure measurements.

On the contrary, models from Hibiki & Ishii and Li *et al.* seem to better reproduce the different trends with flow conditions, especially with pressure. The model from Li *et al.* achieves better predictions by avoiding to reach unphysically high values of N_{sit} at higher wall superheat compared to Hibiki & Ishii. This behavior is clear over Kossolapov data at high pressure, where both model lead to overestimations, the strongest discrepancy being associated to Hibiki & Ishii model.

Overall, the model of Li *et al.* is the most efficient with an acceptable agreement on most of the data of Borishanskii and Zhou *et al.*. The measurements of Richenderfer and Kossolapov fail to be precisely reproduced, but it shows a coherent trend and the most limited error when compared to other correlations.

Remark : The coherency of NSD predictions is hard to ensure since we do not know the exact contact angle and boiling surface morphology in the experiments. This was pointed out by Richenderfer [108] who observed significant variation in the NSD value depending on the heater, though keeping the same material (ITO). For instance, this may explain the fact that the NSD measured by Kossolapov at 10.5 bar is higher than any other pressure on his experiment, leading to both underpredictions and overpredictions of the model of Li *et al.* depending on the pressure.

All things considered, those comparisons show that the Nucleation Site Density remains among the most difficult quantity to evaluate because of its very large variations over experiments, boiling surfaces and flow conditions. Dedicated correlations are hardly precise outside of their establishment databases. However, it remains the best yet only way to compute N_{sit} . **In that regard, the NSD correlation of Li *et al.* appears to be the most coherent choice.**

7.4 GROWTH TIME

As discussed in Section 6.3, the bubble growth can be acceptably modeled as:

$$R(t) = K \text{Ja}_w \sqrt{\eta_L t} \quad (7.16)$$

with value of K laying roughly between 0.1 and 2 depending on the boiling conditions.

With a given departure radius R_d , the bubble growth time until departure from nucleation site $t_{g,d}$ can be estimated as:

$$t_{g,d} = \left(\frac{R_d}{K \text{Ja}_w} \right)^2 \frac{1}{\pi \eta_L} \quad (7.17)$$

Note : This formulation is used in Gilman [46] and Kommajosyula [71] HFP models, with their own choice of value for K .

By correlating their own growth time measurements, Basu *et al.* [3] propose the following relationship including an influence of the liquid subcooling:

$$\frac{D_d^2}{\eta_L \text{Ja}_w t_{g,d}} = 45 e^{-0.02 \text{Ja}_L} \quad (7.18)$$

which is naturally used in their HFP model to compute the bubble growth time.

Remark : If precise estimations of the thermal boundary layer thickness is achievable, the new analytic expression of the bubble growth proposed in Eq. 6.101 can be used to express the growth time:

$$t_{g,d} = \left[\frac{1}{K_a} \ln \left(1 - \sqrt{1 - \frac{R_d}{R_\infty}} \right) \right]^2 \quad (7.19)$$

with K_a defined as in Eq. A.25 and R_∞ in Eq. 6.101.

This formulation requires $R_d < R_\infty$ the equilibrium radius in subcooled pool boiling. Though this condition seems logical physically speaking, it can't be ensured numerically due to the range of values attainable using correlations or other mechanistic models to estimate R_d .

7.5 WAITING TIME

The waiting time t_w between two nucleation events on an active site corresponds to the time needed for the thermal boundary layer to reconstruct after its disruption due to bubble departure from the nucleation site. This process is then intrinsically related to the heater properties and the transient heat transfer with the external liquid flow.

7.5.1 Existing Models

7.5.1.1 Analytic Approaches

Traditional approaches of the wait time estimation rely on the analytic solution to the transient heat transfer in a semi-infinite medium. Assuming that after bubble departure liquid at $T_{L,bulk}$ is displaced towards the wall at T_w , one can solve the conductive heat transfer problem at the wall with the initial and boundary conditions:

$$\frac{\partial T_L}{\partial t} = \eta_L \frac{\partial^2 T_L}{\partial y^2} \quad (7.20)$$

$$T_L(y, 0) = T_{L,bulk}, \forall y > 0 \quad (7.21)$$

$$T_L(0, t) = T_w, \forall t \geq 0 \quad (7.22)$$

The solution of this heat transfer problem if given by:

$$T_L(y, t) = T_{L,bulk} + (\Delta T_w + \Delta T_L) \operatorname{erfc} \left(\frac{y}{2\sqrt{\eta_L t}} \right) \quad (7.23)$$

For instance, Mikic & Rohsenow [93] combine this solution with the assumption that a new nucleation will occur over a cavity of radius R_c when the vapor temperature reaches:

$$T_{V,nuc} = T_{sat} + \frac{2\sigma T_{sat} \left(\frac{1}{\rho_V} - \frac{1}{\rho_L} \right)}{R_c h_{LV}} \quad (7.24)$$

The wait time is then assumed to be the time needed for the transient temperature field to reach $T_{V,nuc}$ at height $y = R_c$, i.e. $T_L(R_c, t_w) = T_{V,nuc}$. Combining Eq. 7.23 and 7.24 allow to write:

$$t_w = \frac{1}{4\eta_L} \left[\frac{R_c}{\operatorname{erfc}^{-1} \left(\frac{\Delta T_L}{\Delta T_L + \Delta T_w} + T_{sat} \left(\frac{1}{\rho_V} - \frac{1}{\rho_L} \right) \frac{2\sigma}{(\Delta T_w + \Delta T_L) h_{LV} R_c} \right)} \right]^2 \quad (7.25)$$

$$\approx \frac{1}{\pi \eta_L} \left[\frac{(\Delta T_w + \Delta T_L) R_c}{\Delta T_w - T_{sat} \left(\frac{1}{\rho_V} - \frac{1}{\rho_L} \right) \frac{2\sigma}{R_c h_{LV}}} \right]^2 \quad (7.26)$$

Using the same approach, Han & Griffith [19] use the same expression of the transient liquid temperature field but consider $T_L \left(\frac{3}{2}R_c, t_w \right) = T_{V,nuc}$, which yields a wait time that is $\frac{9}{4}$ times Eq. 7.26.

Later, Yeoh *et al.* [135] followed a similar derivation to propose an expression of the wait time that accounts for the contact angle value:

$$t_w = \frac{1}{\pi \eta_L} \left[\frac{(\Delta T_L + \Delta T_w) C_1 R_c}{\Delta T_w - \frac{2\sigma T_{sat}}{C_2 \rho_V h_{LV} R_c}} \right]^2 \quad (7.27)$$

$$C_1 = \frac{1 + \cos(\theta)}{\sin(\theta)} ; \quad C_2 = \frac{1}{\sin(\theta)} \quad (7.28)$$

All those analytical approaches present one pivotal parameter: the activated cavity radius R_c . It is a very complicated parameter to evaluate since it can vary by decades depending on the flow conditions and the boiling surface morphology.

Among existing expressions of R_c , we can mention:

$$R_c = \frac{2\sigma T_{sat}}{\rho_V h_{LV} \Delta T_w}, \text{ used by Han \& Griffith [19]} \quad (7.29)$$

$$R_c = \sqrt{\frac{1}{C_1 C_2} \frac{2\sigma T_{sat} \lambda_L}{\rho_V h_{LV} \phi_w}}, \text{ used by Yeoh } et \text{ al. [135]} \quad (7.30)$$

$$R_c = \frac{2\sigma \left(1 + \frac{\rho_V}{\rho_L} \right) / P}{\exp \left(h_{LV} \frac{\Delta T_w}{R_g T_w T_{sat}} \right)}, \text{ used by Hibiki \& Ishii [57]} \quad (7.31)$$

Remark : Those analytic expressions do not include the influence of an external liquid velocity, which could have an impact over the wait time since it modifies the hydrodynamics controlling the reconstruction of the thermal boundary layer. In particular, turbulent flows could induce a larger mixing effect between the bulk and the wall thus increasing the time needed to reach sufficient superheat to allow a new nucleation to occur.

7.5.1.2 Empirical Correlations

Alternatively, other authors considered the wait time estimation through empirical correlations based on data-fitting on given measurements. For instance, Basu *et al.* [3] proposed:

$$t_w = 139.1 \Delta T_w^{-4.1} \quad (7.32)$$

based on low pressure and low liquid velocity experiments.

Note : This expression of t_w is used in Basu *et al.* HFP model [3].

More recently, Kommajosyula [71] included the effect of the liquid subcooling through the liquid Jakob number Ja_L as:

$$t_w = 0.061 \frac{Ja_L^{0.63}}{\Delta T_w} \quad (7.33)$$

Remark : This expression, used in Kommajosyula's HFP model, will yield $t_w = 0$ for saturated boiling conditions, which is hardly reasonable since a non-zero wait time exists between two nucleation events even at saturation [45].

7.5.2 Experimental Measurements

To try to assess the proposed expressions of the bubble wait time, we rely on some experimental measurements available in the literature from Basu *et al.* [3], Richenderfer [108] and Kossolapov [72]. The boiling conditions of the data are summed up on Table 7.4.

Author	Fluid	P [bar]	G_L [kg/m ² /s]	ΔT_L [K]	ϕ_w [MW/m ²]	ΔT_w [K]	t_w [ms] (N_{mes})
Basu <i>et al.</i> [3] (2005)	Water	1.01	346.0	8.35 - 46.5	N.A.	9.83 - 17.5	0.797 - 13.3 (19)
Richenderfer [108] (2018)	Water	1 - 2	1000 - 2000	5 - 20	0.74 - 7.13	N.A.	0.914 - 6.02 (259)
Kossolapov [72] (2021)	Water	10.5	500 - 2000	10	N.A.	0.12 - 25.9	6.13 - 85.9 (33)

Table 7.4: Bubble wait time data in vertical flow boiling. Wall superheat values for Richenderfer data are estimated using Frost & Dzakowic correlation (Eq. 6.108).

The experimental data are all using water as working fluid. We can see at first glance that values measured by Kossolapov are nearly a decade larger compared to the other experiments. This may be an effect of pressure due to:

- The bubbles that are smaller and depart nearly right after nucleation, leaving wait time as the main part of the nucleation cycle ;
- The wall Jakob number values that are smaller ;
- The heterogeneity in nucleation sites behavior (their number increasing with pressure), with sites exhibiting very large wait time due to their very low nucleation frequency versus very active sites that contributes much more to the overall nucleation. This can partially be explained by the local decrease in wall temperature when a bubble nucleates (acting locally as a heat sink), potentially deactivating the neighboring sites. Averaging over those events as done by Kossolapov [72] may result in a large wait time.

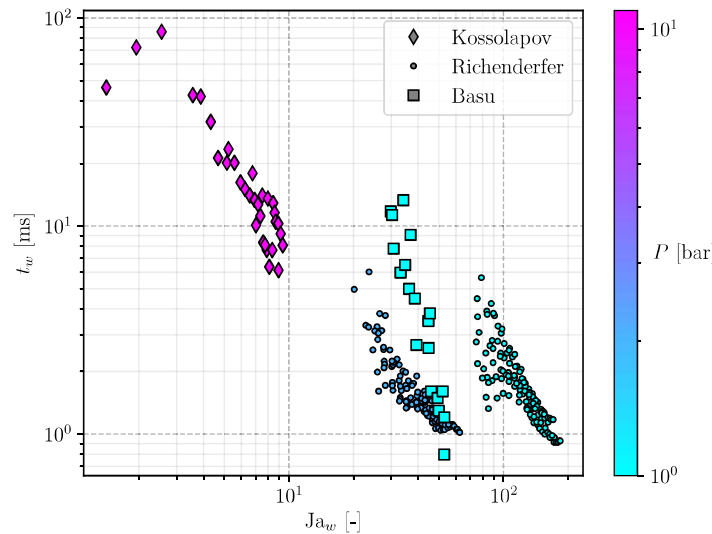


Figure 7.6: Evolution of the wait time values with the wall Jakob number.

On Figure 7.6, we show the evolution of the measures wait times with the wall Jakob number. We can see that the low values of Jakob number actually correspond to high wait times, which seems to confirm the previous assumptions.

Moreover, we see that there is a steep decrease of the wait time with Ja_w . The slope however changes depending on the data set, which would logically depend on the heater thermal properties as well as on the operating fluid. It seems that the slope followed by Kossolapov data at 10 bar seem to align with that of Richenderfer data at 2 bar, which would exhibit a sort of coherency between those two data sets. On the contrary, values at 1 bar from Basu do not clearly match with Richenderfer data at 1 bar.

The data sets from Kossolapov and Richenderfer also give the associated frequency to each wait time measurement. This allows to plot the product $t_w \times f$ to evaluate the proportion of the nucleation cycle occupied by wait time. The value of $t_w \times f$ would physically be expected to tend to 1 when $\Delta T_w \rightarrow 0$ (highly reduced nucleation) and to 0 when $\Delta T_w \rightarrow \infty$ due to the intense nucleation and increased transient heat transfer under the high temperature gradient between the wall and the fluid. Experimental values are plotted on Figure 7.7 versus the reduced Jakob number $\text{Ja}_w^* = \frac{c_{p,L}\Delta T_w}{h_{LV}}$ values to regroup the values by excluding the influence of the density ratio ρ_L / ρ_V .

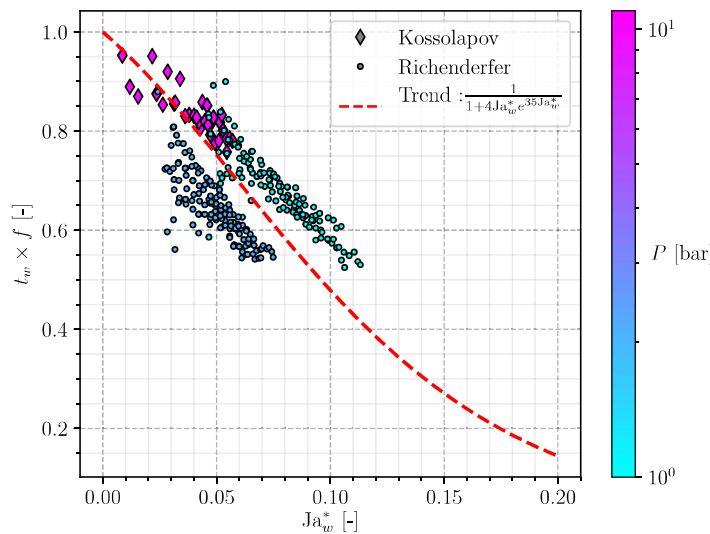


Figure 7.7: Evolution of the product $t_w \times f$ with the reduced Jakob number.

We can see that for lower values of Ja_w^* , the product $t_w \times f$ starts to tend to 1. For higher values, a linear decrease seem to be the general trend of the measurements. However, it can't decrease linearly forever, which is why the trend on Figure 7.7 extrapolated to higher values of Ja_w^* looks like a sigmoid in order to approach zero for large superheats. Nevertheless, we clearly lack of measurements at larger values of Ja_w^* to confirm this supposed trend.

Remark : The range of values attained by the product $t_w \times f$ can vary from 1 down to 0.5 on the chosen experimental data. This clearly shows that the relation between the wait time and the growth time is not straightforward as assumed in some works who neglects the growth time or suppose a constant relationship such as $t_w = 3t_g$ [19].

Moreover the boiling conditions range covered by the data are not that exhaustive, leaving room for even larger ranges of $t_w \times f$ with different fluids and heater material for instance.

7.5.3 Evaluation of the Models

Using the data of Table 7.4 to evaluate the different approaches presented above, we obtain the results presented on Figures 7.8 and 7.9.

The correlation of Basu *et al.* naturally performs well on their own data but largely underestimates the wait time for Richenderfer and Kossolapov data. Kommajosyula's formulation produces better results on

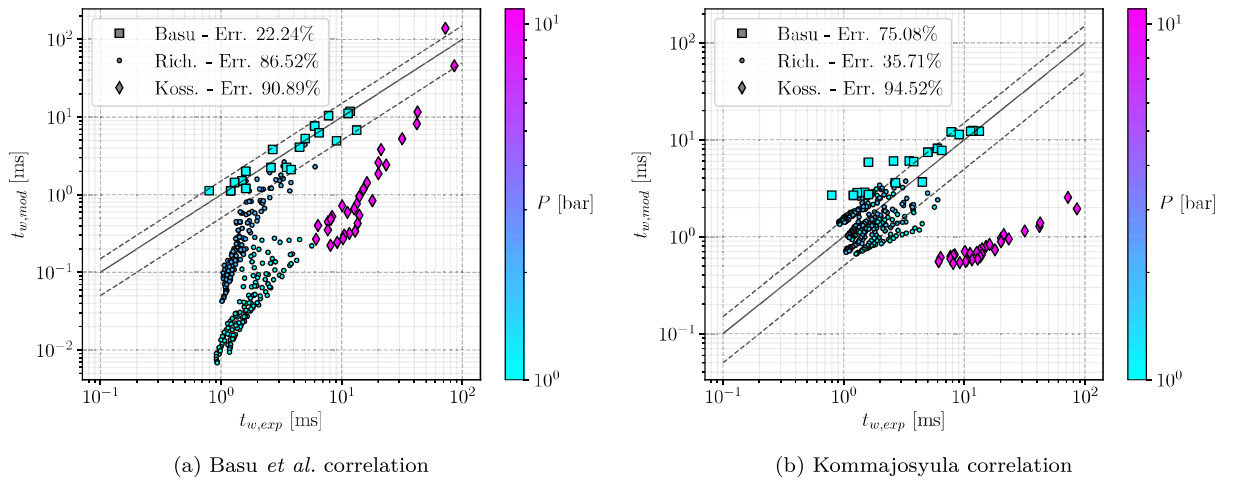


Figure 7.8: Predictions using the correlations. $\pm 50\%$ dashed lines are represented.

the low pressure cases, particularly on Richenderfer cases. However, it fails to capture the increase in t_w for Kossolapov data and largely underestimates them.

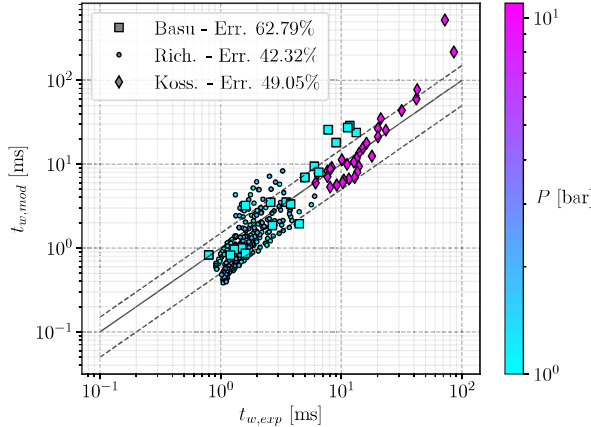


Figure 7.9: Yeoh *et al.* formulation of t_w with Han & Griffith cavity radius. $\pm 50\%$ dashed lines are represented.

When testing the analytic formulations of the wait time, we tested different combinations of (t_w, R_c) expressions. Overall, we saw that the results were strongly dependent on the value of the cavity radius with values that can change by decades depending on the chosen formulation.

At last, it appeared that choosing the Yeoh *et al.* expression of t_w (Eq. 7.27) along with the cavity radius of Han & Griffith (Eq. 7.29) resulted in good results in average over the three chosen datasets. As we can see on Figure 7.9, it produces overall better results compared to the correlation. Moreover, we used contact angle values that were representative of each experimental conditions according to each author:

- $\theta = 31^\circ$ for Basu *et al.* data [4] (metallic surface) ;
- $\theta = 72^\circ$ for Richenderfer data [108] (ITO on sapphire) ;
- $\theta = 80^\circ$ for Kossolapov data [72] (ITO on sapphire).

Remark : Obviously, since the wait time results from a transient heat transfer between the wall and the liquid after the bubble departure, it should strongly depend on the wall thermal properties (*e. g.* its effusivity). However, they are not accounted for in the analytic expressions, with solely the contact angle being related to the wall material.

The fact that the analytic expression is able to correctly predict the large range of t_w values from the different experiments is encouraging since it is based on a physical approach contrary to correlations which mainly relies on data-fitting.

To conclude, it seems appropriate to use the wait time formulation of Yeoh *et al.* along with expressing cavity radius using Han & Griffith estimation. We must though keep in mind that the model is sensitive to the value of the contact angle θ , which has to be evaluated in order to make proper use of the analytic expressions.

7.6 CONSIDERATIONS ON BUBBLE INTERACTIONS AND NUCLEATION SITES DEACTIVATION

7.6.1 Nucleation Site Distribution

NSD correlations actually estimate the total number of sites where bubbles can nucleate on a surface. However, experimental observations showed that nucleation sites exhibit largely heterogeneous behaviors. For instance, Figure 7.10 shows experimental observations from Kossolapov [72] that demonstrate the variety of nucleation frequency measured for each site on a boiling surface.

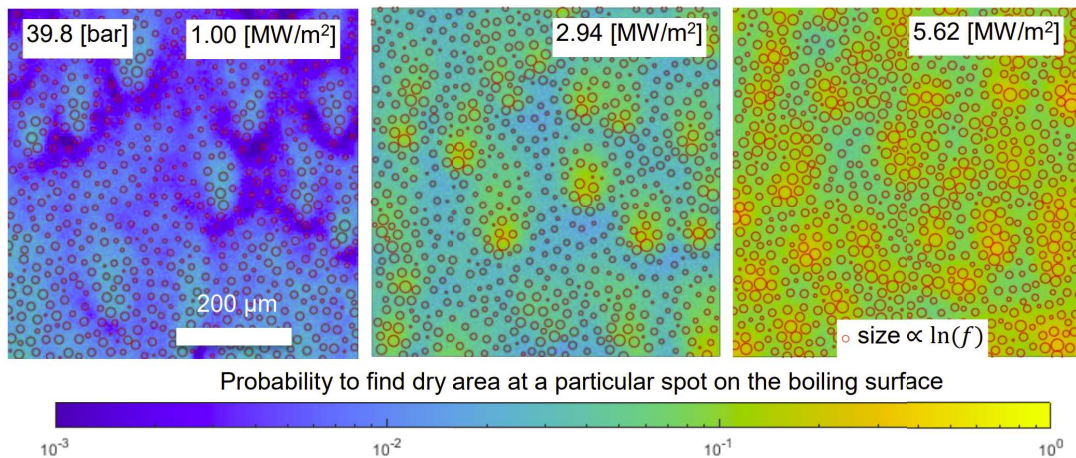


Figure 7.10: Nucleation site distribution by and adapted from Kossolapov [72]. Red circles represent the active sites positions with diameter increasing with the site's nucleation frequency.

This large difference in nucleation frequency between the different sites indicates that a minority of sites contribute to most of the total phase change process. Those differences may originate from different interactions such as:

- Thermal deactivation: a bubble nucleating at a site gathers the energy in the wall to use it for phase change, which in turns locally decreases the temperature and will hinder nucleation to occur at neighboring sites.
- Static deactivation: given a number of active sites, distributing a number of bubbles of radius R_d over them can lead to overlapping that can not geometrically be accommodated on the wall. This effect was notably considered by Gilman & Baglietto [47].
- Sliding deactivation: if a bubble slides and swipes a given area, sites laying on its path may experience quenching even before holding a nucleating bubble. This consequently will impact their nucleation frequency and may lead to partial deactivation under the sliding effect.

In order to consider such interactions between nucleation sites, we need to know their spatial distribution over the boiling surface. Usual approaches considered that the nucleation sites followed an homogeneous spatial Poisson process *i.e.* the probability of finding a site in an area A only depends on the value of A and not on its location over the boiling surface.

This has been supported by different experimental observations such as those of Gaertner [40] or Sultan [123] for pool boiling who found an agreement between site distribution and Poisson process by studying

sites populations in subdivisions of the boiling surface. It was also confirmed for flow boiling by Del Valle & Kenning [26] who observed site distribution at different heat fluxes. However, they noticed that the increase in nucleation site with the heat flux did not come from an additive effect of new sites since some active sites at low heat fluxes became inactive at higher heat fluxes before sometimes reactivating later (see Figure 7.11a). This further highlights that the interactions and deactivation processes originate from complex physics that simultaneously include wall morphology and thermal behavior, external flow influence and bubble presence.

More recent observations also show a random distribution of the sites such as in Zhou *et al.* [144] (Figure 7.11b).

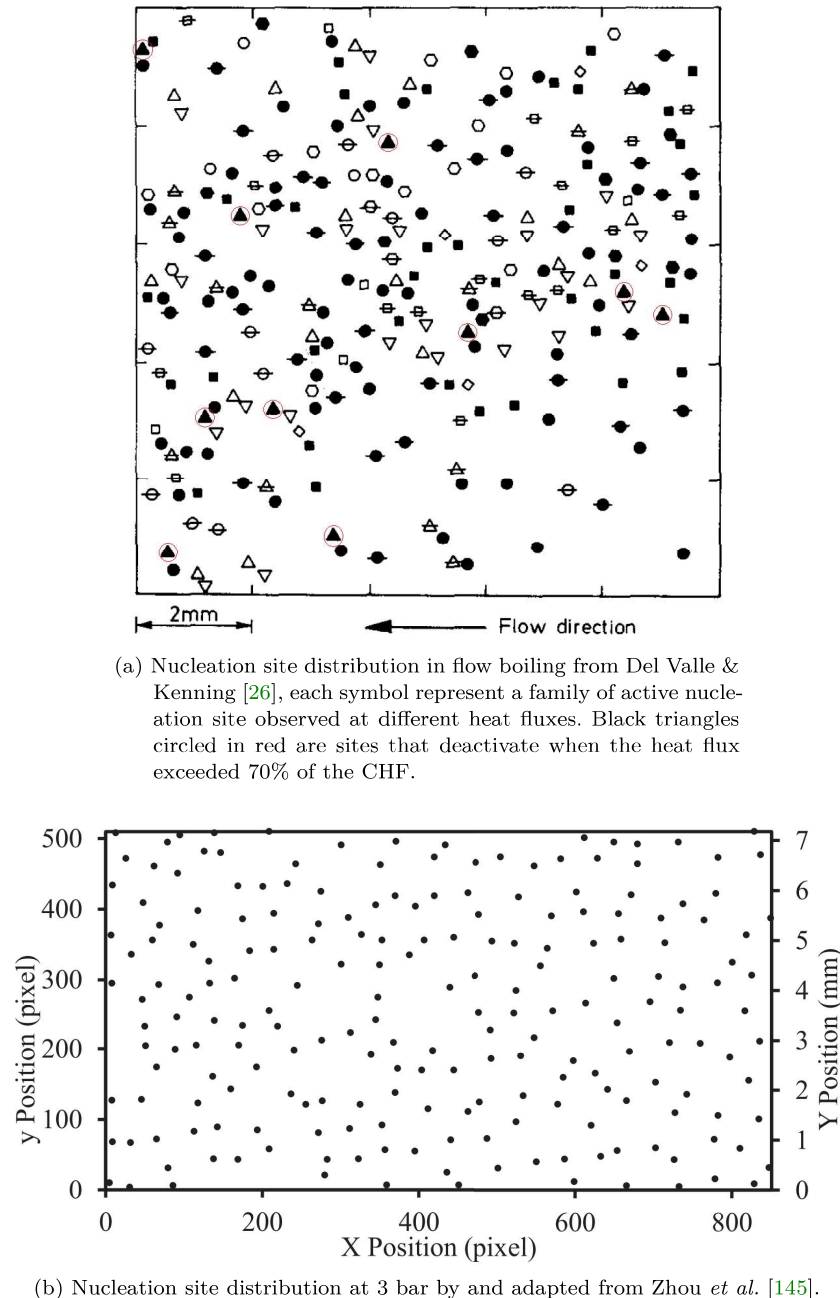


Figure 7.11: Examples of experimental nucleation sites distribution in flow boiling.

Considering an homogeneous spatial (two-dimensional) Poisson process with an event density (*i.e.* average number of events per unit of area) λ , then the probability that the number of events N in an area A is equal to $n \in \mathbb{N}$ is [25]:

$$\mathcal{P}(N(A) = n) = \frac{(\lambda A)^n}{n!} e^{-\lambda A} \quad (7.34)$$

Then, one can express the probability density function of the nearest-neighbor, depending on the distance r between two events as:

$$f(r) = 2\lambda\pi r e^{-\lambda\pi r^2} \quad (7.35)$$

This special case of Poisson point-processes is also called "Complete Spatial Randomness".

Remark : Although observations of the boiling surface presented random distributions of sites close to a Poisson process, Del Valle & Kenning [26] found that the measured nearest-neighbor distance distribution was deviating from Eq. 7.35 for low values of r .

Eq. 7.35 allows to compute the average distance s between two events:

$$s = \int_0^{+\infty} r f(r) dr = 2 \frac{\sqrt{\pi}}{4\sqrt{\lambda\pi}} = \frac{1}{2\sqrt{\lambda}} \quad (7.36)$$

Note : In the case of boiling physics, the word "event" can refer to active nucleation sites or bubbles on the surface.

From those mathematical expressions, we can then model different type of interactions between sites by choosing proper event densities λ . Further subsections propose treatments of a few of them.

7.6.2 Static Deactivation

Note : This calculation has originally been conducted by Gilman [47] and continued by Komma-josyula [71].

Let us consider the nucleation site density N_{sit} computed by a correlation as in Section 7.3. As mentioned earlier, if we distribute a given number of bubbles of radius R_d over the different sites, we have no guarantee that the correlation avoids too large values of N_{sit} that would lead to geometrical overlapping as shown on Figure 7.12.

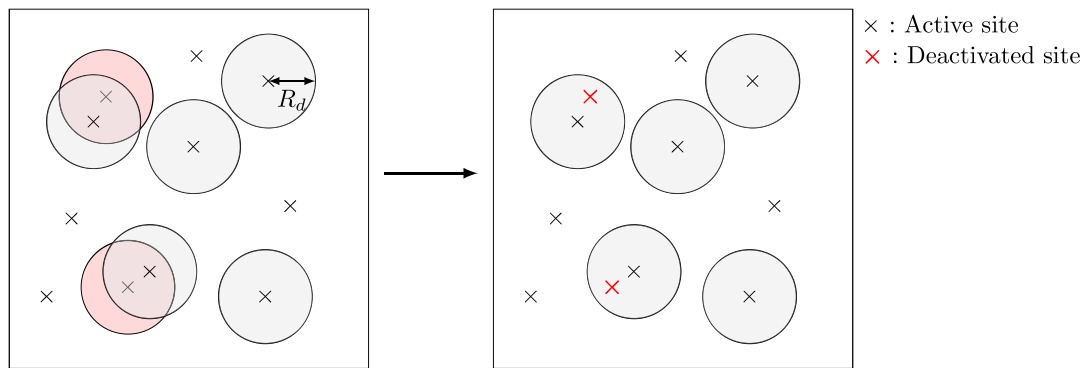


Figure 7.12: Sketch of the geometrical overlapping leading to static deactivation. Bubbles in red can not be accommodated on the surface due to their site laying below an existing bubble.

Thus, we need a correction of N_{sit} to obtain the actual number of active sites $N_{sit,a}$ that can geometrically fit on the surface regarding the nucleation parameters. Given a bubble growth time before departure $t_{g,d}$ and an average nucleation frequency f , we can estimate the actual number of bubbles growing attached to their sites on the boiling surface as:

$$N_b = t_{g,d} \times f \times N_{sit,a} \quad (7.37)$$

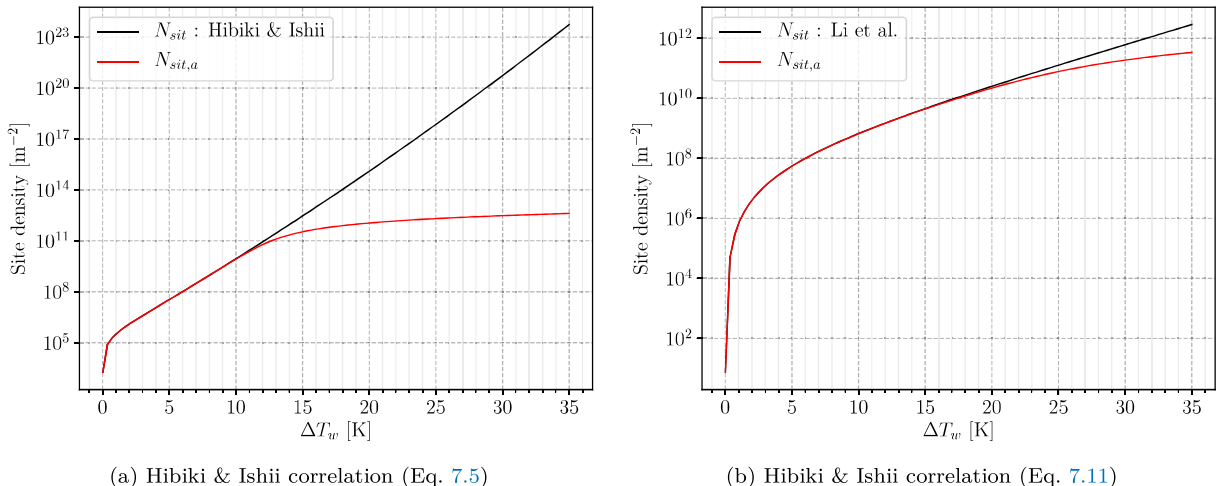


Figure 7.13: Static deactivation correction tested with Hibiki & Ishii and Li *et al.* correlations for water at 40 bar, $f = 200$ Hz, $t_{g,d} = 0.1$ ms, $\theta = 80^\circ$ and $R_d = 0.01$ mm.

If N_b is used as an event density in the Poisson process, we can estimate the probability to have an undesired overlapping *i.e.* two simultaneous bubbles of radius R_d on neighboring sites at a distance $r \leq R_d$:

$$\mathcal{P}(r \leq R_d) = 1 - \underbrace{\mathcal{P}(N(\pi R_d^2) = 0)}_{\text{No bubble nucleates within } \pi R_d^2} = 1 - e^{-N_{sit,a} t_{g,d} f \pi R_d^2} = \mathcal{P} \quad (7.38)$$

This overlapping probability \mathcal{P} can then be used to ponderate the number of sites given by the NSD correlation, yielding:

$$N_{sit,a} = (1 - \mathcal{P}) N_{sit} \quad (7.39)$$

$$\Leftrightarrow N_{sit,a} t_{g,d} f \pi R_d^2 e^{N_b t_{g,d} f \pi R_d^2} = N_{sit} t_{g,d} f \pi R_d^2 \quad (7.40)$$

$$\Leftrightarrow N_{sit,a} = \frac{\mathcal{W}(N_{sit} A_{sit})}{A_{sit}} \quad (7.41)$$

where $A_{sit} = t_{g,d} f \pi R_d^2$ and \mathcal{W} is Lambert's W-function (reciprocal of $x \rightarrow xe^x$).

The evaluation of \mathcal{W} can easily be achieved with a few iterations of a bisection method. Otherwise, Kommajosyula proposed an approximation to allow its direct computation [71].

On Figure 7.13 we show the impact of the correction of Eq. 7.41 on NSD correlations of Hibiki & Ishii (Eq. 7.5) and Li *et al.* (Eq. 7.11).

Li *et al.* correlation present a significant correction for larger wall superheat due to its formulation that damps the exponential growth of the NSD at high superheat. On the contrary, the well-known drawback of Hibiki & Ishii correlation which yields too large N_{sit} value at high superheat is strongly ponderated by the static deactivation correction.

7.6.3 Static Coalescence

Now that the actual number of bubble-generating sites have been identified, we can consider other interaction phenomena that can occur on the boiling surface. For instance, if two bubbles are simultaneously growing on sites at a distance lower than $2R_d$, the bubbles will coalesce while growing up to the detachment diameter (Figure 7.14).

Using the bubble density N_b (Eq. 7.37) as the event density in Eq. 7.35, the probability of static coalescence is:

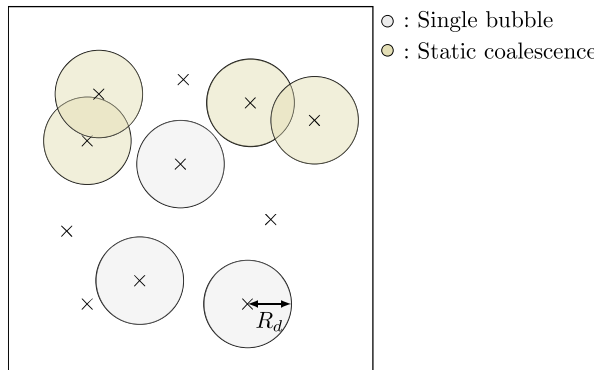


Figure 7.14: Sketch of the static coalescence phenomenon.

$$\mathcal{P}(r \leq 2R_d) = \int_0^{2R_d} f(r) dr = 1 - e^{-N_b \pi (2R_d)^2} = \mathcal{P}_{coal,st} \quad (7.42)$$

The density of bubble-generating sites that will lead to a static coalescence can then be estimated as :

$$N_{coal,st} = \mathcal{P}_{coal,st} N_{sit,a} \quad (7.43)$$

Figure 7.15 the evolution of $\mathcal{P}_{coal,st}$ with the wall superheat for two departure radius values, using the same conditions as in Figure 7.13.

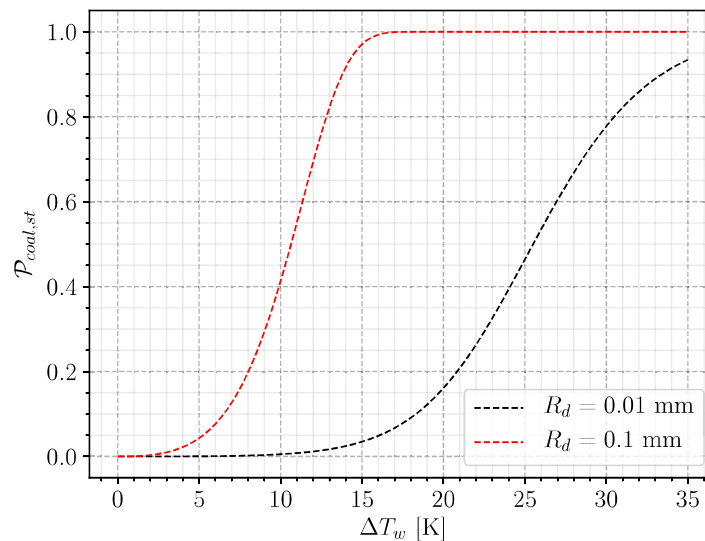


Figure 7.15: Static coalescence probability with corrected Li *et al.* for water at 40 bar, $f = 200$ Hz, $t_{g,d} = 0.1$ ms and $\theta = 80^\circ$.

7.6.4 Sliding Coalescence

The question of sliding coalescence is partly addressed by Basu *et al.* [3] (Section 5.3) by comparing the computed sliding distance of a single bubble $l_{sl,0}$ with the average distance between two active nucleation sites $s = 1/\sqrt{N_{sit,a}}$ (twice the value obtained if we use the Poisson distribution Eq. 7.36). They suppose that if $l_{sl,0} > s$ bubble coalescence will occur during the sliding phase and reduces the number of sites generating sliding bubbles.

Remark : Their approach is based on the distribution of active nucleation sites $N_{sit,a}$ and not on the bubble density N_b which could better represent the average distance between two bubbles actually living on the surface.

Using the spatial distribution, if the total area covered by a single sliding bubble is $A_{q,1b}$ and the number of sites generating sliding bubbles N_{sl} , we can estimate:

- The probability of finding no growing bubbles in area $A_{q,1b}$, meaning no sliding coalescence (NC):

$$\mathcal{P}_{NC} = \exp(-N_{sit,a}t_{g,d}fA_{q,1b})$$
- The number of sites generating sliding bubbles without coalescence : $N_{sl,NC} = N_{sl} \times \mathcal{P}_{NC}$
- The number of sites generating sliding bubbles that will coalesce with others: $N_{sl,C} = N_{sl} \times (1 - \mathcal{P}_{NC})$
- The number of sites, present in sliding bubbles path, that will not be holding growing bubbles :

$$N_{nob} = N_{sit,a} \times N_{sl,NC} \times A_{q,1b}$$

Those types of calculations are interesting if one wishes to further distinguish many different types of bubble behavior, and particularly *if we dispose of a sliding length for single bubbles $l_{sl,0}$ meaning that single bubble lift-off would be considered*. This point being questionable in vertical flow boiling as discussed in Section 6.6.

7.7 BUBBLE SLIDING LENGTH

Estimation of the bubble sliding length is critical for the evaluation of the quenching term since it acts as an enhancing factor of the wall area that will undergo transient heat transfer.

As discussed in Section 6.6, if we consider that bubble lift-off occurs when a sliding bubble coalesces with an other bubble growing on its site, the sliding length l_{sl} shall be close to the average distance between two nucleation bubbles on the boiling surface. This value has been derived in Section 7.6:

$$l_{sl} = s_b = \frac{1}{2\sqrt{N_b}} \quad (7.44)$$

with N_b the bubble density from Eq. 7.37.

To assess the validity of this assumption, we compare on Figure 7.16 values of sliding length obtained using either the bubble density N_b or the active site density $N_{sit,a}$ (Eq. 7.41). Since their expression depend on the values of f , $t_{g,d}$ and R_d , we take:

- $R_d = 0.015$ mm at 40 bar and $R_d = 0.02$ mm at 20 bar (see Table 6.3) ;
- $ft_{g,d} = 0.1$ or $ft_{g,d} = 0.01$ since bubble departure by sliding becomes nearly instantaneous after nucleation as pressure increases [72].

First, we must acknowledge that the ranges of measured sliding length by Kossolapov include bubbles that do not slide to the longest observed distance. When looking at the statistical distribution provided in his work [72], bubbles seem to averagely slide around half the longest distance measured in the experiments.

The evaluation using the average distance between two active sites is always clearly underestimating the sliding distance. This seems natural due to the heterogeneity and temporal asynchronism between active sites regarding their nucleation behavior. On the contrary, estimating the distance using the bubble density with very low values of $ft_{g,d}$ seem to better approach the actual sliding length. Only a clear overestimation is observed for the $P = 20$ bar and $G = 500$ kg/m²/s case for which we can speculate that values of $ft_{g,d}$ may be larger.

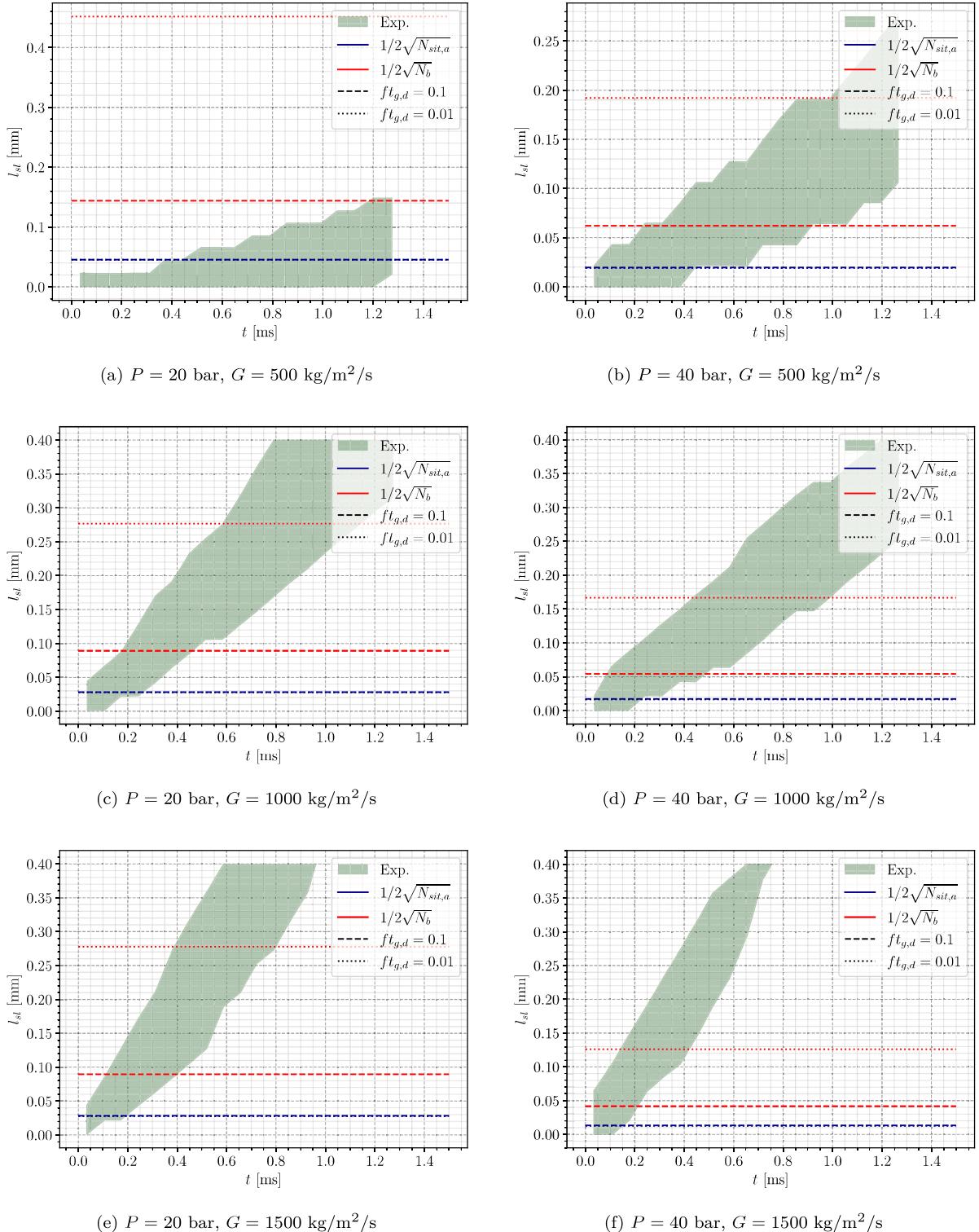


Figure 7.16: Comparison of sliding distance estimations with Kossolapov measurements [72]. NSD was estimated using Li *et al.* correlation (Eq. 7.11).

7.8 SINGLE BUBBLE QUENCHING AREA

When computing the quenching heat flux, we need to provide the total wall area visited by a single bubble $A_{q,1b}$ that will undergo quenching. In wall boiling model that do not consider bubble sliding [52, 73, 102] the impacted area at bubble lift-off is often considered as :

$$A_{q,1b} = F_A \pi R_{lo}^2 \quad (7.45)$$

with F_A being an enhancement factor that accounts for the possibility that the bubble will induce quenching over a surface larger than its projected area. For instance, we remind that Kurul & Podowski used $F_A = 4$ in their model [73].

Remark : This question of bubble influence area has been discussed by different authors. Yoo *et al.* [138] experimentally found enhancement factor up to 14 for small sliding bubbles. On the contrary, Kossolapov [72] observed that the area undergoing quenching was exactly the surface covered by the bubble footprint that can be even smaller than the bubble projected area. This aspect seems still open to discussions and may need extra experimental observations to reach a solid conclusion. **In this work, we will simply consider that the bubble induces transient heat transfer over its projected area.**

Otherwise, models that account for bubble sliding [3, 47, 71, 135] compute the quenching area using the sliding length l_{sl} as:

$$A_{q,1b} = l_{sl} (R_d + R_{lo}) \quad (7.46)$$

However, depending on the relationship between l_{sl} , R_d and R_{lo} , the quenching area induced by a single sliding bubble without coalescence can have different shapes as pictured in Figure 7.17.

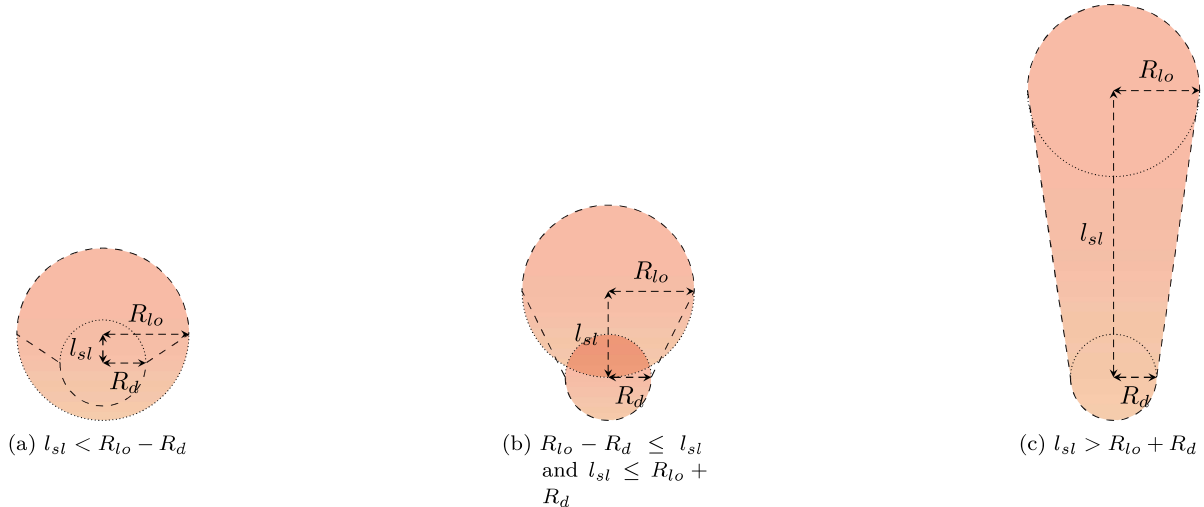


Figure 7.17: Quenching area shape depending on the relation between R_d , R_{lo} and l_{sl} , if the bubble do not experience multiple coalescence while sliding.

Based on Figure 7.17, we can then write:

$$A_{q,1b} = \begin{cases} \pi R_{lo}^2 & \text{if } l_{sl} \leq R_{lo} - R_d \\ \frac{1}{2}\pi R_d^2 + l_{sl} (R_d + R_{lo}) + \frac{1}{2}\pi R_{lo}^2 & \text{if } l_{sl} \geq R_{lo} + R_d \end{cases} \quad (7.47)$$

Which can be re-expressed by defining $l_{sl}^* = \frac{l_{sl}}{R_{lo}}$ and $A_{q,1b}^* = \frac{A_{q,1b}}{\pi R_{lo}^2}$

$$A_{q,1b}^* = \begin{cases} 1 & \text{if } l_{sl}^* \leq 1 - \frac{R_d}{R_{lo}} \\ \frac{1}{2} \left(1 + \left(\frac{R_d}{R_{lo}} \right)^2 \right) + \frac{l_{sl}^*}{\pi} \left(1 + \frac{R_d}{R_{lo}} \right) & \text{if } l_{sl}^* \geq 1 + \frac{R_d}{R_{lo}} \end{cases} \quad (7.48)$$

and we linearly interpolate those two expressions for the region where $1 - \frac{R_d}{R_{lo}} \leq l_{sl}^* \leq 1 + \frac{R_d}{R_{lo}}$.

7.9 ASSEMBLING A NEW HEAT FLUX PARTITIONING

Based on all the discussions conducted in Chapter 6 and in previous Sections of this Chapter, we will now propose a formulation for the HFP model.

In our approach, we consider the following partitioning (Figure 7.18):

- A liquid convective heat flux $\phi_{c,L}$ associated to forced convection ;
- An evaporation heat flux based on static coalescence between adjacent bubbles nucleating on very close sites $\phi_{e,coal,st}$;
- An evaporation heat flux based on sliding coalescence between a sliding bubble and a growing bubble on its site $\phi_{e,coal,sl}$;
- A quenching heat flux due to transient conduction following bubble departure, sliding and lift-off ;
- A vapor convective heat flux $\phi_{c,V}$ that accounts for the portion of the wall directly in contact with vapor under a bubble footprint.

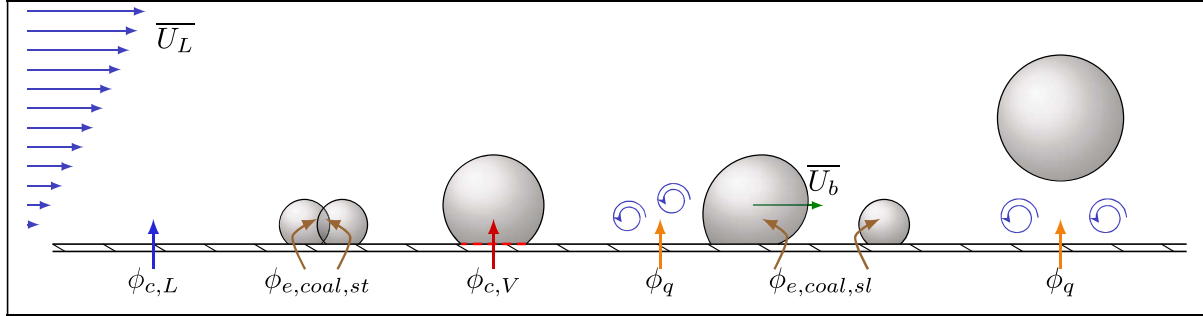


Figure 7.18: Sketch of all the considered heat transfers for the new HFP model.

The total wall heat flux then writes:

$$\phi_w = \phi_{c,L} + \phi_{e,coal,st} + \phi_{e,coal,sl} + \phi_q + \phi_{c,V} \quad (7.49)$$

7.9.1 Liquid Convective Heat Flux

The liquid convective heat flux $\phi_{c,L}$ is naturally computed as:

$$\phi_{c,L} = A_{c,L} h_{c,L} (T_w - T_L) = h_{c,L} (\Delta T_w + \Delta T_L) \quad (7.50)$$

where $A_{c,L}$ is the proportion of the wall area that is affected by liquid forced convection.

The liquid heat transfer coefficient $h_{c,L}$ is computed using Gnielinski correlation (Eq. 3.21) that has proven to be efficient for wall temperature predictions in single-phase regimes both for R12 and water (3.5.2 and 7.2).

7.9.2 Static Coalescence Evaporation Heat Flux

The static coalescence arises from the calculation of the probability for two bubbles to nucleate at a distance lower than $2R_d$ (Eq. 7.42) which gives the proportion of active nucleation sites that will produce this type of bubble (Eq. 7.43).

Assuming that the bubbles will merge at a radius close to R_d , we can compute the associated evaporation heat flux:

$$\phi_{e,coal,st} = N_{coal,st} f \rho_V h_{LV} \frac{4}{3} \pi R_d^3 \quad (7.51)$$

This heat flux can also be expressed using the resulting radius of the coalescence:

$$\phi_{e,coal,st} = \frac{N_{coal,st}}{2} f \rho_V h_{LV} \frac{4}{3} \pi R_{coal,st}^3 \quad (7.52)$$

$$R_{coal,st} = (R_d^3 + R_d^3)^{1/3} = 2^{1/3} R_d \quad (7.53)$$

7.9.3 Sliding Coalescence Evaporation Heat Flux

Since we identified the active sites that will lead to static coalescence, we consider that the remaining sites will generate bubbles for which lift-off occurs under sliding coalescence. Meaning that half of the sites will generate a sliding bubble and the other half a static bubble that will coalesce with the sliding one. This results in a bubble of diameter:

$$R_{coal,sl} = (R_{sl}^3 + R_d^3)^{1/3} \quad (7.54)$$

Where R_{sl} is the diameter of the sliding bubble after a distance $l_{sl} = \frac{1}{2\sqrt{N_b}}$ (Eq. 7.44). The sliding part is solved following the bubble dynamics model that has been developed in Section 6.5 after departure at radius R_d computed using Eq. 6.107.

We can thus write:

$$\phi_{e,coal,sl} = \frac{N_{coal,sl}}{2} f \rho_V h_{LV} \frac{4}{3} \pi (R_{sl}^3 + R_d^3) \quad (7.55)$$

7.9.4 Quenching Heat Flux

The quenching heat flux is split in two parts:

- Quenching from static coalescing bubbles, each of them having a projected area of πR_d^2 ;
- Quenching from sliding coalescing bubbles, for which the total swiped area can be expressed using Eq. 7.47 with a lift-off radius being the resulting coalescence radius (Eq. 7.54).

The time during which the transient heat transfer will take place depends on the relationship between the total wait time t_w and the theoretical time t^* at which the heat transfer coefficient of transient conduction and forced convection are equal:

$$h_{c,L} (\Delta T_w + \Delta T_L) = \frac{\lambda_L (\Delta T_w + \Delta T_L)}{\sqrt{\pi \eta_L t^*}} \quad (7.56)$$

$$\Leftrightarrow t^* = \left(\frac{\lambda_L}{h_{c,L}} \right)^2 \frac{1}{\pi \eta_L} \quad (7.57)$$

If the wait time t_w is lower than t_* , then transient conduction dominates during the whole period between two nucleation and the quenching time t_q is thus equal to t_w .

Otherwise, if $t_w > t^*$ the wait time will consist of transient heat transfer during t^* before being dominated by forced convection up to t_w . The quenching time t_q in this case is then t^* .

Then, using the transient heat transfer solution (mentioned in Section 7.5, also derived by Del Valle [26]), we can write the total quenching flux as:

$$\phi_q = A_q t_q f \frac{2\lambda_L (\Delta T_w + \Delta T_L)}{\sqrt{\pi \eta_L t_q}} \quad (7.58)$$

$$A_q = N_{coal,st} \pi R_d^2 + \frac{N_{coal,sl}}{2} A_{q,1b} \quad (7.59)$$

$$t_q = \min(t_w, t^*) \quad (7.60)$$

where $A_{q,1b}$ is computed using Eq. 7.47 with $R_{coal,sl}$ as the lift-off radius.

7.9.5 Vapor Convective Heat Flux

Assuming that the vapor is at saturation temperature, we can write:

$$\phi_{c,V} = A_{c,V} h_{c,V} (T_w - T_{sat}) = A_{c,V} h_{c,V} \Delta T_w \quad (7.61)$$

where $A_{c,V}$ is the portion of the wall area in direct contact with vapor.

The vapor heat transfer coefficient is estimated simply based on a conductive transfer over a bubble radius:

$$h_{c,V} = \frac{\lambda_V}{R} \quad (7.62)$$

For a truncated spherical bubble, the vapor contact area is its foot area : $\pi R^2 \sin(\theta)$. Since the bubbles are supposed to grow following a \sqrt{t} law (Section 6.3), the average radius for a bubble over its growth time t_g is:

$$\bar{R} = \frac{1}{t_g} \int_0^R r \, dr = \frac{1}{t_g} \int_0^{t_g} K \text{Ja}_w \sqrt{\eta_L t} \, dt = \frac{1}{t_g} K \text{Ja}_w \frac{2}{3} \sqrt{\eta_L} t_g^{3/2} = \frac{2}{3} R \quad (7.63)$$

Distinguishing between the bubbles that coalesce while growing up to R_d on their site and sliding bubbles that reaches R_{sl} , we have:

$$A_{c,V} = \left(N_{coal,st} + \frac{N_{coal,sl}}{2} \right) \pi \left(\frac{2}{3} R_d \sin(\theta) \right)^2 + \frac{N_{coal,sl}}{2} \pi \left(\frac{2}{3} R_{sl} \sin(\theta) \right)^2 \quad (7.64)$$

The time-averaged surface proportion occupied by bubble footprints is then:

$$\overline{A_{c,V}} = \left(N_{coal,st} + \frac{N_{coal,sl}}{2} \right) \pi \left(\frac{2}{3} R_d \sin(\theta) \right)^2 \times t_{g,df} + \frac{N_{coal,sl}}{2} \pi \left(\frac{2}{3} R_{sl} \sin(\theta) \right)^2 \times t_{g,lof} \quad (7.65)$$

7.9.6 Liquid Convection Area

Using the expressions of A_q and $A_{c,V}$, we can deduce the remaining unaffected area $A_{c,L}$:

$$A_{c,L} = 1 - A_q t_q f - \overline{A_{c,V}} \quad (7.66)$$

7.9.7 Model Summary

On Tables 7.5 and 7.6, we gather the formulations and closure laws of the proposed Heat Flux Partitioning model.

In the end, we can see that to fully close the model, we need to set 3 parameters values being:

- The contact angle θ which should be chosen in reasonable ranges regarding the heater surface and working fluid. As discussed earlier, usual uncertainties for contact angle measurements usually lie around 5° to 10° [50].

- The contact angle hysteresis $d\theta$ of the tilted bubble. It plays a role in determining the capillary term in the non-dimensional approach (Chapter 6). Although precise measurements and its dependency on flow parameters are clearly lacking, it seems that values higher than 10° are acceptable for low pressure flows (larger bubbles) and decrease down to a few degrees when reaching higher pressures such as 40 bar.
- The bubble growth constant K whose value has been discussed earlier (Section 6.3). Its value should roughly lie between 0.1 and 2 depending on the flow conditions. It appeared that for subcooled low pressure flow match with values of $K < 1$ while at higher pressures $1 \leq K \leq 2$ better represent the bubble growth regime.

Physical Parameter	Modeling
Liquid Convective Heat Transfer Coefficient $h_{c,L}$	$\text{Nu}_L = \frac{h_{c,L} \lambda_L}{D_h} = \frac{\frac{C_f}{2} (\text{Re}_{D_h} - 1000) \text{Pr}}{1 + 12.7 \sqrt{\frac{C_f}{2} (\text{Pr}^{2/3} - 1)}}, C_f = 0.036 \text{Re}_{D_h}^{-0.1818}$
Departure Radius R_d	$C_{AM,x} K^2 \frac{\text{Ja}_w^2}{\text{Pr}_L} + \frac{1}{3} \frac{\text{Re}_b}{\text{Fr}} + \frac{1}{8} C_D \text{Re}_b > \frac{1}{2} \frac{f_{C,x}(\theta, d\theta)}{\text{Ca}}$ $C_{AM,x} = 0.636, C_D = (1 + \Delta C_D) C_{D,U}$ (See Eq. 6.35)
Sliding Velocity U_b	$\left(1 + \frac{\rho_L}{\rho_V} C_{AM,x}\right) \frac{dU_b}{dt} = \left(\frac{\rho_L}{\rho_V} - 1\right) g + \frac{3}{8} \frac{C_D}{R} \frac{\rho_L}{\rho_V} (U_L - U_b) U_L - U_b + 3 \frac{\dot{R}}{R} \left[C_{AM,x} \frac{\rho_L}{\rho_V} (U_L - U_b) - U_b \right] - \frac{3}{4} \frac{\sigma}{\rho_V} \frac{f_{C,x}}{R^2}$
Bubble Growth Law & Times t_g	$R(t) = K \text{Ja}_w \sqrt{\eta_L t}, t_g = \left(\frac{R}{K \text{Ja}_w}\right)^2 \frac{1}{\eta_L}$
Bubble Wait Time t_w	$t_w = \frac{1}{\pi \eta_L} \left[\frac{(\Delta T_L + \Delta T_w) C_1 R_c}{\Delta T_w - \frac{2\sigma T_{sat}}{C_2 \rho_V h_{LV} R_c}} \right]^2, C_1 = \frac{1 + \cos(\theta)}{\sin(\theta)}, C_2 = \frac{1}{\sin(\theta)}$ $R_c = \frac{2\sigma T_{sat}}{\rho_V h_{LV} \Delta T_w}$
Nucleation Frequency f	$f = \frac{1}{t_{g,d} + t_w}$
Nucleation Site Density N_{sit}	$N_{sit} = N_0 e^{f(P) \Delta T_w A \Delta T_w + B} (1 - \cos(\theta))$ $f(P) = 26.006 - 3.678e^{-2P} - 21.907e^{-P/24.0.65}$ $A = -2 \times 10^{-4} P^2 + 0.0108P + 0.0119, B = 0.122P + 1.988$ $1 - \cos(\theta) = (1 - \cos(\theta_0)) \left(\frac{T_c - T_{sat}}{T_c - T_0}\right)^\gamma, \gamma = 0.719$ P in MPa, θ_0 contact angle at room temperature. (Eq. 7.11)
Active Nucleation Site Density $N_{sit,a}$	$N_{sit,a} = \frac{\mathcal{W}(N_{sit} A_{sit})}{A_{sit}}, A_{sit} = t_{g,d} f \pi R_d^2, \mathcal{W}$ is Lambert's W-function
Nucleating Bubbles Density N_b	$N_b = t_{g,d} f N_{sit,a}$
Average Sliding Distance l_{sl}	$l_{sl} = \frac{1}{2\sqrt{N_b}}$
Static & Sliding Coalescing Site Density $N_{coal,st}$ & $N_{coal,sl}$	$N_{coal,st} = \mathcal{P}_{coal,st} N_{sit,a}, N_{coal,sl} = (1 - \mathcal{P}_{coal,st}) N_{sit,a}$ $\mathcal{P}_{coal,st} = 1 - \exp(-N_b \pi (2R_d)^2)$
Static & Sliding Coalescence Radiiuses $R_{coal,st}$ & $R_{coal,sl}$	$R_{coal,st} = 2^{1/3} R_d, R_{coal,sl} = (R_d^3 + R_{sl}^3)^{1/3}, R_{sl}$ sliding diameter after l_{sl}

Table 7.5: Summary of the HFP model closure laws

Physical Parameter	Mathematical Formulation
Liquid Convective Heat Flux $\phi_{c,L}$	$\phi_{c,L} = A_{c,L} h_{c,L} (\Delta T_w + \Delta T_L)$ $A_{c,L} = 1 - A_q - A_{c,V} + A_q \max \left(0, \frac{t_w - t_q}{t_q} \right)$
Static Coalescence Evaporation Heat Flux $\phi_{e,coal,st}$	$\phi_{e,coal,st} = N_{coal,st} f \rho_V h_{LV} \frac{4}{3} \pi R_d^3$
Sliding Coalescence Evaporation Heat Flux $\phi_{e,coal,sl}$	$\phi_{e,coal,sl} = \frac{N_{coal,sl}}{2} f \rho_V h_{LV} \frac{4}{3} \pi (R_{sl}^3 + R_d^3)$
Quenching Heat Flux ϕ_q	$\phi_q = A_q t_q f \frac{2\lambda_L (\Delta T_w + \Delta T_L)}{\sqrt{\pi \eta_L t_q}}$ $A_q = N_{coal,st} \pi R_d^2 + \frac{N_{coal,sl}}{2} A_{q,1b}$ $A_{q,1b} = \pi R_{coal,sl}^2 \times A_{q,1b}^* \text{ with } A_{q,1b}^* \text{ by Eq. 7.48}$
Vapor Convective Heat Flux $\phi_{c,V}$	$\phi_{c,V} = A_{c,V} h_{c,V} \Delta T_w$ $h_{c,V} = \frac{\lambda_V}{R}$ $A_{c,V} = \left(N_{coal,st} + \frac{N_{coal,sl}}{2} \right) \pi \left(\frac{2}{3} R_d \sin(\theta) \right)^2 + \frac{N_{coal,sl}}{2} \pi \left(\frac{2}{3} R_{sl} \sin(\theta) \right)^2$

Table 7.6: Summary of the HFP model formulation

7.10 CONCLUSION

In this Chapter, we covered different aspects related to the construction of the HFP model, including the evaluation of closure laws required to complete the mathematical model.

At last, we can remember that:

- Single phase heat transfer coefficient is well predicted using Gnielinski correlation, with errors on the wall temperature below 3K for single-phase water flows in various conditions. A corrective factor of 4 had to be used for cases where only one side of the channel is heated to account for geometry difference regarding the correlation establishment.
- Nucleation site density using existing correlations have been assessed using different experiments with water. Covering a large range of pressure, it appeared that Li *et al.* [82] formulation was better at predicting the experimental nucleation site density. In particular, the influence of pressure is very significant and must be accounted for. However, we must keep in mind that although the nucleation site density is critical for wall boiling modeling, its value depends on very fine details of the boiling surface which are not always accessible.
- The bubble wait time has been studied using some existing experimental measurements. Its strong decrease with the wall superheat makes it accounting between nearly 100% down to 50% of the total nucleation period. Comparison of wait time values predictions showed that analytic approaches could perform better than correlations, though this requires an estimation of the active cavity radius which can be very tricky depending and surface-dependent.
- Considering sites and bubble interactions can be achieved under the hypothesis that they both follow an homogeneous spatial Poisson point-process. The mathematical formulations can then be used to account for events such as nucleation site suppression and bubble static coalescence.
- Bubble sliding length was found to be in reasonable agreement with the average distance between two nucleating bubbles on the wall, which can be associated to the fact that bubble leave the surface when coalescing with another one.

- A new heat flux partitioning model was finally proposed in which the boiling flux is computed based on coalescence event avoiding the need of a particular closure law for the lift-off diameter D_{lo} , which estimation for single bubbles was questionable as discussed in Section 6.6. Moreover, the departure and sliding includes the detailed force balance approach developed in Chapter 6.

Next chapter will be dedicated to the validation of the new HFP model through comparisons with wall temperature measurements in vertical flow boiling.

8

VALIDATION OF THE HEAT FLUX PARTITIONING MODEL

Contents

8.1	Detailed Comparison and Assessment of the Heat Flux Partitioning	141
8.1.1	Active Nucleation Site Density	142
8.1.2	Wait Time, Growth Time, Quenching Time and Nucleation Frequency	142
8.1.3	Single Bubble Area and Total Bubble Area	143
8.1.4	Flux Proportions and Wall Superheat	143
8.2	Wall Temperature Predictions	146
8.2.1	Kossolapov Data	146
8.2.2	Jens-Lottes Data	147
8.2.3	Kennel Data	148
8.3	Validation for DEBORA Experiment	151
8.4	Conclusions	151

In this Chapter, we want to assess the validity of the new Heat Flux Partitioning formulation proposed in Chapter 7. To do so, we will conduct two different validations:

- The first part will be dedicated to validation on a single experimental subcooled boiling case at 10.5 bar from Kossolapov [72] for which numerous physical parameters have been measured. This will ensure that the mathematical formulation and the closure laws propose an acceptable physical modeling of the boiling parameters.
- The second part will consist on wall temperature predictions for vertical subcooled flow boiling of water in various conditions, including pressure. Experimental database from Jens & Lottes [61], Kennel [65] and Kossolapov [72]. Comparison with other HFP models from Kurul & Podowski, Basu and Kommajosyula will be performed.

8.1 DETAILED COMPARISON AND ASSESSMENT OF THE HEAT FLUX PARTITIONING

In this section, we compare our results to those obtained by Kossolapov [72] in vertical subcooled flow boiling. At a pressure of 10.5 bar, he realized measurements of many relevant parameters regarding the Heat Flux Partitioning:

- Active nucleation site density $N_{sit,a}$;
- Bubble nucleation frequency f ;
- Bubble wait time t_w ;
- Transient heat transfer (quenching) time t_q ;
- Average bubble growth time t_g ;
- Average area visited by a bubble $A_{q,1b}$;
- Proportion of the heater area impacted by bubbles $A_{b,tot}$
- Liquid single-phase heat flux proportion $\frac{\phi_{c,L}}{\phi_w}$;

- Quenching heat flux proportion $\frac{\phi_q}{\phi_w}$;
- Wall superheat ΔT_w .

The only lacking parameters to conduct a full evaluation of the model would be the average bubble departure diameter R_d , sliding length l_{sl} and lift-off diameter / coalescence diameter.

The values provided by Kossolapov are an average conducted over all the observed nucleation events during the time of the experiment. Such data are representative of what we want to achieve using a HFP model since we represent average values of the boiling parameters for the considered boiling surface.

All those variables were measured for a subcooling $\Delta T_L = 10^\circ\text{C}$ at three different liquid mass fluxes $G_L = 500, 1000$ and $2000 \text{ kg/m}^2/\text{s}$.

We present the results obtained by comparison with the case at $G_L = 2000 \text{ kg/m}^2/\text{s}$ for each variable. The simulations using the HFP model were conducted using a contact angle $\theta = 85^\circ$ (usual contact angle for water and ITO [72]), an hysteresis $d\theta = 2^\circ$ and a growth constant $K = 0.8$

8.1.1 Active Nucleation Site Density

On Figure 8.1, we compare the values obtained for the active nucleation site density. The Li *et al.* correlation used in the model (Eq. 7.11) propose a reasonable prediction of the measured values of $N_{sit,a}$ with an underestimation of less than a decade. The correlation correctly reproduce the experimental trend where we observe a sort of saturation in the nucleation site density for higher wall superheat.

To better match the asymptotic value of the experiment, we correct the Li *et al.* correlation for this case by a factor $\Delta T_w^{2-0.3\Delta T_w^{0.5}}$ which better fits the measurements for $\Delta T_w > 10 \text{ K}$ but yields a small overestimation before.

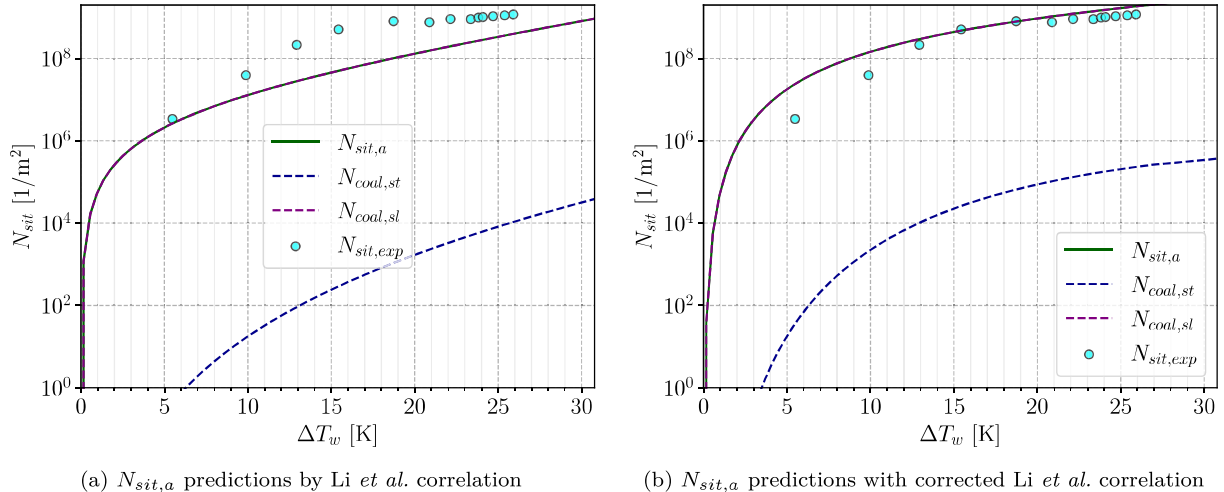


Figure 8.1: Comparison of active nucleation site density with and without a correction for Li *et al.* formulation.

Note : Following comparisons are conducted using the corrected value of $N_{sit,a}$ to limit the impact of the nucleation site density prediction over the other parameters.

8.1.2 Wait Time, Growth Time, Quenching Time and Nucleation Frequency

Figure 8.2 compares the different times involved in the boiling physics and the bubble nucleation frequency. As seen in Section 7.5, the wait time is quite fairly reproduced along with the nucleation frequency. Actually, the bubble departure is nearly instantaneous and the nucleation cycle is mainly composed of the wait period, which means a good estimation of t_w leads to a reasonable estimation of f for this case.

The average bubble growth time is overestimated by nearly a decade for low superheat and is better predicted for larger superheat. Its evolution seem coherent with a decrease up to 15 K and a stabilization afterwards. However, the experimental measurements show an increase in the growth time for large superheat which could be associated to bubble diameter increase with the wall Jakob number as previously observed in Section 6.6. This could be in partial contradiction with the single coalescence hypothesis for the lift-off since the average distance between bubbles is likely to decrease with wall superheat, thus decreasing the average growth time. On the other hand, the growth time overprediction may be associated to sliding length overestimation.

A very good approximation of the quenching time t_q is achieved using the time t^* (Eq. 7.57). This indicates that for this experimental case, the large value of the wait time implies that the transient conduction will be limited to a duration t^* and that the remaining wait time will be governed by forced convection.

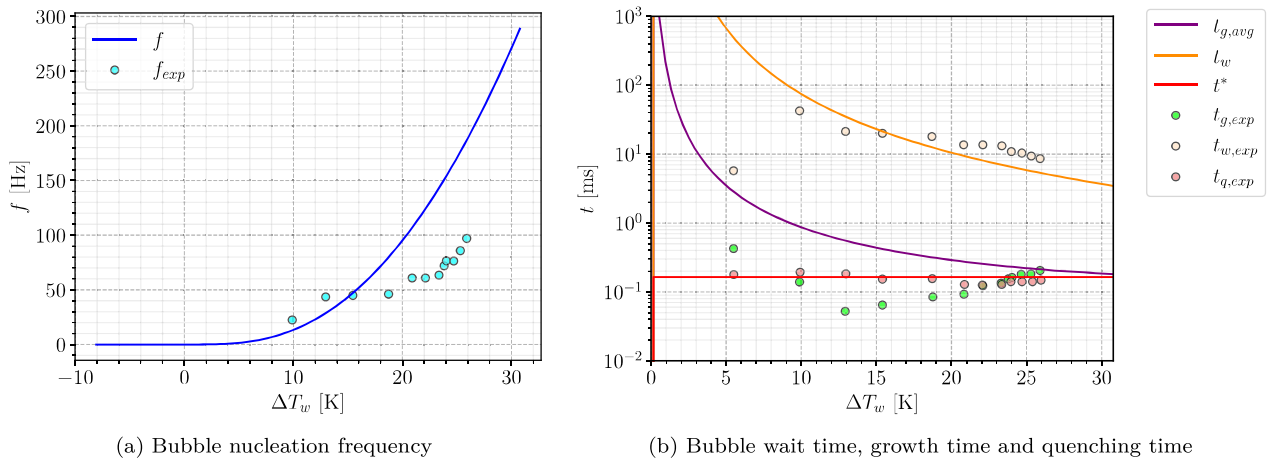


Figure 8.2: Comparison of bubble nucleation frequency, wait time, growth time and quenching time.

8.1.3 Single Bubble Area and Total Bubble Area

Figure 8.3 that the total area visited by a bubble is largely overestimated for the whole boiling curve. It only achieves a reasonable order of magnitude at high wall superheat ($\Delta T_w > 23$ K). This could question the usual hypothesis that supposes a sliding length l_{sl} equal to the average distance between bubbles $s_b = 0.5/\sqrt{N_b}$. The sole projected area of the bubbles is in average better for the visited area, but underpredicts the largest values of $A_{q,1b}$ when bubbles start sliding over significant lengths.

Moreover, both values do not reproduce the experimental trend where the visited area regularly increases with the wall superheat. Further experimental insights regarding the behavior of the bubble sliding length could allow a better modeling of l_{sl} depending on the bubble lift-off process as discussed in Section 6.6.

Those results naturally lead to an overprediction of the wall area fraction impacted by bubbles but shows an coherent increasing trend with wall superheat.

On Figure 8.4, we indicatively show the values of sliding length l_{sl} , departure diameter R_d and sliding diameter R_{sl} when sliding over l_{sl} . The small values of R_d are coherent with nearly immediate departure by sliding, with sliding radiiuses close to 0.1 mm.

8.1.4 Flux Proportions and Wall Superheat

Figure 8.5 finally compares the fraction of single-phase convection and quenching over the total heat flux ϕ_w along with the boiling curve. The evolution of the single-phase flux reasonably agrees with the experiment and becomes 0 at a superheat similar to the measurement. However, the quenching heat flux is logically overestimated due to the significant overestimation of the area visited by a single bubble.

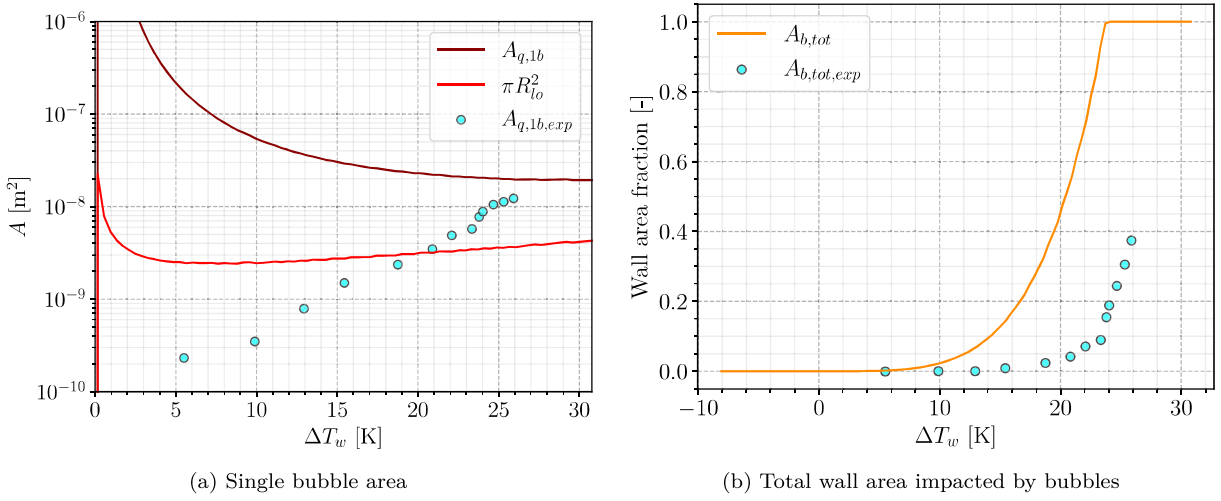


Figure 8.3: Comparison of average area visited by a bubble and total wall fraction area impacted by bubbles (footprint or transient conduction).

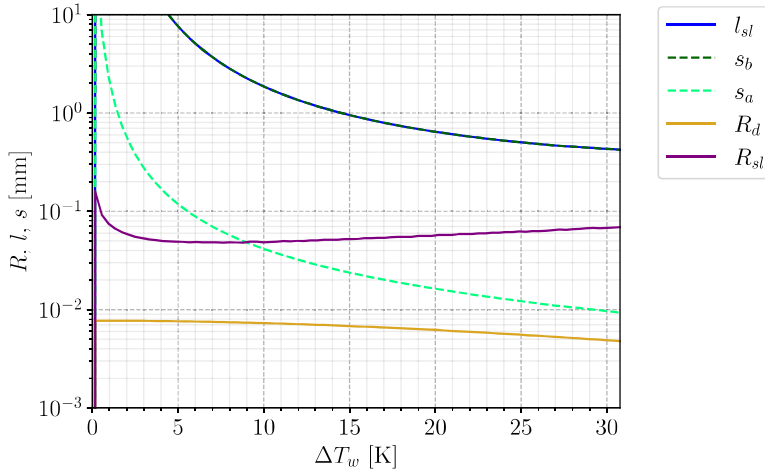


Figure 8.4: Bubble radii, sliding length and distances between sites.

On the other hand, the boiling curve is pretty well predicted except for the last experimental measurement where an increase in wall temperature starts, which could correspond to conditions close to the CHF that can't yet be detected by the HFP model.

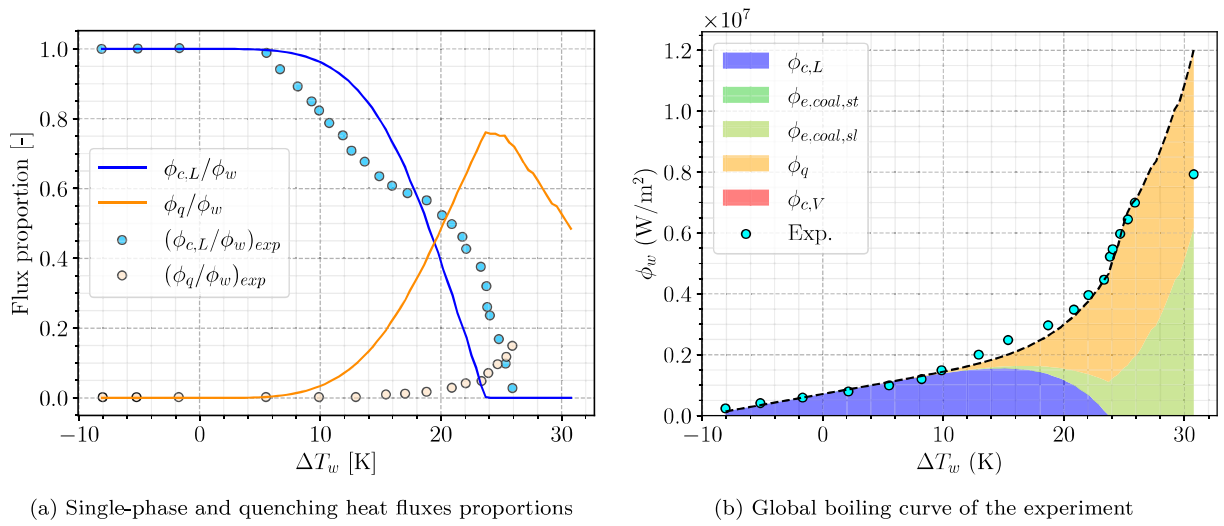


Figure 8.5: Comparison of the resulting heat flux partitioning along with the boiling curve.

8.2 WALL TEMPERATURE PREDICTIONS

In this section, we want to evaluate the model's capability to predict wall temperature in boiling regimes for different flow conditions. To do so, we gather boiling curves data from the literature for water that covers a large range of flow conditions as detailed in Table 8.1.

Author	D_h [mm]	P [bar]	G_L [kg/m ² /s]	ΔT_L [K]	ϕ_w [MW/m ²]	ΔT_w [K]	N_{mes} [-]
Kossolapov [72] (2021)	11.78	1.12 - 75.8	500 - 2000	10	0.23 - 7.93	1.55 - 30.77	81
Jens-Lottes [61] (1951)	5.74	137.9	2617.5	53.3 - 92.2	2.15 - 3.63	1.81 - 4.16	38
Kennel [65] (1948)	4.3 - 13.2	2 - 6.2	284 - 10 577	11.1 - 83.3	0.053 - 6.35	1.64 - 49.7	172

Table 8.1: Experimental data range of wall temperature measurements in the boiling region.

The following sub-sections compare the results for wall superheat predictions obtained using four models: Kurul & Podowski (Section 5.2), Basu *et al.* (Section 5.3), Kommajosyula (Section 5.5) and the new formulation (Section 7.9).

In order to propose consistent choices required closing parameters for the new formulation, we will discuss the values attributed to the contact angle θ , bubble inclination $d\theta$ and constant value in bubble growth rate K .

8.2.1 Kossolapov Data

The boiling curves from Kossolapov's work [72] are among the most recent available data and notably include various operating pressures. The experimental setup consists of a heated flat plate of ITO in vertical flow boiling in a rectangular channel.

As stated by Kossolapov, the contact angle for water and ITO usually lies between 80° and 90° [72]. The bubble tilt is likely to be very low for high pressure cases (see Sec. 6.4) and the bubble growth rate coefficient K shall be closer to $1.5 / 2$ at high pressure while it can be lower than 1 for low pressure cases. The chosen values are then:

- $\theta = 85^\circ$;
- $d\theta = 1^\circ$ for $P > 5$ bar and $d\theta = 5^\circ$ otherwise ;
- $K = 1.5$ for $P > 5$ bar and $K = 1.0$ otherwise.

Figure 8.6 shows two typical boiling curves along with the heat flux partitioning obtained using the new formulation for Kossolapov cases at 19.8 bar and 75.8 bar.

We can observe that experimental profiles are quite fairly reproduced in both cases. The model also shows different types of heat flux partitioning with the case at 75.8 bar starting to have a significant proportion of static coalescence evaporation flux. This is probably a consequence of both the high pressure and large wall superheat resulting in a very large nucleation site density and increasing the probability for two bubbles to coalesce early in their lifetime.

Figure 8.7 shows the wall temperature predictions achieved with the different HFP models.

We can note that the new formulation generally better agrees with experimental measurements but yields significant underestimation of low wall superheat values for low pressure cases. The predictions achieved by Kurul & Podowski and Kommajosyula models seem similar while Basu *et al.* formulation largely overestimates the wall temperature with an average error above 100 K.

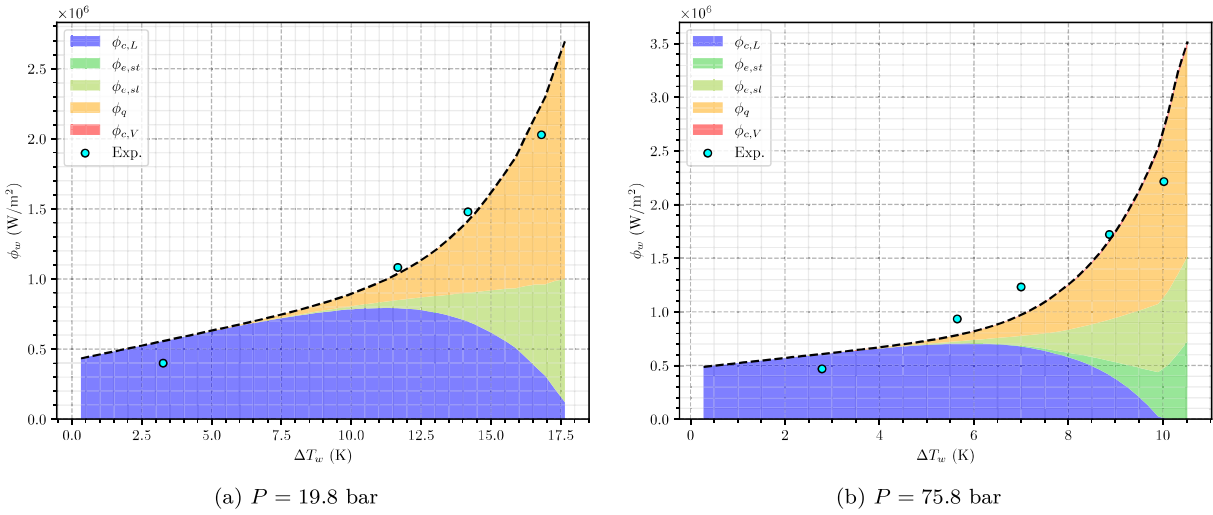


Figure 8.6: Comparison with measured boiling curves from Kossolapov [72]. $\Delta T_L = 10^\circ\text{C}$ and $G_L = 1000 \text{ kg/m}^2/\text{s}$.

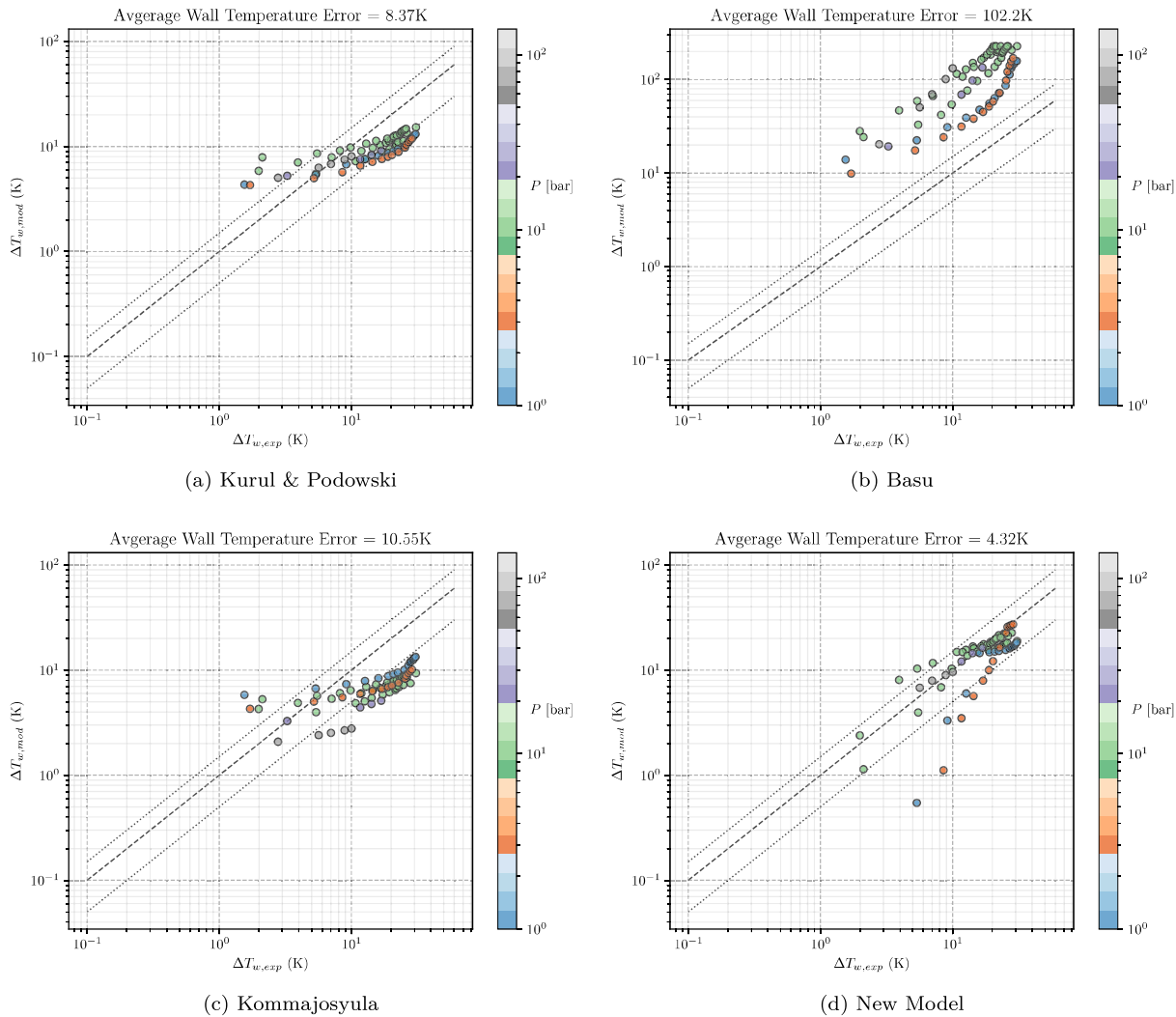


Figure 8.7: Wall temperature predictions achieved by the different HFP models on Kossolapov data.

8.2.2 *Jens-Lottes Data*

The data of Jens & Lottes are of particular interest for the HFP validation since they were obtained in conditions close to PWR ones, with an operating pressure of 138 bar, liquid mass flux above $2500 \text{ kg/m}^2/\text{s}$

and high inlet liquid subcooling. The experiment consisted of an integrally heated metallic circular pipe. Precise evaluation of the contact angle in those conditions is tricky but, according to the work of Song & Fan [118], the water contact angle on metallic surfaces (*e.g.* stainless steel) at large pressure present a very large decrease when reaching surface temperatures above 200°C. Since saturation temperature of water at 138 bar is $T_{sat} \approx 335^\circ\text{C}$, the boiling measurements lie largely in the low contact angle zone. Therefore, we will assume:

- $\theta = 20^\circ$;
- $d\theta = 1^\circ$ (very high pressure leading to nearly non-tilted bubbles) ;
- $K = 2.0$ (very high pressure and low Jakob numbers).

Figure 8.8 shows a typical boiling curve obtained for an experimental case of Jens & Lottes. We can observe that in this region where wall superheat are low ($\Delta T_w < 5$ K), the quasi-entirety of the wall heat flux is evacuated through liquid convection and transient conduction through quenching. This is likely to be a consequence of the very high pressure conditions under which nucleation site density is very large but bubbles become extremely small ($R \sim \mu\text{m}$). Evaporation heat flux is then relatively small but the large number of bubbles and their sliding induce a strong quenching effect over the heater surface.

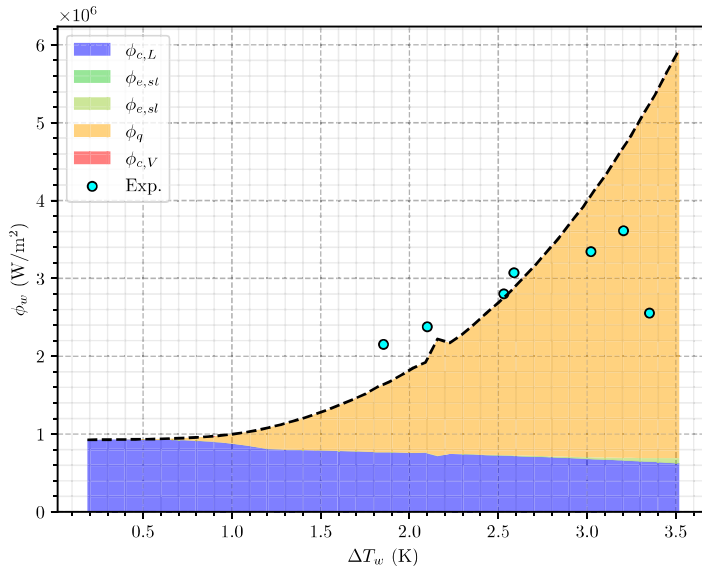


Figure 8.8: Comparison with measured boiling curve by Jens & Lottes [61]. $P = 138$ bar, $G = 2600$ kg/m²/s, $\Delta T_L = 64^\circ\text{C}$.

Figure 8.9 shows the wall temperature predictions achieved with the different HFP models.

Both the new formulation and Kommajosyula model achieve good predictions of the wall temperature in those high pressure conditions. However, Kurul & Podowski and Basu models do not seem to capture properly the wall superheat evolution, with large relative overestimations ($\sim 200\%$).

8.2.3 *Kernel Data*

Kernel measurements are of similar nature to those of Jens & Lottes since they were conducted for a uniformly heated vertical circular metallic pipe. However, the experiments were operated at pressures lower than 6 bar and various inlet liquid mass fluxes and subcoolings. In those conditions, the evaluation of the constant K in the bubble growth profile can be very tricky since the larger bubbles at low pressure are more impacted by the bulk flow, implying potentially large variations of K that can become much lower than 1. Regarding the contact angle, its value can also be roughly estimated using Song & Fan review [118] showing that metallic surfaces at low and moderate pressure also show a contact angle decrease with temperature, with values roughly lying between 40° and 60° when $T_w \sim T_{sat}$. Therefore, we assume:

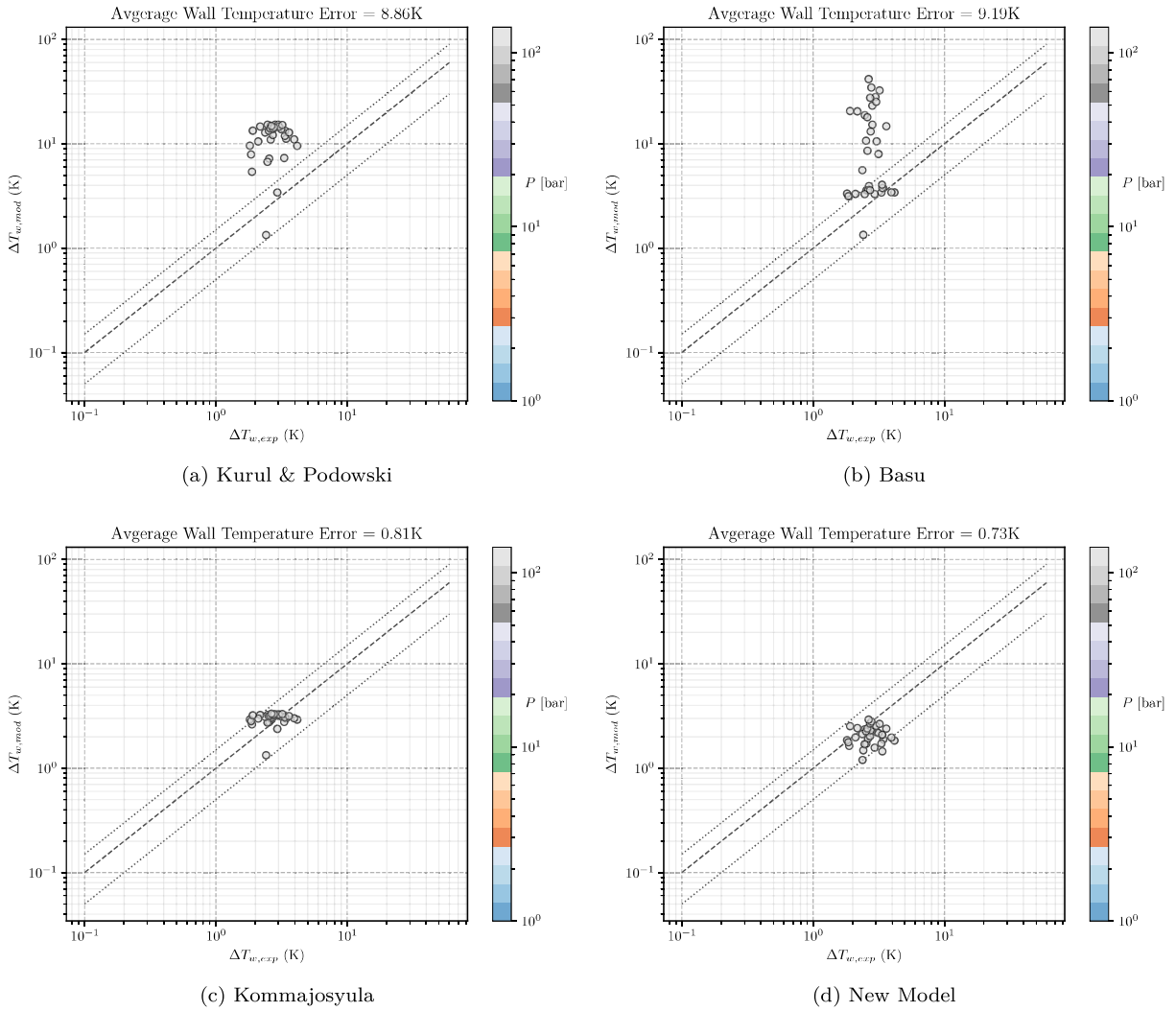


Figure 8.9: Wall temperature predictions achieved by the different HFP models on Jens data.

- $\theta = 50^\circ$;
- $d\theta = 5^\circ$ (larger and deformable bubbles at low pressure) ;
- $K = 0.3$ (larger impact of bulk subcooling on bubble growth).

Figure 8.10 shows the wall temperature predictions achieved with the different HFP models.

Achieving a good quality of wall superheat predictions for the cases of Kennel appears more complicated. Indeed, the new formulation and Kommajosyula model obtain the best results but still present an average underestimation of approximately 50%. The very large range of conditions associated to the low pressure may invalidate the assumption of constants values for $d\theta$ and K .

Remark : In his work, Kommajosyula [71] presented better wall temperature predictions on Kennel data with his model (average error between 3 K and 5 K). We only managed to achieve similar results using a much lower contact angle ($\theta \leq 20^\circ$) which could be questioned regarding the operating conditions.

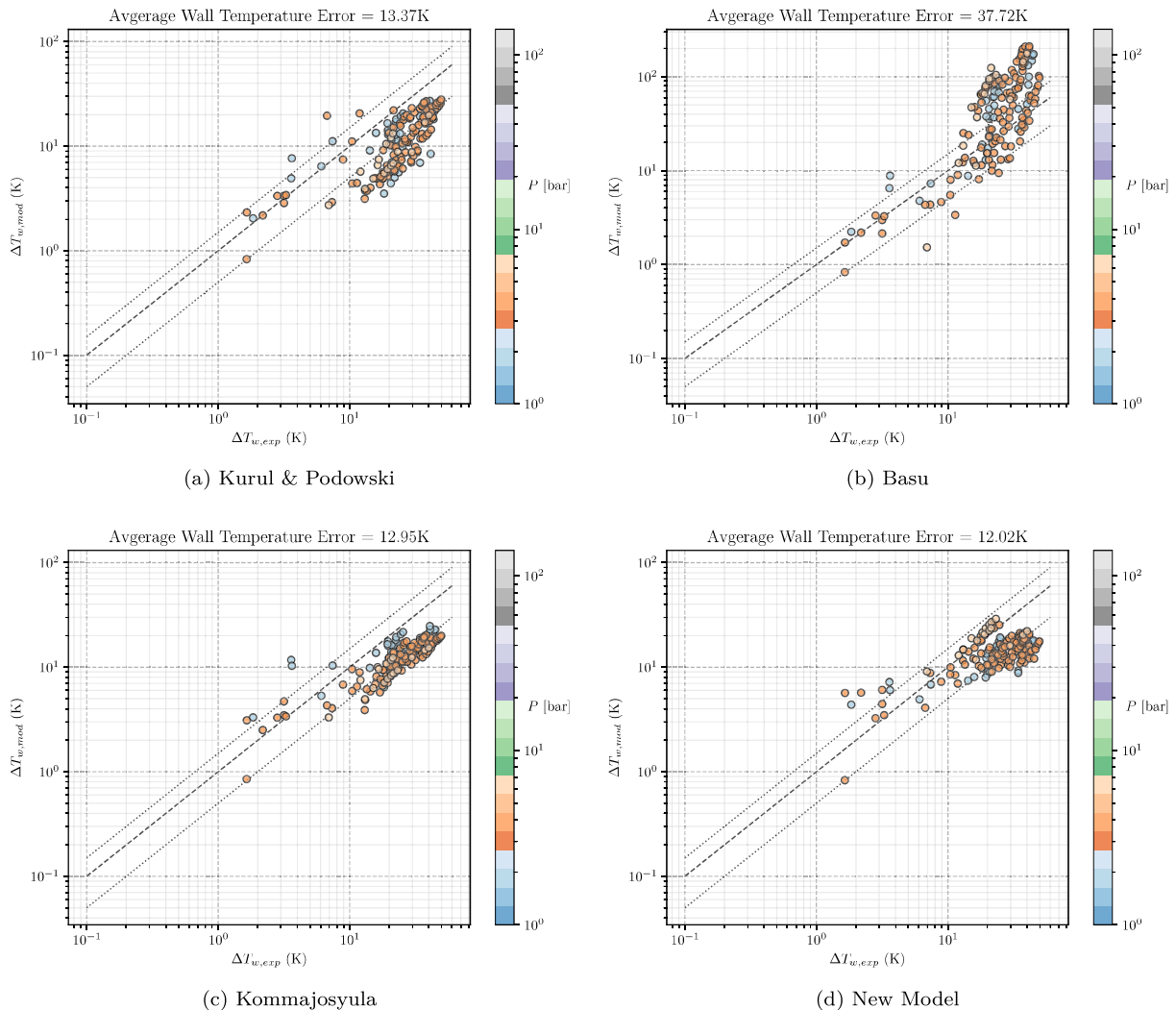


Figure 8.10: Wall temperature predictions achieved by the different HFP models on Kennel data.

8.3 VALIDATION FOR DEBORA EXPERIMENT

In order to try a further validation of the proposed HFP model, we will test it under conditions that are representative of the DEBORA cases for the G2P26W16 campaign (Chapter 3):

- R12 as operating fluid ;
- $P = 26.2$ bar ;
- $G_L = 2000 \text{ kg/m}^2/\text{s}$;
- $\phi_w = 73.9 \text{ kW/m}^2$.

Since refrigerant are usually known to have low contact angle and recalling that wall temperature in this case is less than 20°C lower than R12 critical temperature ($T_{\text{crit},\text{R12}} \approx 380 \text{ K}$), we suppose $\theta = 5^\circ$. The operating pressure being experimentally chosen to match high-pressure water similarity, we thus choose $d\theta = 1^\circ$ and $K = 2$ in accordance with the choices made for Jens & Lottes cases.

Based on the NCFD calculations of case 8G2P26W16Te44.9 (Chapter 4), we extract the axial profile of T_L and U_L in the wall-adjacent cell and use it as inputs in the HFP models. This yields the axial wall temperature profile presented in Figure ??.

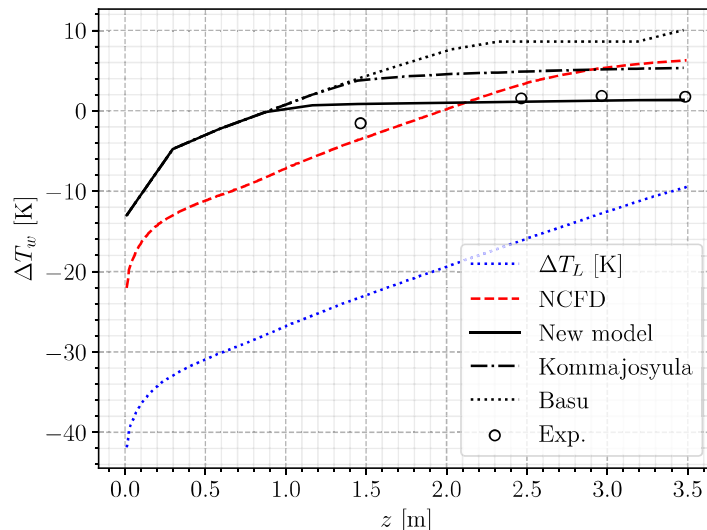


Figure 8.11: Comparison of different HFP on the 8G2P26W16Te49 DEBORA case.

We see that the models perform in very different ways for the DEBORA conditions. Basu *et al.* formulation largely overestimates the experimental value while Kommajosyula's model finds a wall temperature slightly lower than the NCFD computation. On the other hand, the new formulation provides a wall temperature much closer to the experimental measurements, which is probably an effect mainly due to the large quenching combined with the pressure dependency of the nucleation site density.

8.4 CONCLUSIONS

In this Chapter, we proposed different aspects of validation regarding the proposed Heat Flux Partitioning model developed in Section 7.9. All in all, we can conclude that:

- The evolution of most physical parameters included in the model are coherent with detailed measurements conducted by Kossolapov [72] (Section 8.1), namely the nucleation site density, the bubble departure frequency, waiting time and quenching time.
- The quenching seems overestimated with a probably too large sliding length. Meaning that the proposed modeling (*i. e.* average distance between two nucleating bubbles, Section 7.7) is likely to be an upper bound of the actual sliding length. Bubbles may actually slide over shorter length, which would require dedicated investigations when reaching boiling regimes with large bubble density on the wall.

- The formulation seems able to capture different nature of heat flux partition, with high-quenching regimes at high pressure and low superheats (Figure 8.8), regimes with both static and sliding coalescence at high pressure and high superheat (Figure 8.6), or mixed between quenching and sliding coalescence at low to moderate pressure and high superheat (Figure 8.6).
- Wall temperature predictions (Section 8.2) using the new formulation along with reasonable values for the closing parameters (θ , $d\theta$, K) yields better results in average compared to older models. In particular, it seems capable of enhancing the wall temperature predictions on the DEBORA case as shown on Figure ??.